Detection of molecular interactions using field-effect-based capacitive devices

Dissertation

zur Erlangung des akademischen Grades
d o c t o r r e r u m n a t u r a l i u m
(Dr. rer. nat.) im Fach Chemie

eingereicht an der
Mathematisch-Naturwissenschaftlichen Fakultät I
Humboldt-Universität zu Berlin

von

M.Sc. Maryam Hadji Abouzar

Präsident der Humboldt-Universität zu Berlin:
Prof. Dr. Jan-Hendrik Olbertz
Dekan der Mathematisch-Naturwissenschaftlichen Fakultät I:
Prof. Dr. Andreas Herrmann

Gutachter/innen: 1. PD. Dr. Werner Moritz

2. Prof. Dr. Michael Josef Schöning

3. Prof. Dr. Michael Keusgen

Tag der mündlichen Prüfung: 8. August 2011

Abstract

Label-free detection of molecular interactions utilizing field-effect devices is one of the most attractive approaches for a new generation of biochips with direct electrical readout for a fast, simple and cost-effective analysis.

In this study, a capacitive electrolyte-insulator-semiconductor (EIS) structure was used as transducer for the label-free electrical detection of charged macromolecules via their intrinsic charge. Polyelectrolyte multilayers (PEM) and DNA molecules were utilized as model systems to study the charge effects induced in EIS sensors by the formation of “planar”- and “brush”-like molecular layers, respectively.

The layer-by-layer adsorption of positively and negatively charged polyelectrolyte (PE) layers onto the sensor surface as well as the influence of PE concentration, ionic strength and type of the applied electrolyte on the EIS sensor signal was electrochemically studied. In addition, the PEMs build-up was physically characterized using atomic force microscopy, scanning electron microscopy and ellipsometry.

An array of on-chip integrated nanoplate EIS sensors based on a silicon-on-insulator structure was developed for the first time, enabling the reliable detection of DNA hybridization/denaturation in a differential measurement setup. Enhanced DNA biosensor characteristics were achieved by the immobilization of DNA molecules on the sensor surface via Au-nanoparticles and used low-concentrated buffer solution for the measurements. The results of this novel approach were validated by means of the fluorescence microscopy method.

Furthermore, an electrostatic model for an EIS sensor modified with “planar”- and “brush”-like molecular layers was developed. The model predicts a strong dependence of the sensor signal on the electrolyte concentration, surface charge density and the distance between the charged layer and the sensor surface. This is consistently agreeing with the experimental results.

Keywords:

Label-free detection, polyelectrolyte, DNA, field effect.

Zusammenfassung

Die markierungsfreie Detektion von molekularen Wechselwirkungen mittels Feldeffekt-basierter Sensoren ist eine vielversprechende Strategie zur Entwicklung einer neuen Generation von Biochips mit direkter elektrischer Auslesung und somit geeignet für schnelle, einfache und kostengünstige Analysen.

In dieser Arbeit wurde als Transducer eine kapazitive Elektrolyt-Isolator-Silizium- (EIS) Struktur zur markierungsfreien elektrischen Detektion geladener Makromoleküle anhand ihrer intrinsischen Ladung verwendet. Als Modellsystem für die Untersuchung der im EIS-Sensor durch die Ausbildung „planarer“ bzw. „brush“-ähnlicher Molekülschichten induzierten Effekte wurden Polyelektrolyt-Multischichten (PEM) bzw. DNA-Moleküle verwendet.

Die Adsorption der positiv und negativ geladenen Polyelektrolyt-Schichten an die Sensor-Oberfläche, sowie der Einfluss der Polyelektrolyt-Konzentration, der Ionenstärke und der Art des Elektrolyten auf das EIS-Signal wurden elektrochemisch untersucht. Zusätzlich wurde die Ausbildung der PEM physikalisch unter Verwendung eines Rasterkraftmikroskopes und der Ellipsometrie charakterisiert.

Basierend auf Silizium-Isolator-Silizium-Strukturen wurde zum ersten Mal ein Mikroarray mit „Nanoplate“ EIS-Sensoren entwickelt, die alle auf einem einzigen Chip integriert waren. Dies ermöglicht mittels differenzieller Messanordnungen eine verlässliche Detektion der DNA-Hybridisierung bzw. -Denaturierung. Die Eigenschaften des Biosensors wurden durch Verwendung von Gold-Nanopartikeln für die Immobilisierung der DNA auf der Sensoroberfläche sowie durch eine niedrige Salzkonzentration im Messpuffer entscheidend verbessert. Die Ergebnisse dieser neuen Vorgehensweise wurden mittels Fluoreszenz-Mikroskopie validiert.

Darüber hinaus wurde ein elektrostatisches Modell für einen EIS-Sensor mit einer „planaren“ und einen weiteren, mit „brush“-ähnlicher Molekularschicht entwickelt. Das Modell prognostiziert eine starke Abhängigkeit der Sensorsignalstärke von der Elektrolytkonzentration, der Ladungsdichte auf der Oberfläche und dem Abstand zwischen geladener Schicht und Sensoroberfläche. Die Prognosen stimmten durchweg gut mit den experimentellen Ergebnissen überein.

Schlagwörter:

markierungsfrei, Polyelektrolyt, DNS, Feldeffekt.

Contents

List of Figures

List of Tables

List of abbreviations

A	Adenine
AFM	Atomic force microscopy
Au-NP	Gold nanoparticles
ac	Alternating current
C	Cytosine
CA	Contact angle
ConCap	Constant-capacitance
C-V	Capacitance-voltage
DNA	Deoxyribonucleic acid
dsDNA	Double-stranded DNA
ssDNA	Single-stranded DNA
dc	Direct current
EIS	Electrolyte-insulator-semiconductor
EISOI	Electrolyte-insulator-silicon-on-insulator
En-FED	Enzyme-based field-effect device
FED	Field-effect device
G	Guanine
I	Insulator
IS	Impedance spectroscopy
ISFET	Ion-sensitive field-effect transistor
IUPAC	International Union of Pure and Applied Chemistry
M	Metal
MIS	Metal-insulator-semiconductor
MPTES	3-mercaptopropyl trimethoxysilane
NW	Nanowire
PAH	Poly (allylamine hydrochloride)
PB	Poisson-Boltzmann
PBS	Phosphate buffer solution
PDADMAC	Poly (diallyldimethylammonium chloride)
PE	Polyelectrolyte
PEM	Polyelectrolyte multilayer
PSS	Poly (styrene sulfonate)

pzc	Point of zero charge
S	Semiconductor
SEM	Scanning electron microscopy
SNP	Single nucleotide polymorphisms
SOI	Silicon-on-insulator
SSC	Sodium chloride-sodium citrate buffer
TEA	Trimethanolamine
TMAH	Tetramethylammonium hydroxide
TOA	Tetraoctylammonium

List of symbols

A	Surface area
β	Denaturation efficiency
β_{int}	Surface intrinsic buffer capacity
C	Capacitance of the structure
C_a	SiO_2/electrolyte interface capacitance
C_{dif}	Differential double-layer capacitance
C_{dl}	Double-layer capacitance
C_{eff}	Effective gate capacitance
C_{FB}	Flat-band capacitance
C_i	Insulator capacitance
$C_{HF_{\text{min}}}$	High-frequency minimum capacitance
$C_{LF_{\text{min}}}$	Low-frequency minimum capacitance
C_m	Measured capacitance of the structure
C_{min}	Minimum value of capacitance
C_{PE}	Capacitance of the adsorbed PE on the insulator surface
C_{sc}	Space-charge capacitance
c_0	Concentration in electrolyte in mol/L
c_m	Concentration of the mobile ions in PEM
D_{Au-NP}	Diameter of gold nanoparticle
D_{dsDNA}	Diameter of double-stranded DNA
D_{ssDNA}	Diameter of single-stranded DNA
d	Thickness of insulator layer
d_{PE}	Thickness of each PE layer
d_{Si}	Thickness of the top Si
ΔV_{fb}	Shift of the flat-band voltage
E_0	Amplitude of the potential
E_{ref}	Potential of the reference electrode

E_t	Potential at time t
e_0	Elementary charge
ε_0	Air permittivity
ε_i	Insulator permittivity
ε_s	Silicon permittivity
f	Frequency
Φ	Phase shift
ϕ_s	Semiconductor-surface potential
ψ	Potential distribution
ψ_0	Electrolyte solution/charged surface interface potential
ψ_{PE}	Surface potential of a PE layer
ψ_{s-PE}	Potential at the electrolyte/gate interface after the PE adsorption
I	Current
I_m	Ionic strength in PEM
I_t	Current at time t
K_B	Boltzmann constant
K_1 and K_2	Chemical equilibrium constants
k^{-1}	Debye length
k_m^{-1}	Debye length in PEM
L	DNA length
l_B	Bjerrum length
λ_D	Debye length
m	Number of DNA per gold nanoparticle
n_b	Number of base pairs
n_{PE}	Number of adsorbed layers
pK_a	Acidity constant
Q_d	Charge in depletion region
Q_e	Electron charge in the inversion region
Q_h	Charge of the accumulated holes

Q_i	Located charge in insulator
Q_M	Charge on the metal gate
R	Resistance of the structure
R_c	Contact resistance
R_e	Electrolyte resistance
R_{ms}	Roughness (quantified by the root-mean-square value)
R_{RE}	Reference electrode resistance
R_{Si}	Lateral bulk resistance of Si
R_{sc}	Space-charge resistance in the semiconductor
R_{sp}	Specific contact resistance
ρ	Resistivity of the substrate
σ	Charge density
σ_{PE}	Charge density of a PE layer
σ_{ssDNA}	Charge density of ssDNA
σ_{dsDNA}	Charge density of dsDNA
T	Thymine
T	Thermodynamic temperature
T_m	Melting temperature
t	Time
θ	Fraction of charge neutralization
V_G	Gate voltage
V_T	Threshold voltage
V_{fb}	Flat-band voltage
W_M	Metal-electron work function
W_S	Silicon-electron work function
w_d	Width of the depletion region
w_m	Maximum width of the depletion region
ω	Radial frequency
χ_{sol}	Surface-dipole potential
x_m	PEM thickness

y	Dimensionless potential
Z	Impedance of the system
Z_0	Magnitude of impedance
$\|Z\|$	Absolute magnitude of the impedance
Z'	Real component of the impedance
Z''	Imaginary component of the impedance
Z_w	Warbung impedance (diffuse impedance)
ζ	Zeta potential

Chapter 1

1 Introduction

The history of biosensors started about fifty years ago with the development of the glucose sensor. In 1962, Clark and Lyones fabricated a glucose sensor by the immobilization of glucose oxidase molecules on an oxygen-sensing electrode via a dialysis membrane [ClaLy62] to make the oxygen electrode sensitive to the analyte (glucose). The idea of coupling bio-recognition elements with various types of transducers has been used as a basis for the realization of different biosensors, which had extraordinarily grown over recent years. One of the main driving forces behind the significant increase of interest and research in (bio-)chemical sensors has been the enormous progress in biotechnology (e.g., genomics, proteomics and pharmaceuticals) and the necessity of controlling and monitoring complex biochemical processes both *in-vitro* and *in-vivo*. Figure 1.1 schematically demonstrates the functioning principle of (bio-)chemical sensors.

As per definition of IUPAC (International Union of Pure and Applied Chemistry), a biosensor is an analytical device for the detection of an analyte that combines a biological component with a physicochemical detector. It consists of a bio-recognition element (e.g., cell receptors, enzymes, DNA, etc.) the transducer (e.g., optical, piezoelectric, electrochemical, etc.) that transforms the signal resulting from the interaction of the analyte with the biological element into another measurable signal and related electronics or signal processors that are primarily responsible for the display of the results in a user-friendly way.

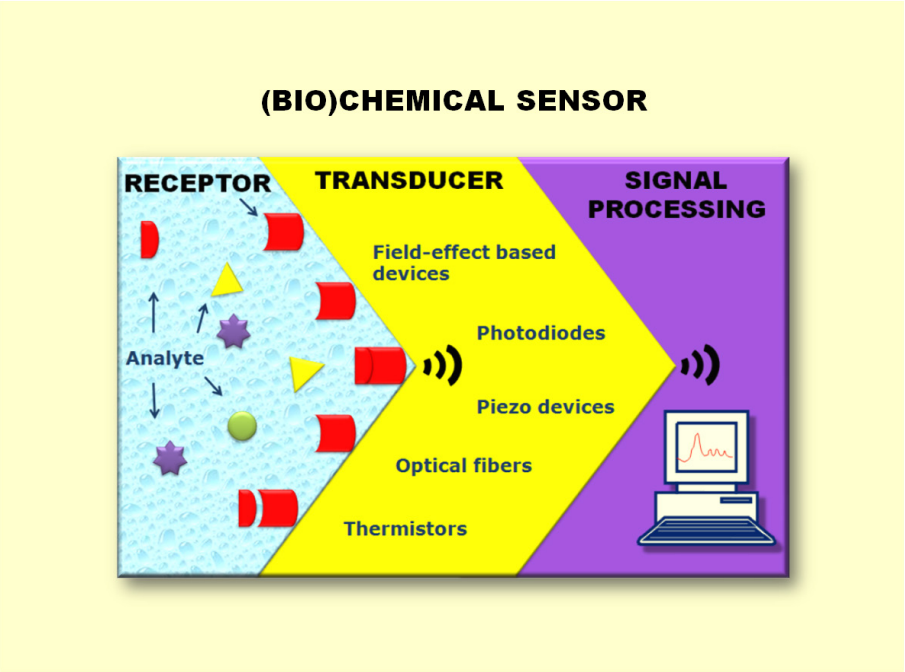

Fig. 1.1: Schematic of functioning principle of (bio-)chemical sensors.

Among different kind of biochips (e.g., protein microarray, antibody microarray, etc.), the DNA biosensor, for application in medical diagnostic (sensing defects, or single nucleotide polymorphisms (SNPs) in genes), biotechnology, pharmacy, food industry and forensic is in great demand. In 1953, the double-helix structure of the DNA molecule was discovered by Watson and Crick [Wat53], which was the first stage for genetic research. Furthermore, the development of sequencing techniques [Maxa77, Sang77] made the decoding of genetic information possible. This approach showed that the hybridization of single-stranded DNA (ssDNA) could be employed for the realization of DNA chips. By DNA-hybridization process, the target ssDNA (unknown ssDNA) is identified by a probe ssDNA and a double-stranded (dsDNA) helix structure with two complementary strands is formed. In general, the commonly used DNA-detection techniques are based on labeling of the target ssDNA molecules with various labels (radiochemical, enzymatic, fluorescent), followed by detection of the labels with specific methods after DNA hybridization [SmSan86, Zou08]. These regularly used techniques are established and sensitive, but due to the labeling step and utilization of complicated instruments for detection of the labels, such methods have been proven to be time-consuming, expensive and complex to implement [PogIn07]. Therefore, a direct label-free detection method of DNA hybridization is preferable.

In the last two decades, following different approaches for label-free detection of DNA hybridization have been described: mass-sensing using quartz crystal microbalance [Dong08],

optical sensing utilizing ellipsometry [DemCa08] and plasmon resonance spectroscopy [ThiFr97], electroanalytical sensing using impedimetric [KafPän08], amperometric [HiaGaj01], voltammetric [KalCan10], chronopotentiometric [WanKaw01] and field-effect-based potentiometric [PogIn07, SakMiy05, VuEsch09] methods. Recently, utilization of field-effect-based devices (FEDs) for development of DNA-based biosensors has been strongly increased. The main driving force behind the enormous research and development in this field is the possibility of direct electrical detection of DNA hybridization using FEDs, which provides a simple, fast and cost-effective DNA analysis [SchgPog06]. Moreover, the possibility of miniaturization of FED-based DNA sensors using advanced microfabrication technology makes them very attractive for analysis of nucleic acid samples [PogCh05]. For preparation of FED-based DNA sensors, the binding of ssDNA molecules (bio-recognition element) into the sensor surface plays a very important role [Zou08, Han06]. The immobilization method should provide a stable binding and define the number of immobilized ssDNA per surface area.

Since most nanomaterials (such as nanoparticles, carbon nanotubes and nanowires) are comparable in size with the bio-recognition elements, like DNA, proteins, among others (see Fig. 1.2), they are favorable interface materials between biological molecules and transducers. For the improvement of FED-based biosensor characteristics, a variety of nanomaterials and nanostructures has been utilized. These include metal nanoparticles [GuRi09, GuAb08, TaGa06], carbon nanotubes [MarTse09, SiqAb09a, SiqAb09b], nanowires (NWs) [HaLi04, VuGh10, ZhLu10, ZhCh08, PaLi07, PaTi07, Stern07], nanogaps [LiCh08, SchgAb07b], nanocrystalline materials [AbPog08a, AbPog08b] and nanoscale films [AbPog10, NefWu07b].

Recently, several research works have been done to detect DNA hybridization by sensing the change of the intrinsic molecular charge during the hybridization process utilizing FEDs (e.g., EIS (electrolyte-insulator-semiconductor) sensors and FETs (field-effect transistors)) [FrCo02, UsIn04, SakMiy05, VuEsch09, InHan07]. Since DNA molecules are poly-anions with negative charges at their phosphate backbone, it could be expected that the hybridization of ssDNA with its complementary strands would directly modulate the capacitance of an EIS structure or the drain current of a FET device. The past decade witnessed an amazing growth in research and development of FED-based DNA sensors, which has been visualized in Fig. 1.3 as a statistical diagram of the publications about this subject.

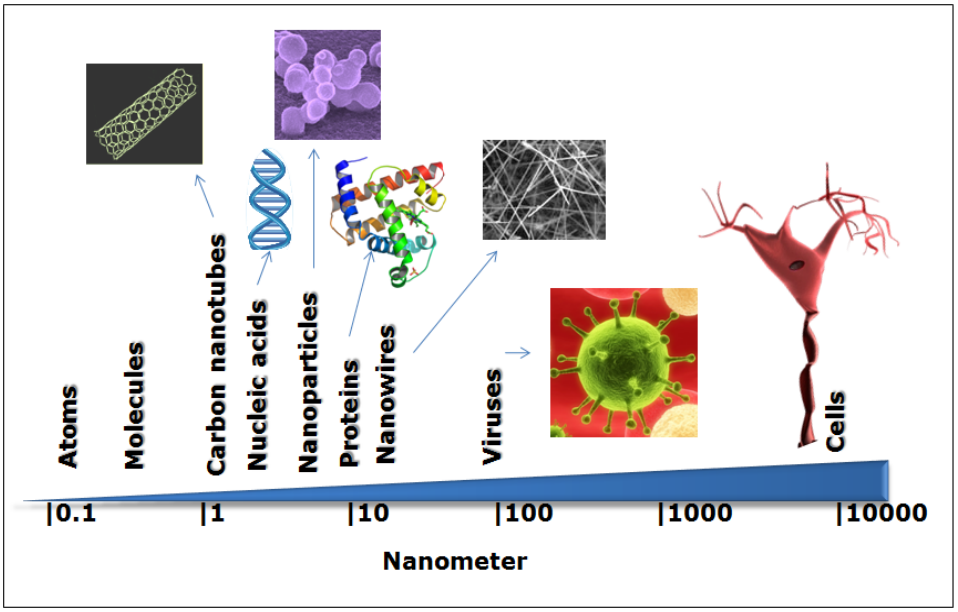

Fig. 1.2: Relative size of various biomolecules and nanomaterials involved in biosensors. Sources of the photos used in this figure: Carbon nanotube [Web1], nanowire [Web2], protein [Web3], nucleic acid, cell and virus [ClipArt of Microsoft Office PowerPoint 2007].

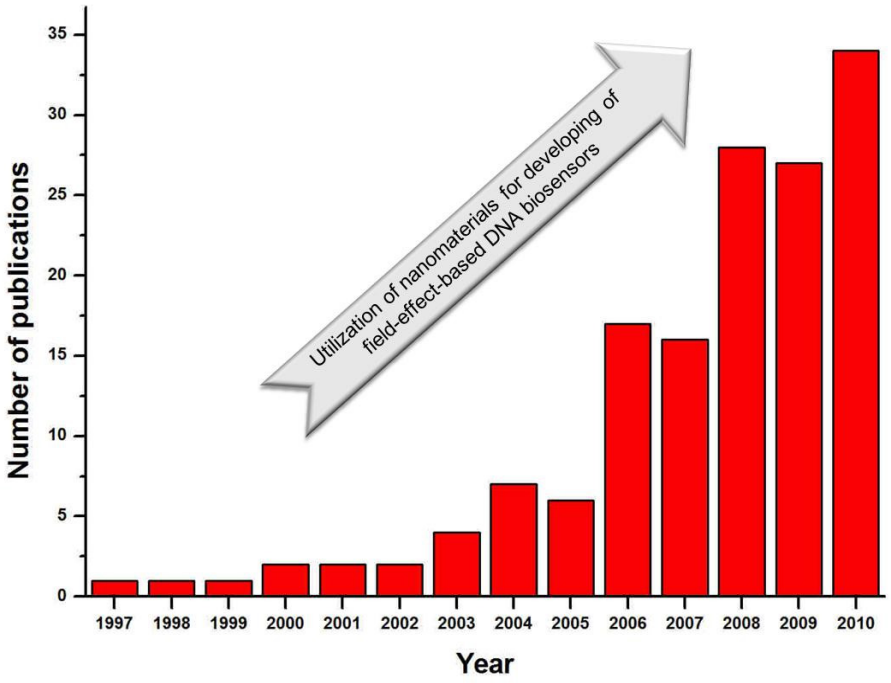

Fig. 1.3: Statistics of publications about label-free detection of DNA using FEDs (source: Web of Science).

In 1997, Souteyrand et al. reported a first attempt of the direct detection of a DNA-hybridization event using a SiO_2-gate ISFET (ion-selective field-effect transistor) and concluded that the detected-signal changes can be induced by a change of the sensor-surface

charge via the DNA-hybridization process [Sout97]. Later on, researchers discussed and critically evaluated the limitation of those FEDs for detection of the charge of DNA molecules [PogCh05, Heiz07, Curr08]. Since only the charge-density changes, which occur at the surface or within the order of the Debye length from the surface, can be detected by FEDs, the detection of the DNA's intrinsic charge is strongly limited by the ion concentration of electrolyte. In addition, it has been demonstrated that the counter-ion condensation effect will mask or reduce the expected hybridization signal, especially in high ionic-strength solutions [PogCh05, Mann01].

Recently, an alternative new method and device for the label-free DNA FED-based detection is suggested, which utilizes an ion-sensitive field-effect device as a transducer [PogCh05]: here, ssDNA probe molecules are arranged into the ion-sensitive layer with a certain intermolecular space, and the redistribution of the ion concentration in the intermolecular spaces and/or alteration of the ion sensitivity of the ion-sensitive layer (due to the DNA hybridization) serves a detection mechanism. Thus, in contrast to field-effect-based DNA-detection devices discussed above, the counter-ion screening effect is used in this case to exactly obtain a useful sensor response. The proposed device is capable of functioning in both low and high ionic-strength solutions without requiring the formation of a tightly packed ssDNA monolayer. The expected DNA-hybridization signal could be in the range of 25-35 mV [PogCh05].

Basically, a deep understanding of the adsorption and interaction of DNA and other charged macromolecules (proteins, polyelectrolytes) into charged surfaces is of great interest not only for sensor applications, but also for the fundamental understanding of many key physiological processes. Generally, the binding and interaction of charged macromolecules can result in the formation of two different kinds of films on the sensor surface, namely, "planar"- and "brush"- like (see Fig. 1.4). In this context, as a model system for label-free field-effect-based detection of the formation of "planar"- and "brush"-like molecular layers, polyelectrolyte layers and DNA molecules can be used, respectively. Polyelectrolytes are linear macromolecule chains bearing a large number of charged or chargeable groups when dissolved in a suitable polar solvent. The subsequent deposition of positively and negatively PE layers leads to a charge inversion of the surface (charge over-compensation effect) [DechEc98], finally resulting in the formation of a PE multilayer (PEM), which is stabilized by strong electrostatic forces.

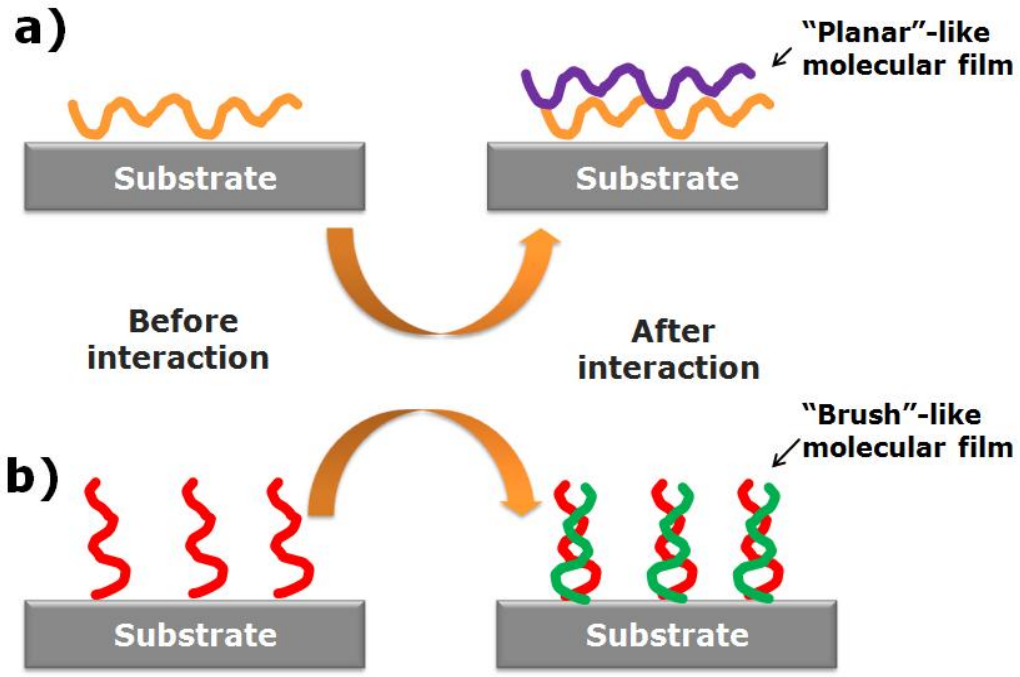

Fig. 1.4: Planar- (a) and brush-like structure of macromolecules before and after interaction with receptors.

Therefore, FEDs modified with PEMs are very useful as a model system for fundamental investigations of the adsorption and binding of charged macromolecules at the solid/liquid interface. Moreover, layer-by-layer (LbL) deposition of PEMs from solutions provides a simple, low-cost and efficient method for the preparation of ultrathin films of a desired architecture, functionality and with a nanoscale control of the thickness [Dech92]. Potential applications of those PEMs range from functional and stimuli-responsive materials, coated colloids, hollow capsules and containers, coatings for lenses and biomedical implants, drug release systems up to biosensors, actuators and organic electronic devices [Kras00, Veer07, Hill06, MaWin09]. For the practical realization of these devices, it is important to understand the formation process and internal structure of PEMs as well as the influence of fabrication parameters on the film characteristics. Adsorption of charged macromolecules on solid substrates and formation of PEMs are determined by a number of factors, like the nature and charge of the surface, the charge density and concentration of the polyelectrolyte, the salt concentration and non-electrostatic interactions of the macromolecules with the surface and with each other [ShRu00]. Recently, beside classical characterization methods (e.g., zeta-potential measurements [EtPi04], X-ray photoelectron spectroscopy [CarNi97], contact-angle measurement [HäFi07], and atomic force microscopy [MeJac03]), FEDs have been also used for the study of internal electrostatic and interfacial properties of PEMs [NefNa06]. Neff et. al. developed a

theoretical model (capacitor model), which quantitatively described the response of field-effect-based thin-film resistors via the formation of PEMs [Nef06]. Theoretical models described in the literature so far, however, do not completely provide a clear understanding of the mechanism of molecular detection by means of FEDs. The quantitative understanding of the counter-ion screening effect and charge distribution within the molecular layer as well as the influence of the distance of charged macromolecules from the sensor surface on the sensor signal still needs some more clear interpretation [SchgAb07a].

In this context, the experimental as well as the theoretical study of detection of molecular interactions using EIS structures for (bio-)chemical sensing is the subject of this research work. To deal with the theme, the present approach is to achieve the following goals:

- More detailed investigation of PEMs build-up using EIS sensors and physical characterization methods (e.g., atomic force microscopy (AFM), scanning electron microscopy (SEM) and ellipsometry). Moreover, the investigation includes studying the influence of the number of PE layers, PE concentration, ionic strength and the type of the applied electrolyte on the EIS-sensor response and PEM's morphology.
- Design and fabrication of on-chip-integrated nanoplate EIS sensors based on a silicon-on-insulator structure to enable a reliable and reproducible detection of DNA hybridization/denaturation in a differential measurement setup. Due to the fabrication procedure, the preparation of the on-chip nanoplate capacitive EISOI sensor arrays is simple and cost-effective (only two photolithography steps are needed) in comparison to SOI-based ISFETs or nanowire transistors [AbPog11a].
- Realization of an EISOI-based DNA-sensor array with enhanced biosensor characteristics using Au-NPs for immobilization of target ssDNA molecules on the sensor surface. Also, applying a low-concentrated buffer solution for the DNA measurements, thereby reducing the screening of the intrinsic charge of the DNA molecules by counter ions in the solution.
- Development of an electrostatic model for an EIS structure modified with PEMs and ssDNA/dsDNA molecules. The model shall explain the influence of the electrolyte concentration, surface charge density and the distance between charged layer and sensor surface on the sensor-output signal.

The format of this thesis is as follow:

- **Chapter 1** presents the aim and motivation of this study.
- **Chapter 2** describes the functioning principle of FEDs and the electric potential of surfaces in liquids.
- **Chapter 3** depicts the properties of PEs used in this work and the influence of intrinsic and extrinsic factors on the polyelectrolyte multilayer build-up. Furthermore, the chapter presents the structure of the DNA molecule as well as the hybridization/denaturation conditions.
- **Chapter 4** focuses on the fabrication and general characterization of the sensors (EIS and EISOI sensor array) used in this work. The fabricated sensors have been physically characterized using SEM and ellipsometry. To study the electrical and electrochemical behavior of the realized sensors, their frequency-dependent capacitance-voltage (*C*-*V*) curve and their impedance spectra have been measured. Furthermore, an electrical equivalent circuit has been developed for EISOI sensors, which explains the impedance and *C*-*V* behavior of the sensors. The pH sensitivity of bare sensors was examined using ConCap (constant-capacitance) method, which is required for the further characterization of functionalized sensors with PEMs and DNA molecules in the next chapters.
- **Chapter 5** deals with the label-free electrical detection of the PEM build-up (as a model system for "planar"-like molecular films) on the SiO_2 surface using EIS sensors. After adsorption of each PE layer, ellipsometry and AFM were applied for characterizing the changes in the PEMs thickness and surface morphology, respectively. The influence of the terminating polyelectrolyte layer on the wetability of the sensor surface during the multilayer formation was studied by means of water contact-angle measurements. Moreover, variation in the surface potential via adsorption of polyelectrolytes on the SiO_2 surface using EIS sensors was electrochemically monitored and the influence of the ion concentration of electrolyte, concentration of PE as well as the type (buffered and unbuffered) of used electrolytes on the EIS sensor signals have been studied. To analyze the sensor response, an electrostatic model for an EIS sensor modified with PEMs was developed, which takes into account the Debye screening of the intrinsic charge of the PEs by mobile ions in the electrolyte as well as within the PEMs. In addition, the application of weak PEs for preparing biosensors with enhanced characteristics is introduced and demonstrated.
- **Chapter 6** focuses on the functionalization of the EISOI sensors with Au-NPs and the immobilization of DNA molecules on the sensor surface. The fabricated EIS sensors

and nanoplate EISOI sensor array were applied for the label-free detection of DNA hybridization and denaturation in a differential-mode arrangement. To reduce the screening of the DNA charge by mobile ions in the electrolyte, the measurements were performed in low-concentrated buffer solution. The results of electrochemical characterization of DNA detection were proven by fluorescence microscopy method. To predict the effective potential change at the sensor surface via DNA hybridization, an electrostatic model using the linear Poisson-Boltzmann approach was developed and the mechanism of signal generation is discussed.

- **Chapter 7** presents the conclusions and discusses possible further applications of the results and concepts developed in this work.

The Appendixes contain recipes and protocols used in this work including the technical sketches of the developed measurement cell and photomasks used for the EISOI sensor-array fabrication.

Chapter 2

2 Field-effect-based sensors

The functioning principle of field-effect-based capacitors, namely the MIS structure and the EIS sensor are explained in this chapter. Furthermore, the change in the surface potential at the solid/liquid interface caused by the change of the pH value of the electrolyte is demonstrated. The fundamental principles presented are used as a basis for understanding of the function of modified sensors with macromolecules used in this work.

2.1 Metal-insulator-semiconductor structure

The operation principle of field-effect-based capacitive EIS sensors can be described by comparing them with their electronic analogue, the MIS structure [PogSchg06, Sze81]. Figure. 2.1 demonstrates an MIS structure that consists of a semiconductor substrate (in this case, p-type silicon) and a metal layer. The semiconductor and the metal gate are separated by a thin insulating material (e.g., silicon dioxide). The insulator is assumed to be ideal in the sense that no current passes through the insulator (no leakage current) [PogSchg06].

The MIS structure can be compared to parallel-plate capacitors. However, the difference and useful property of the MIS structure is that the applied voltage on the gate modulates the space-charge distribution in the semiconductor and thus, the capacitance of a MIS structure [PogSchg06].

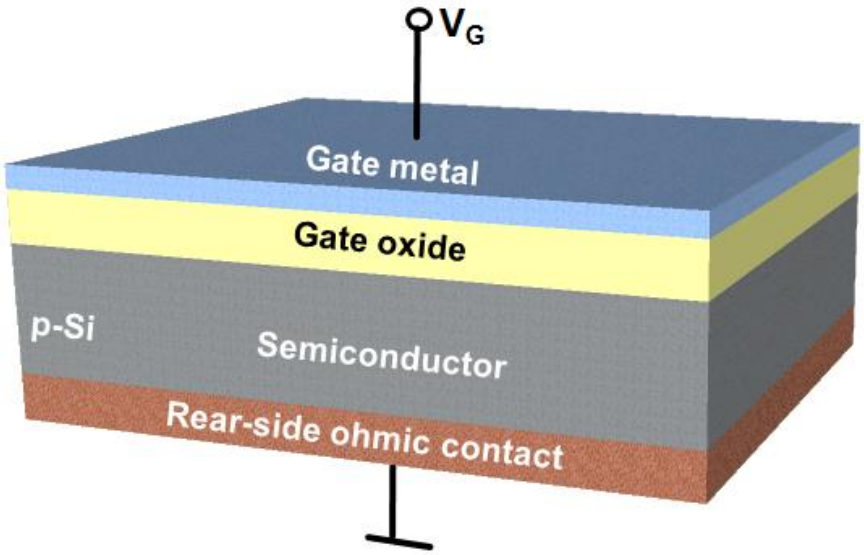

Fig. 2.1: Schematic of an MIS structure. V_G: gate voltage.

The total capacitance of the MIS structure (C) can be modeled as a series of combination of the insulator capacitance ($C_i = \varepsilon_0 \varepsilon_i A/d$, where ε_0, ε_i, A and d are air permittivity, insulator permittivity, surface area and thickness of insulator layer, respectively) and the voltage-dependent space-charge capacitance of the semiconductor (C_{sc}) [Sze81, Nico82, PogSchg06]:

$$C = \frac{C_i C_{sc}}{C_i + C_{sc}} \tag{2.1}$$

In equation (2.1), for a given insulator thickness d, C_i is constant and corresponds to the maximum capacitance of the system. The value of C_{sc} is determined by the thickness of the space-charge region in the silicon layer, which is a function of the applied voltage to the system. As a result, the total capacitance of the MIS structure will also depend on the applied voltage.

A theoretical C-V curve for an ideal p-type MIS structure is given in Figure. 2.2. Depending on the magnitude and polarity of the applied gate voltage (V_G), the C-V curve shows three distinct regions: accumulation, depletion, and inversion [PogSchg06].

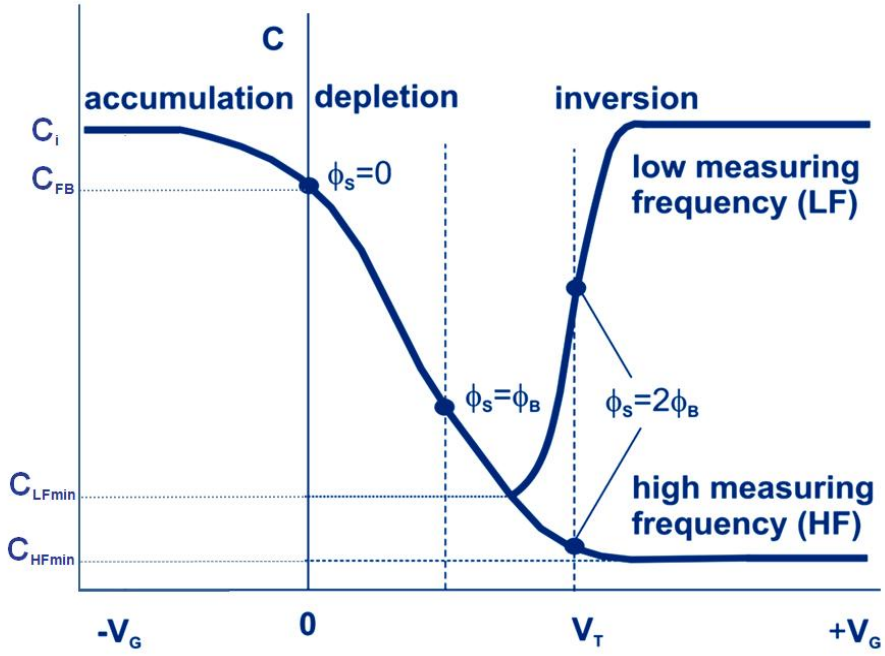

Fig. 2.2: Theoretical *C-V* curve of an ideal p-type MIS structure at high and low measuring frequencies. ϕ_s: semiconductor-surface potential, ϕ_B: potential difference between the Fermi level in the bulk semiconductor (E_F) and the intrinsic Fermi level E_i (midband energy), C_i: insulator capacitance, C_{FB}: flat-band capacitance, C_{LFmin}: low-frequency minimum capacitance, C_{HFmin}: high-frequency minimum capacitance, V_T: threshold voltage (adopted from [PogSchg06]).

A schematic representation of the charge distribution and energy-band diagram for these three modes is given in the Figure. 2.3. The accumulation operating mode occurs, when a negative potential is applied to the metal gate (Fig. 2.3.a). Here, the created electric field attracts positively charged holes from the silicon to accumulate at the silicon-insulator interface and the MIS capacitor behaves like a conventional parallel plate capacitor. Thus, the total capacitance of the structure is defined by the capacitance of the insulator layer, $C=C_i$ (Fig. 2.2) [PogSchg06].

By applying a small positive potential ($V_G>0$) to the metal, the electric field will push the positive mobile charge carriers (i.e., the holes) away from the semiconductor-insulator interface (depletion mode). As a result, a depleted region of mobile carriers is formed at the semiconductor-insulator interface (see Fig. 2.3.b). The width of the depletion region (w_d) depends on the applied voltage, the doping concentration, the dielectric constant and the insulator thickness [PogSchg06]. The total capacitance of the MIS structure in the depletion mode is represented as the series of a fixed capacitance of the insulator layer and a variable capacitance of the depletion layer and given by [Sze81, Grat98, PogSchg06]:

$$C = \frac{C_i}{(1 + (\varepsilon_i w_d / \varepsilon_s d))} \tag{2.2}$$

where ε_s is the permittivity of the semiconductor. Increasing of the applied voltage results in increasing of w_d, and decreasing of the total capacitance.

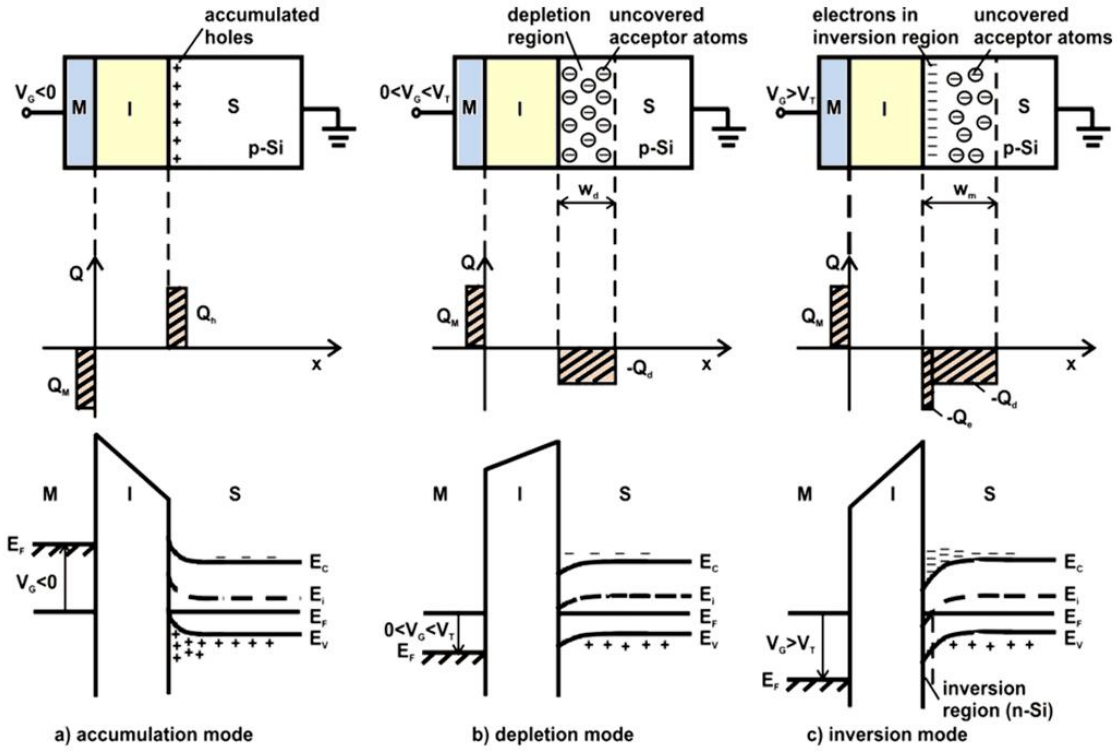

Fig. 2.3: Charge distribution and energy-band diagram of the MIS structure in accumulation (a), depletion (b) and inversion (c) mode, respectively. M: metal, I: insulator, S: semiconductor, Q_M: charge on the metal gate, Q_h: charge of the accumulated holes, Q_d: charge in depletion region (charge of the uncovered acceptors), w_d: width of depletion region, w_m: maximum width of the depletion region, Q_e: electron charge in the inversion region. The (+) symbols near the valence band at the semiconductor-insulator interface represent the accumulated holes. The (-) symbols near the conduction band represent the electrons in the inversion layer (from [PogSchg06]).

Moreover, by increasing the magnitude of the applied positive potential to the metal (V_G>>0), the energy bands bend down further at the interface, which is referred to inversion condition (Fig. 2.3.c). When the Fermi level bends below the intrinsic level, the electron concentration near the interface exceeds the hole concentration. Thus, a thin layer of n-type silicon (an inversion layer) is formed, although the substrate is p-type. In the inversion region at low frequency, the measured total capacitance can again become equal to the insulator capacitance [PogSchg06, Sze81]. In the low-frequency case, the gate-charge fluctuations are slow enough

that the inversion charge can follow the variation directly. At higher frequencies, the supply of charge carriers to the inversion layer is not sufficiently rapid to attain equilibrium. As a consequence, *C-V* curves measured at higher frequencies do not show the increase of the capacitance in the inversion region [PogSchg06, Sze81].

The transition between accumulation and depletion condition is called “flat-band” condition and occurs when the energy bands in the silicon continue horizontally up to the surface. This condition is met when there is no electric field in the silicon, and the net-charge density in the silicon is zero (for an ideal MIS structure when $V_G = 0$ (see Fig. 2.2)). However, for a real (non-ideal) MIS structure the flat-band voltage (V_{fb}) is shifted by an account related to the difference between the metal (W_M) and the silicon (W_S) electron work function and the presence of charges located in the oxide (Q_i, mobile, fixed, trapped, etc.) and surface and interface states (Q_{ss}, due to non-ideal processing and material conditions) [Blac87, BergSib88, PogSchg06]:

$$V_{fb} = \frac{W_M - W_S}{q} - \frac{Q_i + Q_{ss}}{C_i} \tag{2.3}$$

Non-ideality leads to a band bending even at equilibrium in the semiconductor. Here, to reach the flat-band condition, an additional potential must be applied to the metal [PogSchg06].

2.2 Electrolyte-insulator-semiconductor structure

The simplest field-effect-based (bio-)chemical sensor is the EIS sensor, which represents a (bio-)chemically sensitive capacitor. The structure of the capacitive EIS sensor is shown in Figure 2.4. It is obtained from an MIS structure by replacing the metal gate by an electrolyte and a reference electrode. For operation, a dc (direct current) polarization voltage is applied via the reference electrode to set the working point of the EIS sensor, and a small ac (alternative current) voltage is applied to the system in order to measure the capacitance of the sensor, similar to the well-known measurements with MIS capacitors [PogSchg06, Berg03].

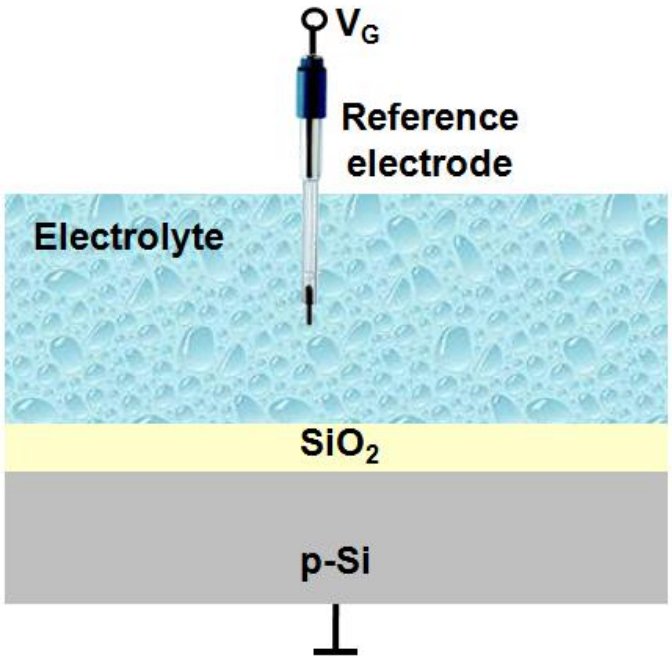

Fig. 2.4: Structure and measuring setup of the capacitive EIS sensor.

The complete ac equivalent circuit of an EIS system is complex and includes components that are related to the semiconductor, gate insulator, different interfaces, electrolyte and reference electrode [Bous83, Mac87]. However, for usual values of insulator thickness (~30-100 nm), the ionic strength of a sufficiently adjusted electrolyte solution (>10^{-4}-10^{-5} M) and the frequencies used, the equivalent circuit of an EIS structure can be simplified as a series connection of the insulator capacitance and space-charge capacitance of the semiconductor [Berg91, FaLa90, Dem95, PogSchg06].

Thus, the expression for the capacitance of the EIS structure ($C(\psi_0)$) is similar to the equation for an MIS capacitance, but with a modulation possibility of V_{fb} and consequently, the space-charge capacitance ($C_{sc}(\psi_0)$), by means of the electrolyte solution/insulator interface potential (ψ_0), which could be caused by a change of the ion concentration in electrolyte or binding with a charged macromolecular layer [Berg91, PogSchg06]:

$$C(\psi_0) = \frac{C_i C_{sc}(\psi_0)}{C_i + C_{sc}(\psi_0)} \tag{2.4}$$

Correspondingly, V_{fb} can be deduced from that of the MIS structure (Eq. (2.3)) by simply adding the potential drops at the additional interfaces [Grat98, Berg91, Berg03, Mado89, Sibb86, Lund91, Jana85]:

$$V_{fb} = (E_{ref} + \chi_{sol} - \frac{W_S}{q} - \frac{Q_i + Q_{ss}}{C_i}) - \psi_0 \tag{2.5}$$

Here, E_{ref} is the potential of the reference electrode, χ_{sol} is the surface-dipole potential of the solution.

In following section (Chapter 2.3), the potential at the electrolyte-oxide interface will be discussed in more detail.

2.3 Oxide/electrolyte interface

2.3.1 Electrical double-layer

If a solid surface and a liquid are brought into contact, the charges of the solid surface cause an electric field at the solid/liquid interface. This electric field attracts counter ions from the electrolyte. The layer which contains surface charges and counter ions is called electric double layer. In general, three models for the electric double layer are existing (Fig 2.5) [Butt03]. The simplest model of an electric double layer (Helmholtz model) defines that the counter ions bind directly to the charged surface and neutralize it (Fig 2.5a). In this model, the electric field generated by surface charges is limited to the thickness of a molecular layer. Nevertheless, the Helmholtz model does not account for many factors such as, diffusion/mixing in the solution, the possibility of absorption on the surface and the interaction between solvent dipole moments and the electrode [Butt03].

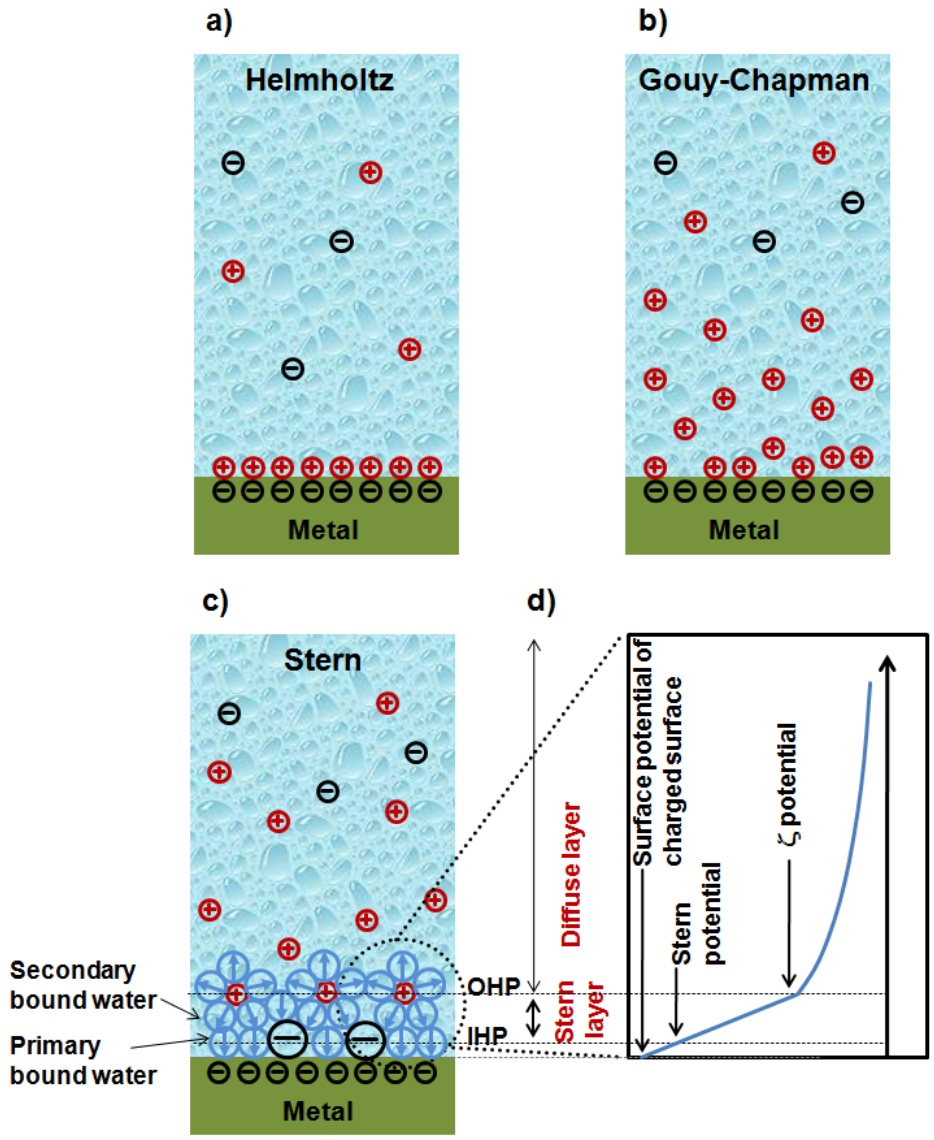

Fig. 2.5: Helmholtz (a), Gouy-Chapman (b) and Stern model (c) of the electric double layer. Potential distribution as a function of distance from the substrate surface (d) (the figures 2.5. a-c are adopted from [Butt03]).

The second introduced model is the Gouy-Chapman double-layer model, which improves the Helmholtz model and takes into account the thermal motion of ions [Butt03]. In this model, thermal fluctuations tend to drive the counter ions away from the surface that results in the formation of a diffuse layer (Fig 2.5.b). With the "linearized Poisson-Boltzmann equation" for planar surfaces, the potential distribution (ψ) for low surface potentials ($\psi_0 \leq 80$ mV), can be calculated [Butt03] as:

$$\psi = \psi_0 . e^{-\kappa x} \tag{2.6}$$

where x is the distance and $k = \lambda_D^{-1}$. Here, λ_D is the decay length (Debye length). The Debye length in a monovalent salt solution with a concentration of c_0 in mol/L at 25°C is defined as follows:

$$\lambda_D = \frac{3\text{Å}}{\sqrt{c_0}} \tag{2.7}$$

In some practical cases, the surface potential is larger than 80 mV. On account of this calculation of potential distributions, the general one-dimensional Poisson-Boltzmann equation should be used [Isr92]:

$$y = 2.\ln\frac{e^{y_0/2} + 1 + (e^{y_0/2} - 1).e^{-kx}}{e^{y_0/2} + 1 - (e^{y_0/2} - 1).e^{-kx}} \tag{2.8}$$

In the above equation, y is the dimensionless potential ($y = e\psi / K_B T$, e_0 is the elementary charge, K_B is the Boltzmann constant and T is the thermodynamic temperature) [Butt03].

Here, using Grahame's equation based on the Gouy-Chapman theory and defined charge density (σ), the potential at the charged surface (ψ_0) can be calculated. The Grahame's equation can be deduced from a condition of "electroneutrality". For this condition, the total charge (i.e., the surface charge plus the charge of the ions) in the whole double layer must be zero. Using the one-dimensional Poisson equation and the fact that the potential and its gradient are zero at great distances, the Grahame equation is derived as follows [Grah47, Butt03]:

$$\sigma = \sqrt{8c_0\varepsilon\varepsilon_0 K_B T}.\sinh(\frac{e\psi_0}{2K_B T}) \tag{2.9}$$

For low potentials ($\sinh x = x$), the relationship is simplified as [Butt03]:

$$\sigma = \frac{\varepsilon\varepsilon_0\psi_0}{\lambda_D} \tag{2.10}$$

and

$$\psi_0 = \frac{\sigma\lambda_D}{\varepsilon\varepsilon_0} \tag{2.11}$$

Neither the Helmholtz nor the Gouy-Chapman model can completely describe the real structure of the electrical double layer. Figure 2.5c shows the Stern model which combined both models and divided the electrical double layer into two parts: Stern layer and diffuse layer. The Stern layer is a layer of ions that is directly adsorbed to the surface. The diffuse layer (Gouy-Chapman layer) consists of mobile ions with a distribution confirmed by Poisson-Boltzmann statistics. The potential at the point where the bound Stern layer ends (outer Helmholtz layer) and the mobile diffuse layer begins is the zeta potential (ζ) (see Fig 2.5.d) [Butt03].

2.3.2 Site-binding model

Commonly used gate-insulator materials for fabrication of EIS structures are oxides (e.g., SiO_2, Ta_2O_5, Al_2O_3) which always contain neutral amphoteric hydroxyl groups (MOH). The mechanism of surface charging for oxides is as follows:

If these are brought in contact with liquids, depending on the pH value of the solution, the neutral surface hydroxyl sites of oxides are either able to bind (MOH_2^+) or release (MO^-) a proton (hydrogen ion) according to the following reactions [Yate74, PogSchg06]:

$$MOH \overset{K_1}{\leftrightarrow} MO^- + H_B^+ \tag{2.12}$$

$$MOH_2^+ \overset{K_2}{\leftrightarrow} MOH + H_B^+ \tag{2.13}$$

where H_B^+ represents the protons in the bulk of the solution, and K_1 and K_2 are chemical equilibrium constants.

Consequently, at pH>pH_{pzc} (where pH_{pzc} is the pH value at the point of zero charge), the oxide surface is negatively charged and at pH<pH_{pzc} the surface is positively charged (Fig. 2.6). A change in the pH will change the oxide-surface potential. The resulting pH-dependent electrical surface charge of the gate insulator will lead to a modulation of the capacitance of the EIS structure [Yate74, PogSchg06].

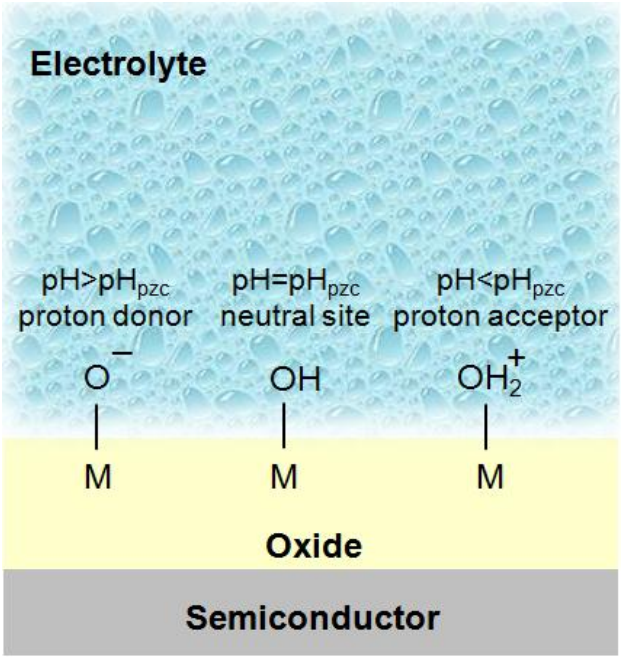

Fig. 2.6: Electrolyte-oxide interface. Depending on the electrolyte pH, the surface groups can be neutral (MOH) or negative (MO^-) or positive (MOH_2^+); pH_{pzc}: pH value at the point of zero charge.

Generally, the pH sensitivity of the EIS system is expressed as follows [Hal96, PogSchg06]:

$$\frac{\delta\psi}{\delta pH_B} = -2.3\frac{K_B T}{q}\alpha \tag{2.14}$$

with

$$\alpha = \frac{1}{(2.3K_B TC_{dif}/q^2\beta_{\text{int}})+1} \tag{2.15}$$

where α is a dimensionless sensitivity parameter ($0< \alpha <1$). The value of α depends on following parameters:

the surface intrinsic buffer capacity (β_{int}), which characterizes the ability of the oxide surface to deliver or take up protons,

the double-layer capacitance (C_{dif}), which is mainly determined by the ion concentration of the bulk solution via the corresponding Debye length.

From equations (2.14) and (2.15), it can be concluded that the maximum Nernstian sensitivity (59.3 mV/pH at 25°C) can be obtained only when α approaches 1 [PogSchg06]. A condition of α=1 is reached for oxides with a high density of surface-active sites and a low value of the double-layer capacity (low electrolyte concentration). A sub-Nernstian response can be expected for oxides with α<1 [PogSchg06]. Therefore, oxides with a large amount of surface sites, like Ta_2O_5 (~10^{15} cm^{-2}) exhibit a high pH sensitivity [SchgBr05], whereas for SiO_2 with less surface sites of $5x10^{14}$ cm^{-2}, a lower pH sensitivity has been observed [Hal96, Hal95, PogSchg06].

Chapter 3

3 Charged macromolecules

In this chapter, the structure and general properties of charged macromolecules, which have been used for the experiments, are presented. Furthermore, the layer-by-layer formation of PEMs as well as the DNA-hybridization/denaturation event is described.

3.1 Polyelectrolytes

Polyelectrolytes are soluble polymers in aqueous solution containing many positively or negatively charged groups [Dech92, Rade01]. The charge of PE is generated by the dissociation of monomer side groups, like amines ($\sim NH_3Cl \rightarrow \sim NH_3^+ + Cl^-$) or sulfonates ($\sim SO_3Na \rightarrow \sim SO_3^- + Na^+$) [Butt03]. Increasing the degree of dissociation leads to rising of the polymer charge.

The conformation and adsorption of polyelectrolytes are strongly influenced by the ionic strength of the solution. In pure water, highly charged polyelectrolytes adopt an extended conformation because of repulsive interactions between charged segments (Fig 3.1a). In salt solution, the interactions are screened so the polyelectrolyte adopts a coiled structure (Fig. 3.1b).

The charge of a polyelectrolyte is shielded in aqueous solution by small ions. This effect is described in the Debye-Hückel model by the screening length. Thus, the electrolyte affects both the polymer adsorptivity and adsorbed layer thickness via the screening of electrostatic polymer-surface attraction and of electrostatic repulsion between the charged segments [BarJo96, ChoSt99, Dob96; Mic99].

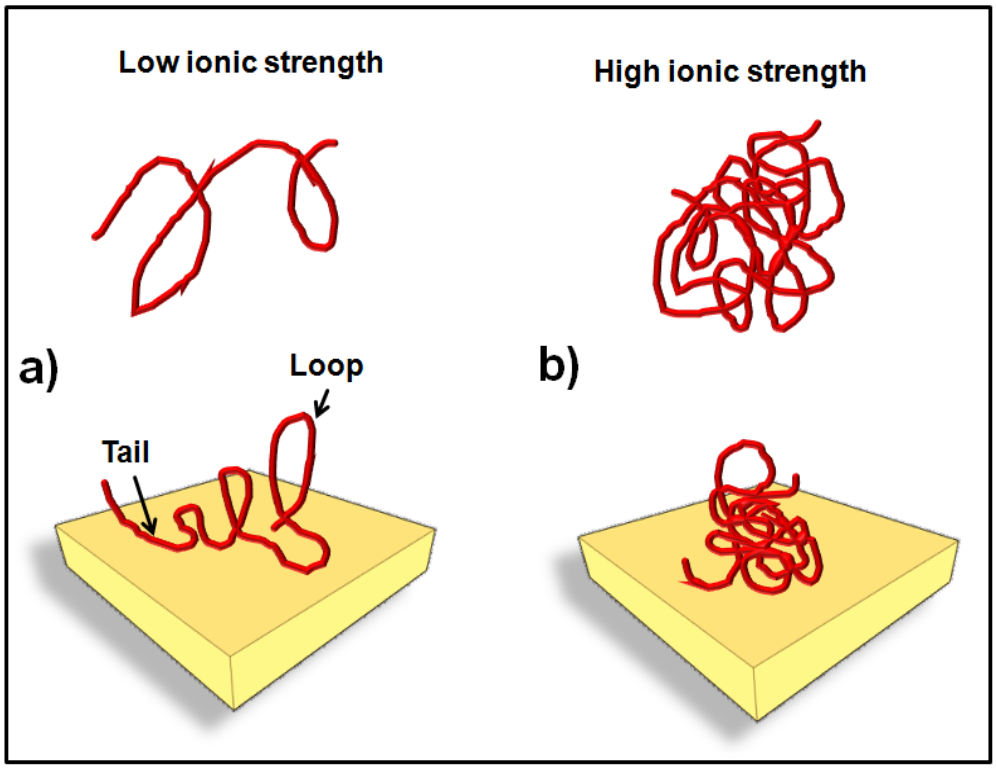

Fig. 3.1: Polyelectrolyte conformation depending on ionic strength in solution and in the adsorbed state is demonstrated [Butt03].

Currently, most of the fundamental work in the field of polyelectrolyte adsorption on a charged surface has been carried out with poly(styrene sulfonate) or PSS and poly(allylamine hydrochloride) or PAH [YoSh98, Dech92, Dech97, DechEc98, DechSlf03, Schf03a, Schf03b].

The structural formula of PSS and PAH are given in Figure 3.2. PSS is a negatively charged polyanion, whereas PAH is a positively charged polycation. PSS is a strong polyelectrolyte that totally dissociates upon dissolution in aqueous solutions and therefore, is fully negatively charged as it liberates Na^+ ions for a wide pH range.

PAH is a weak polyelectrolyte and the degree of dissociation/charging of its amine group depends on the pH value of the solvent. It is fully charged at pH ≤ 6 [Maus04, Glin07]. An isolated amine group at the end of a saturated hydrocarbon chain has a $pK_a \sim 10.6$. Because of the similarity of the chemical bonds in the vicinity of the amine group, this is also approximately the pK of an isolated amine group of PAH. In reality, the amine group is not isolated. The pK_a of PAH is lower (8.7) because of the mutual electrostatic interaction between neighboring amine groups which is unfavorable for deprotonation [Rieg02, Maus04].

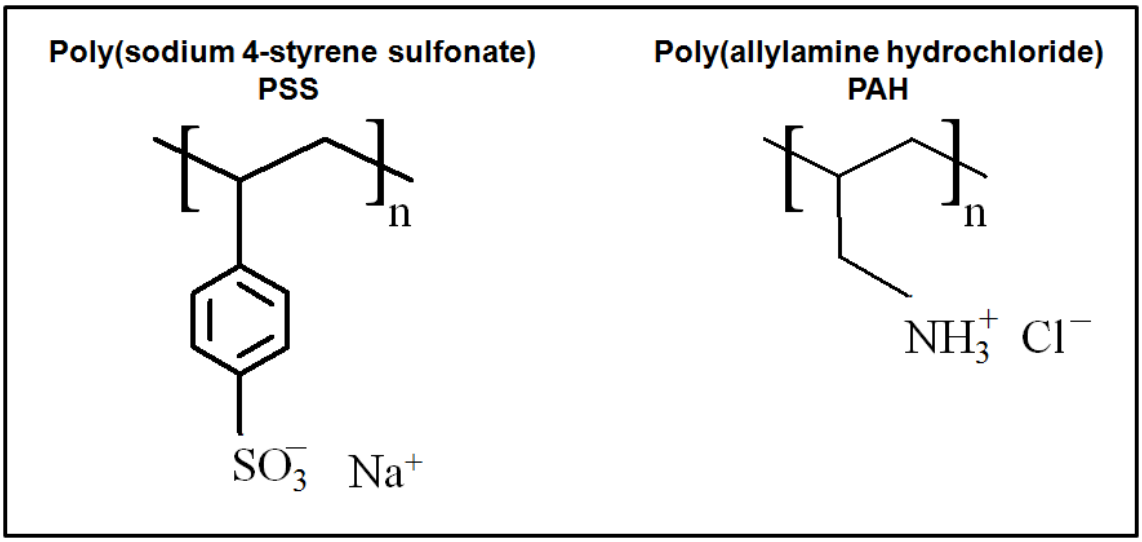

Fig. 3.2: Chemical structures of PSS and PAH.

3.1.1 Build-up of polyelectrolyte multilayer

The self-assembly of macromolecular thin films is becoming increasingly important with a wide field of applications such as the preparation of ion-permeable membranes [DaJen01], drug delivery systems [MaWin09], biosensor applications [AbPog10, NefWu07a], among others. The usual method used for formation of ultra-thin films with various degrees of molecular order and stability is the LbL technique. It is an economical and a readily available process for the fabrication of any kind of shape of large-area defect-free films on surfaces with unique properties.

The formation of PEM is based on the consecutive adsorption of polyions with alternating charge. Experimentally, the substrate is consecutively exposed to the respective PE solution for a time necessary for the adsorption of a single monolayer, followed by rinsing, and exposure to the next PE solution. These procedures are repeated until the desired number of layers is achieved [Dech92]. A schematic representation of the polyelectrolyte multilayer film built-up is given in Figure 3.3.

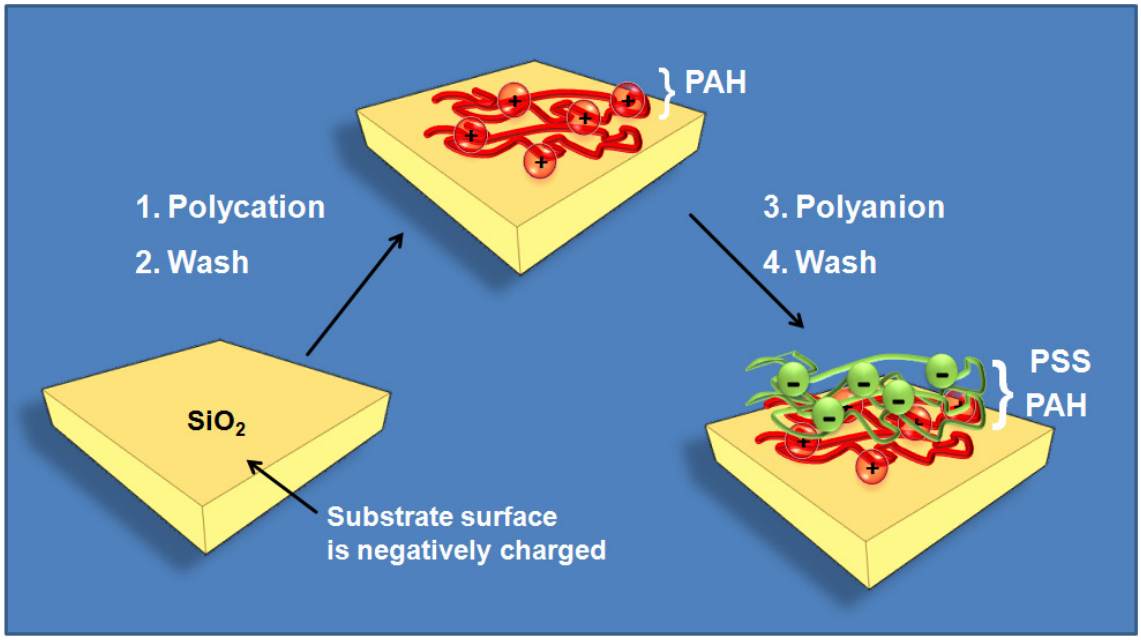

Fig. 3.3: Schematic representation of PEM build-up using LbL technique.

The main idea of this method is based on the charge overcompensation by polyion adsorption. It has been measured that only about one third of the terminating PE layer is complexed with charges from the underlying layer. The rest of the charges have to be screened by counterions or the charges from the next adsorbing layer. It is well accepted that the electrostatic interaction between the (opposite) charges of adjacent PE layers is the driving force for multilayer formation. This was supported by the fact that in electrokinetic measurements, the zeta potential changes its sign after each PE deposition step. It results in a kind of "zigzag" curve with the almost same amplitude [ScSchf02, Sukh98, DechEc98]. Provided that each adsorption step leads to a charge inversion of the terminated layer surface, the subsequent deposition finally results in a layered complex stabilized by strong electrostatic forces.

As mentioned earlier, small counterions render the total system (i.e., the substrate, the PEM, and the adjacent bulk solution) electrically neutral. The counterions indirectly (but strongly) influence the multilayer build-up by adjusting the conformation of the PE molecules in the bulk (through screening effects). It is suggested that the ion content depends on the charge density of the polyelectrolyte. If the average distance between the polyelectrolyte charges is less than the Bjerrum length ($l_B = e_0^2/(\varepsilon K_B T) = 7\text{Å}$), the multilayers contain small counterions, which are immobilized ("Manning condensation") on the polyelectrolyte [Mann78]. By low charge density of PE, multilayers are free of counterions because all ions are released upon film formation [Mann78].

The structure and conformation of PEMs are strongly dependent on the charge density of PEs, ionic strength as well as pH value of the exposed solutions.

3.1.1.1 Influence of ionic strength and charge density on the PEM formation

By the addition of salt to an aqueous PE solution, the thickness of the self-assembled films prepared from these solutions will be increased. The difference in film thickness can be explained by different conformations of the chains. Without salt, the polyelectrolyte chains are oriented flat and parallel to the substrate but with higher salt concentration of the aqueous solution, the chains form coils that are then adsorbed at the interface [Butt03].

Moreover, the charge density of PEs can influence the shape, thickness and morphology of the PEMs as follow [SteiJa01]:

With a charge density ≥75%, thick films are built-up and they become slightly thinner with increasing degree of charge. This is due to the transition from a more coiled to a flat chain conformation of the adsorbed chain because of the increasing electrostatic repulsion between the charges along the chain. This change in conformation is also considered in the decreasing roughness of the surface with increasing degree of charge. The larger roughness is due to chain loops at the surface, whereas chains with flat segments lead to a molecularly smooth surface.

- With a charge density ≤50%, only thin films are formed. In this regime, the change in surface charge after the adsorption of the polycation seems not to be high enough for the build-up of a multilayer system. These results suggest that a minimum charge of both the surface and the oppositely charged polyelectrolyte chain is necessary for the adsorption of the polyelectrolyte.
- In the case of fully charged polyelectrolytes, the film thickness changes dramatically with the salt concentration. The observed change in layer thickness is attributed to the increasing of charges' screening along the polyelectrolyte chain with increasing ionic strength, which induces an increasing coiling of the polyelectrolyte chains. Below a charge density of 50%, the ionic strength has no influence on the film thickness. Above the charge overcompensation threshold, the thickness can be fine-tuned by salt additive in the dipping solution.

3.1.1.2 Influence of pH on the PEM formation

The two most important parameters governing the adsorption of PEs on oppositely charged surfaces (PEM formation) in the absence of added salt are the linear charge density of the ad-

sorbing polymer chain and the surface-charge density of the substrate. This, in turn, provides an opportunity to systematically control the amount of polyelectrolyte layers adsorbed onto a surface, especially in systems containing weak PEs [Schf03b].

Since the degree of ionization of a weak PE and the surface charge density of a substrate can be controllably varied via pH changes in the solution, it is possible to systematically control the build-up of PEMs. This type of control is particularly useful during an LbL sequential process as it provides a very powerful means to control bi-layer composition, thickness and organization. Several experiments suggest a high level of interpenetration in sequentially adsorbed layers based on weak polyelectrolytes. It is estimated that segments from a particular polymer layer can penetrate into as many as one to three of their surrounding bilayers [Schf03b].

3.2 DNA structure

DNA is a nucleic acid that contains the genetic information of the biological functions of all living forms and some viruses. Nucleic acids are macromolecules composed of repeating subunit-nucleotides. A schematic structure of the DNA molecule is presented in Figure 3.4. Each nucleotide is composed of a phosphate group, a five-carbon sugar (or pentose), and a cyclic nitrogen-containing base. Four different bases are commonly found in the DNA molecular structure, namely adenine (A), guanine (G), thymine (T) and cytosine (C). A and G are double ring bases called purines; C and T are single-ring bases called pyrimidines. In the DNA, these subunits are joined together in long chains. One of the most existing breakthroughs in the history of biology occurred in 1953 when James Watson and Frasic Crick deduced the correct structure of DNA. Their double helix structure of a DNA molecule immediately suggested an elegant mechanism for the transmission of genetic information [SnSi06].

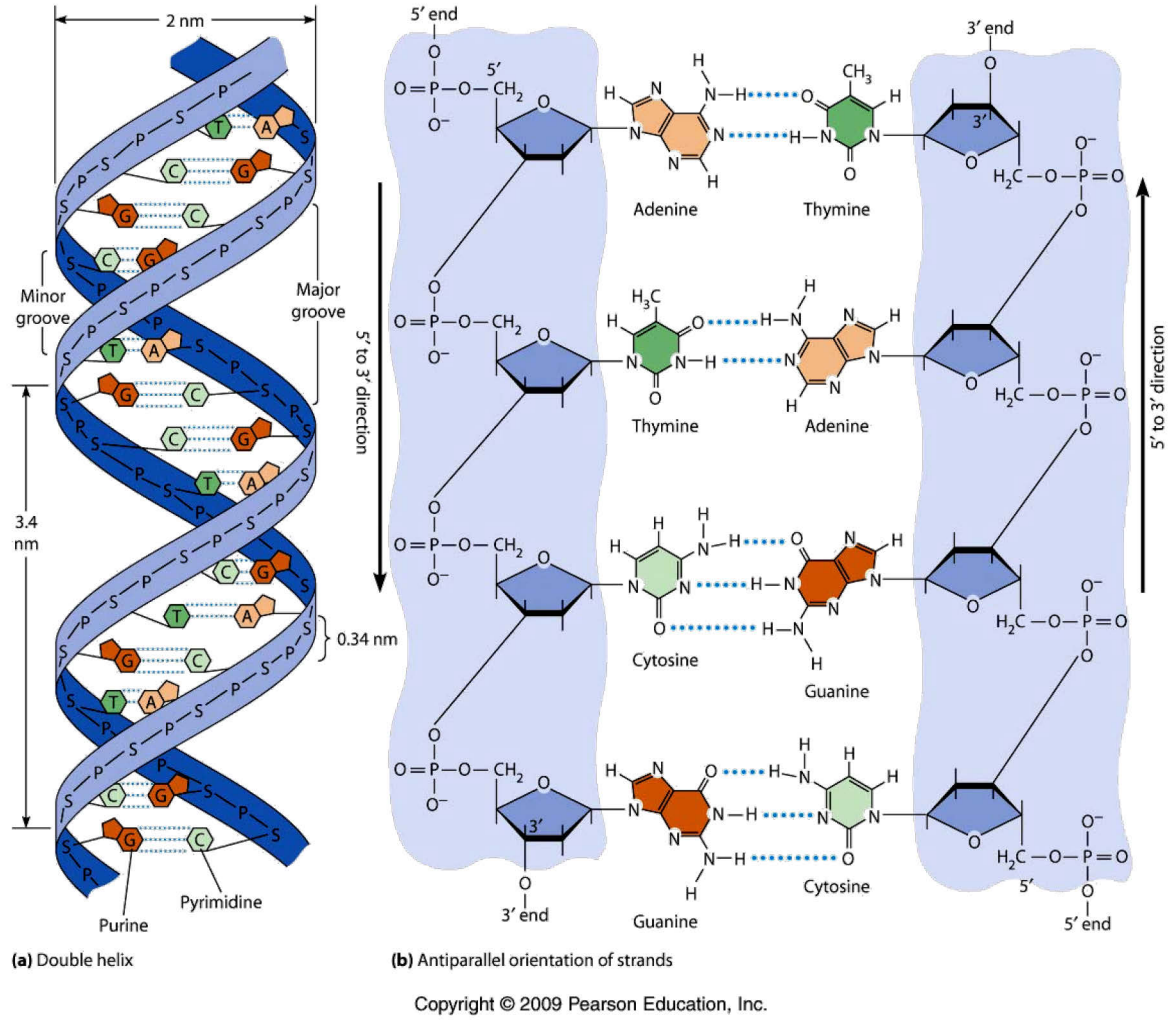

Fig. 3.4: Schematic structure of DNA molecule, illustrating the opposite chemical polarity of two strands and the hydrogen binding between A and T as well as between C and G (from [WaBe09]).

The double helix of DNA has the following features (see Fig. 3.4) [WaBe09, SnSi06]:

- It contains two polynucleotide strands wind around each other.
- The backbone of each strand consists of alternating deoxyribose and phosphate groups.
- The phosphate groups act as a bridge between the consecutive sugars forming the linear polymers.
- The two strands are "antiparallel"; that means, one strand runs from 5′ to 3′ while the other runs from 3′ to 5′.
- The purine or pyrimidine attaches to each deoxyribose towards the axis of the helix.
- In double-stranded DNA (dsDNA), base pairs are formed through hydrogen bonds between A and T and between G and C.

- The double helix makes a complete turn in just over 10 nucleotide pairs, so each turn takes the 34 Å as shown in Fig. 3.4.
- There is an average of 25 hydrogen bonds within each complete turn of the double helix providing a stability of binding about as strong as what a covalent bond would provide.
- The diameter of the helix is about 20 Å.
- The path taken by the two backbones form a major (wider) groove and a minor (narrower) groove.

3.2.1 DNA hybridization and denaturation events

The reaction of one strand of DNA matching up with its counterpart strand is called hybridization. By knowing the molecular structure of one ssDNA, one can determine the other (complementary) single strand. A technique that is used to determine a base-pair sequence in a DNA sample is called genetic sequencing. Hybridization can be performed either in solution or on a solid support [Web6]. The rate of the DNA hybridization depends on DNA concentration (the higher the DNA concentration, the faster the hybridization), temperature, ionic strength and pH value of the hybridization solution, etc. [SnSi06, Web6].

Denaturation occurs when the hydrogen bonds of the double helix are broken and the two DNA strands separate from each other. Breaking of the hydrogen bonds is usually done by temperature increase or with high concentrated alkaline or low ionic-strength solutions. If a solution of native (double-stranded) DNA is heated slowly under carefully controlled conditions, the DNA "melts" over a narrow temperature range [SnSi06, Web7].

When the solution is allowed to cool, the separated DNA strands reassociate with kinetics that depend on the initial concentration. Complementary strands collide randomly in the nucleation event, followed by a rapid "zipping up" of adjacent nucleotide pairs. The reassociation requires varying amounts of time, depending on both the DNA concentration in the solution and the length of the DNA strands [SnSi06].

The melting temperature (T_m) of an oligonucleotide is the temperature at which 50% of the oligonucleotide and its perfect complement are present in duplex form. Typically, annealing or hybridizations are performed at 5 °C-10 °C below the T_m of a duplex. The simplest equation for T_m calculation in °C is the Wallace rule [RyRh89, Web7]:

$$T_m = 2(N_A + N_T) + 4(N_C + N_G) \quad (3.1)$$

where N_A, N_G, N_C, and N_T are the number of incidences of each nucleotide in the oligo. This equation was developed for short DNA oligos of 14-20 bases hybridizing to DNA targets immobilized on a substrate in 0.9 M NaCl.

If both target and probe are free in solution, T_m is approximately 7-8 °C lower than when the target is immobilized on a membrane [WalSh79, Web7]. T_m is dependent on the ionic strength (the higher the electrolyte concentration, the higher T_m, because the positive Na^+ ions shield the negative charges on the phosphodiester backbone from repelling each other), the base composition (the higher the percent of G-C pairs (%G-C), the higher T_m), length of molecule (the higher the length the higher T_m), the pH value (DNA denatures at pH>12), and the presence of helix-destabilizing agents (urea, formamide) [RyRh89, Web7].

Chapter 4

4 Fabrication and characterization of EIS and EISOI sensors

The fabrication procedure of the EIS sensors and the EISOI sensor array are described in this chapter. The physical characterization of the fabricated sensors by means of ellipsometry and scanning electron microscopy together with the electrochemical characterization of bare sensors by means of *C-V*, constant-capacitance and impedance-spectroscopy methods are also explained in this chapter. The introduction of an electrical equivalent circuit accounts for the *C-V* and impedance-spectroscopy behavior of the EISOI sensors. In addition, proof of the pH sensitivity of bare sensors is also discussed. Some of results described in this chapter are published in [AbMor11, AbIn09a, AbIn09b].

4.1 Fabrication of EIS structure and nanoplate EISOI sensor array

For fabrication of EIS structures (Al/p-Si/SiO_2), 30 nm SiO_2 layer was grown on the Si (p-Si <100>, boron-doped, ρ= 1-10 Ωcm) wafer. The thickness of the SiO_2 film was determined by means of ellipsometry. After etching of the SiO_2 layer from the rear surface of the wafer, a contact layer of 300 nm Al was deposited on the rear-side of the p-type wafer. The wafer was then covered with a photoresist layer in order to protect the front surface from the cutting procedure, and cut into chips with a square surface of about 10×10 mm^2.

The nanoplate capacitive sensor array with a 350 nm thick top Si layer was fabricated from an SOI wafer (SOITEC, France) with a 360 nm thick top Si layer (p-Si <100>, boron doped,

ρ= 14-20 Ωcm) on a 400 nm thick BOX layer. For the fabrication of the field-effect-based capacitors, first a high-quality thermal silicon dioxide layer (30 nm) was grown on the top Si layer (Fig. 4.1, step 1). In the second step, the top SiO_2 layer was structured by optical lithography (for photomask design, see appendix B) and etched (wet etching) with an ammonium fluoride etching mixture AF 91-9, PURANAL (Honeywell Specialty Chemicals Seelze GmbH, Germany). For isolation of individual nanoplate capacitors, the top Si layer was anisotropically etched in 12.5% TMAH (tetramethylammoniumhydroxid) at 90 °C (etching rate of 1.2 $\mu m.min^{-1}$) [Taba92] using the structured top SiO_2 layer as a mask (Fig. 4.1, step 2). In the third step, the top SiO_2 layer was structured again by optical lithography and etched to open contact windows to the top Si layer (Fig. 4.1, step 3).

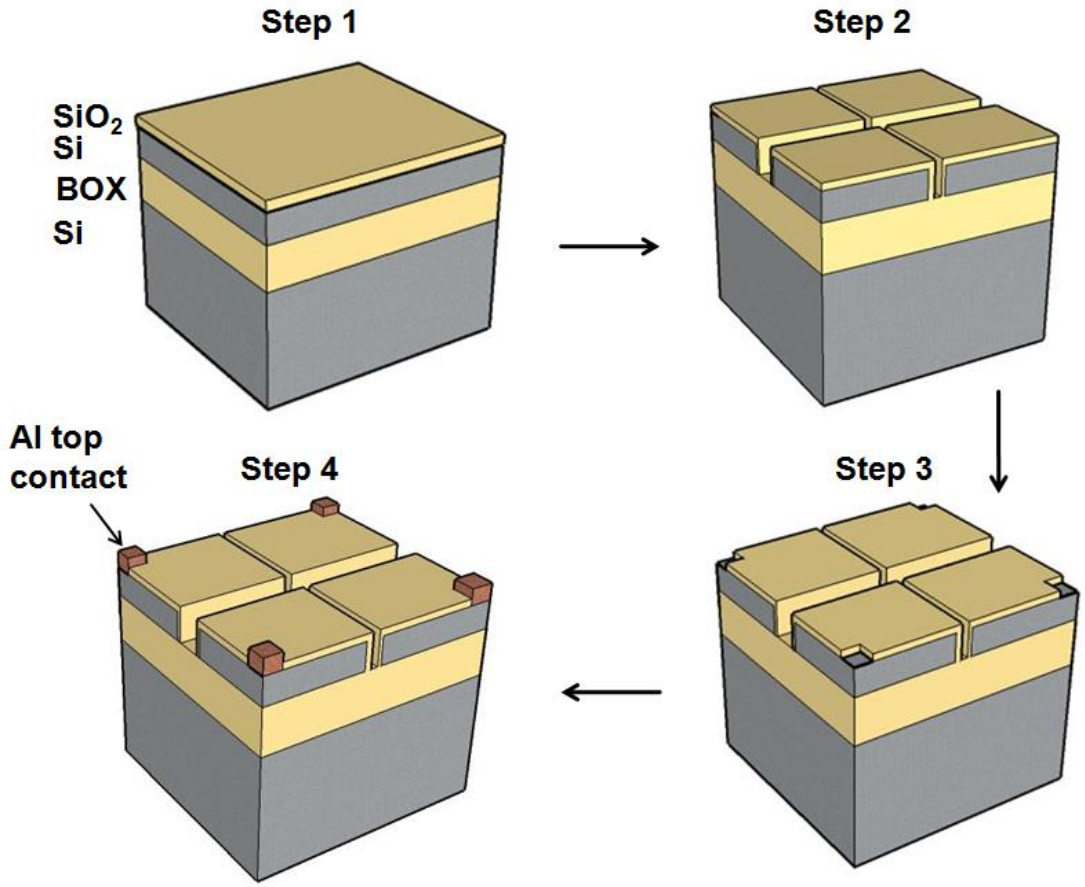

Fig. 4.1: Flowchart for the fabrication of a nanoplate EISOI sensor array.

As a contact layer, 300 nm Al was deposited in front of the top Si layer followed by lift-off and annealing processes (Fig. 4.1, step 4). Finally, the wafer was cut into 12 mm × 12 mm chips. Each chip consists of four electrically isolated nanoplate capacitive field-effect-based

sensors. Figure 4.2 shows the top-view and cross-section SEM micrograph of the layer structure of the fabricated SOI-based nanoplate capacitor.

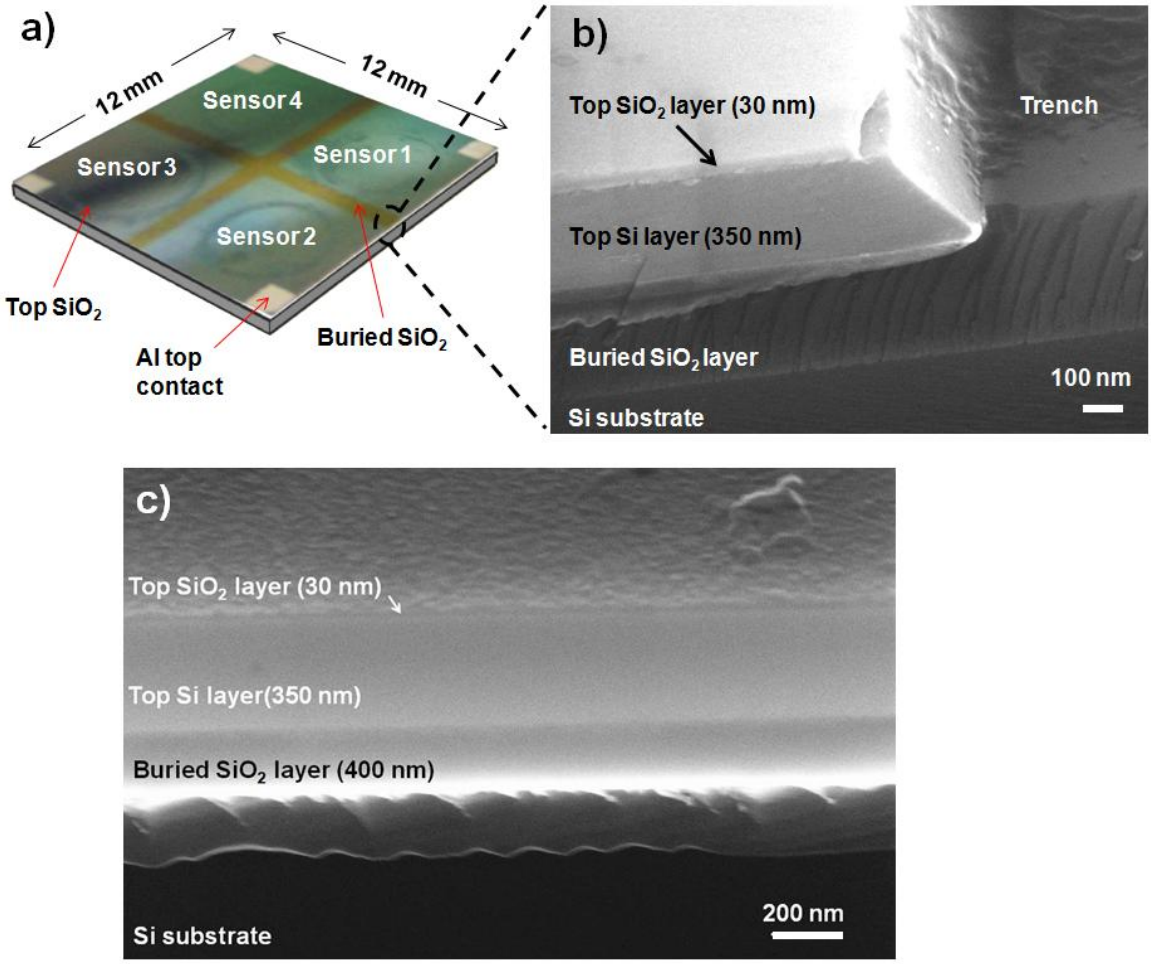

Fig. 4.2: Top view of the realized nanoplate EISOI sensor array (a) and cross-sectional SEM picture of the EISOI sensor layer structure (b, c).

4.2 Measurement setup and methods

For electrochemical characterization, the sensor chips were mounted into a home-made measuring cell (Fig. 4.3 and Fig. 4.4), sealed by an O-ring, and contacted on their front side by the electrolyte and a reference electrode (for EISOI measuring-cell design, see appendix C). The rear side (in the case of EIS sensors) or front-side contact on the upper surface of the top Si layer (in the case of nanoplate EISOI capacitors) was attained by the use of a gold-plated pin (see Fig. 4.5a, and 4.5b).

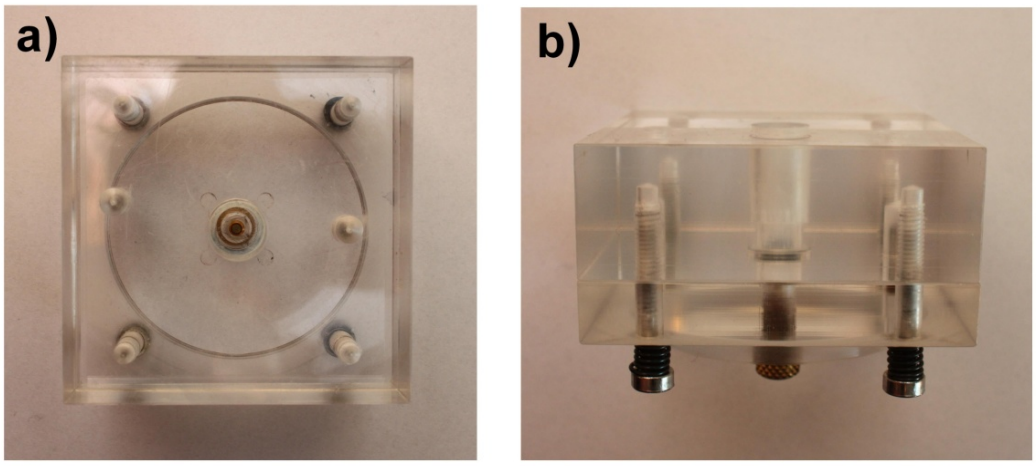

Fig. 4.3: Top (a) and side view (b) of the measurement cell for an EIS sensor.

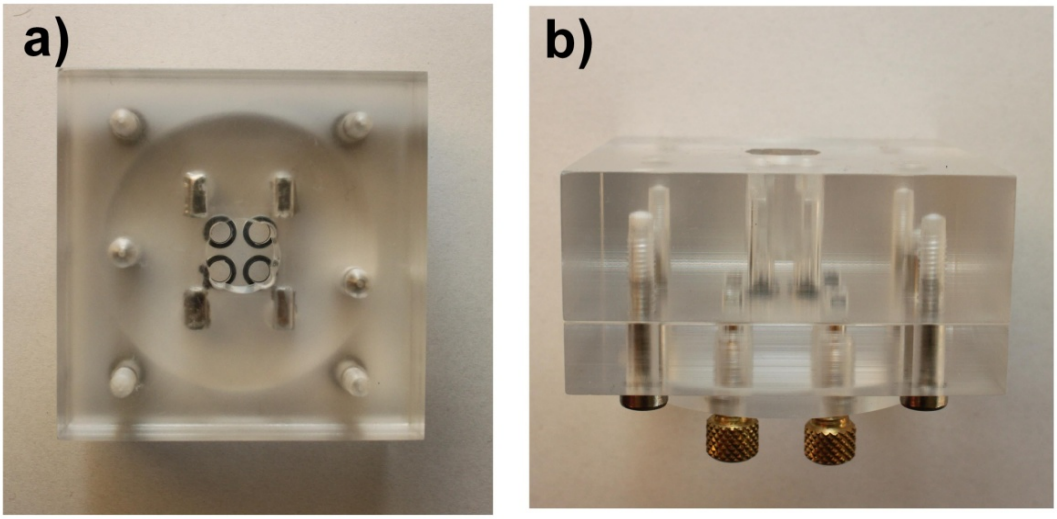

Fig. 4.4: Top (a) and side view (b) of the measurement cell for an EISOI sensor array.

The area of the sensor in contact with the electrolyte is determined by the diameter of the O-ring and was about 0.65 cm^2 and 0.19 cm^2 for the EIS and EISOI sensors, respectively. A conventional Ag/AgCl electrode (Metrohm 6.0733.100 Ag/AgCl, 3 M KCl) was used as a reference electrode. The measurements have been performed in a dark Faraday cage at room temperature. All potential values are referred to the reference electrode.

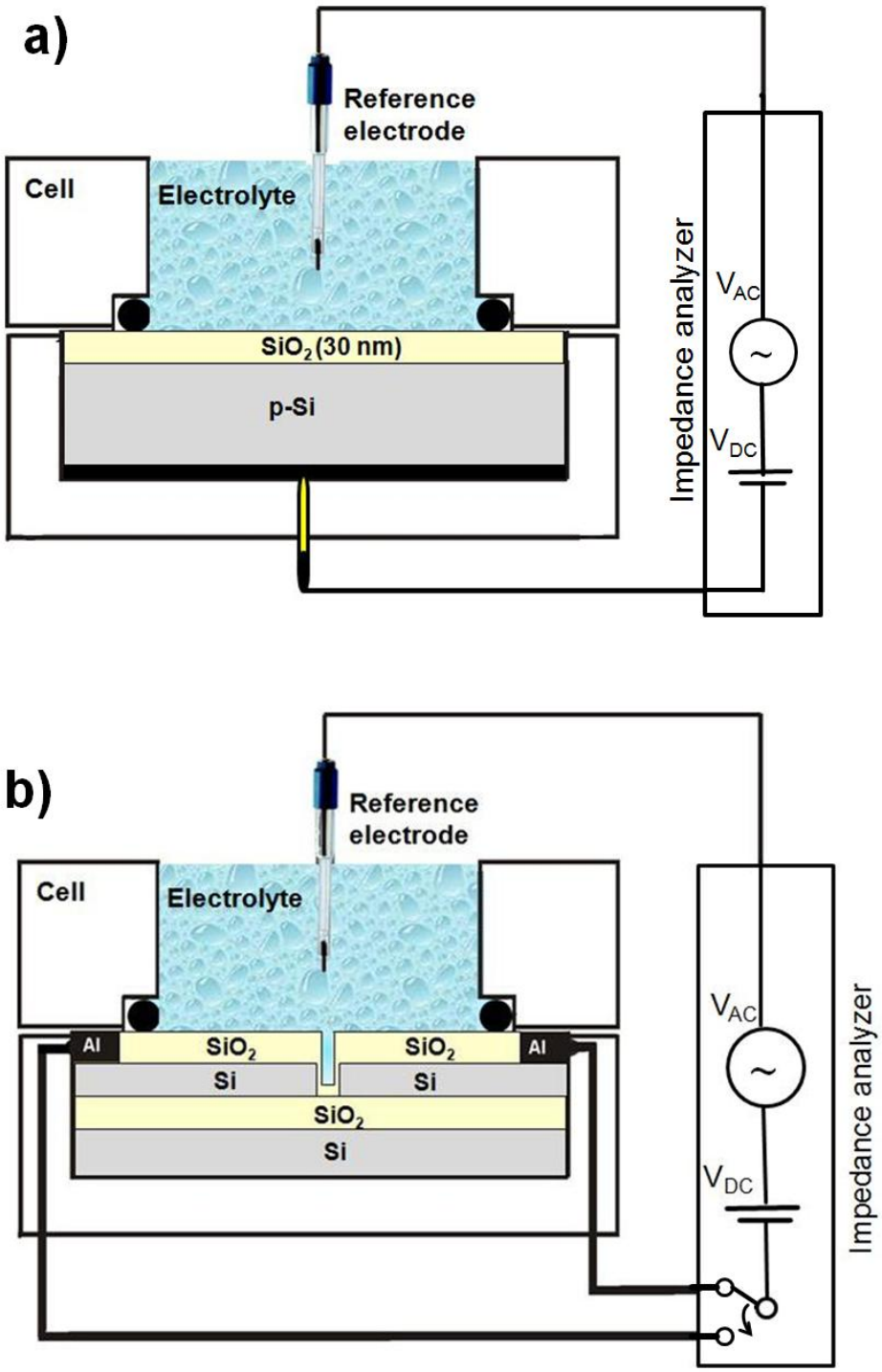

Fig. 4.5: The structure and measuring setup of the capacitive EIS sensor (a) and the capacitive EISOI sensor array (b).

For the electrochemical characterization of EIS sensors and the EISOI sensor array, three methods are used: *C-V*, constant-capacitance (ConCap) and impedance-spectroscopy (IS) methods. For the *C-V* measurements, a small ac voltage (20 mV) and a dc polarization voltage via the reference electrode was applied to the sensors. The impedance analyzer (IM6, Zahner

Elektrik, Germany) measures the whole impedance of the structure and separates the resistive from the capacitive component of the current.

The schematic *C-V* curves of a p-type EIS sensor are given in Figure 4.6a. The *C-V* curves show three different regimes, namely the accumulation, depletion and inversion. In the accumulation operating mode, the capacitance of the insulator layer is significantly smaller than the space-charge capacitance; the capacitance of the whole EIS structure is mainly determined by the geometrical capacitance of the insulator, $C=C_i$. For a capacitive field-effect sensor application, the more useful range represents, however, the depletion region of the *C-V* curve. Since the objective is to characterize the (bio-)chemical sensitivity of the EIS system, it is essential to maintain the conditions at the gate-insulator/semiconductor interface in a constant state so that the measured changes, for instance, concentration-dependent and/or molecular-charge-dependent shifts of the *C-V* curves, can be attributed entirely to the reactions at the electrolyte/insulator interface. The response of a sensitive EIS structure with respect to the electrolyte composition and/or adsorption of charged macromolecules, as explained in section 2.1, depends on its flat-band voltage shift at the working point (Eq. 2.5) which can be accurately determined from the *C-V* curves (Fig. 4.6a) [PogSchg06].

In contrast to the *C-V* method, the ConCap measuring mode allows the investigation of the dynamic behavior of the sensor signal. In the ConCap mode, setting the capacitance at a fixed value (ideally at the flat-band capacitance; usually within the linear region of the *C-V* curve at ~60-70% of the maximum capacitance depending on the shape of the high-frequency *C-V* curve) by using a feedback-control circuit shifts the voltage, which can be directly recorded resulting from the potential change at the sensor surface (Fig. 4.6b). The potential change at the sensor surface can be caused by a change of pH or ion concentration of electrolyte or binding of charged macromolecules. To obtain the calibration curve of the sensor, the measured voltage values are plotted against the corresponding analyte concentration or molecular charge (Fig. 4.6c) [PogSchg06].

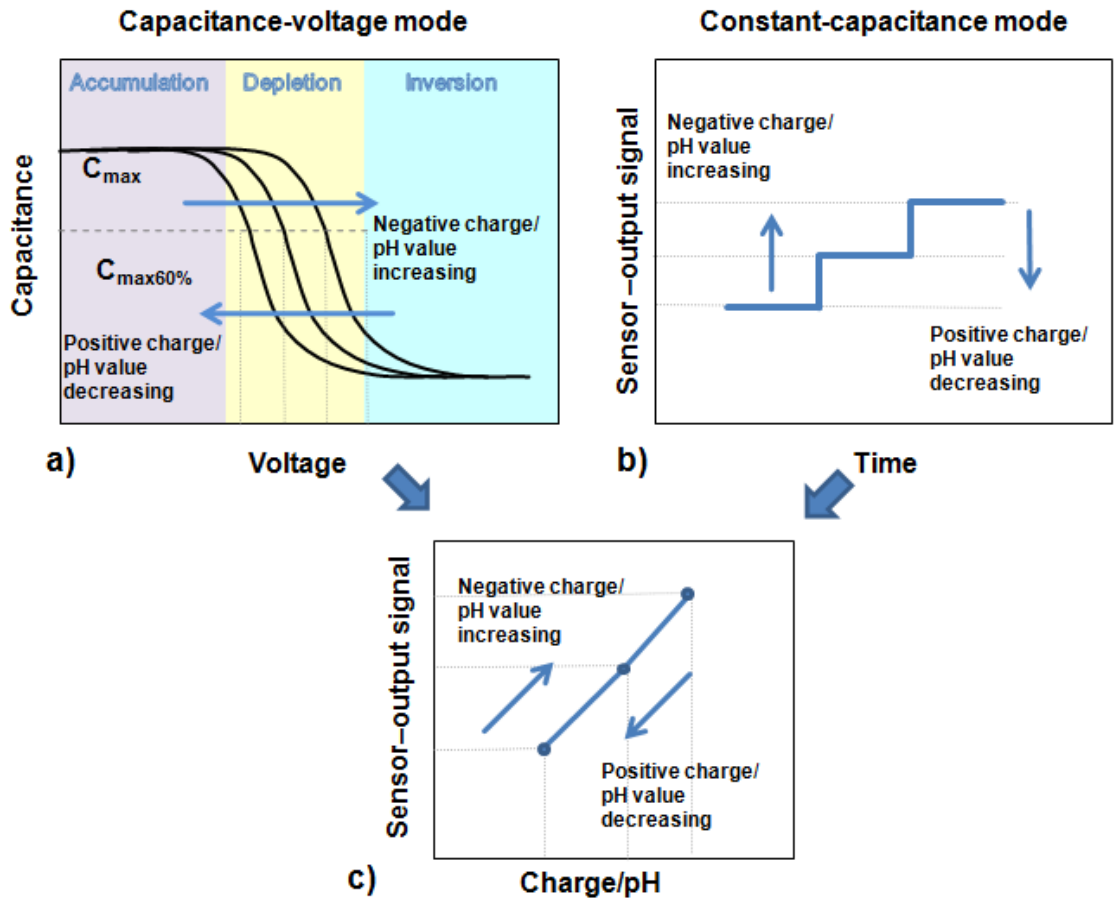

Fig. 4.6: Typical high-frequency *C*-*V* curves (a) and ConCap response (b) of a p-type EIS sensor for different pH values. To obtain the calibration curve (c) of the sensor, the measured voltage values are plotted against the corresponding pH values or surface-charge changes.

Another method that was used for electrochemical characterization of the sensors utilized in this work is IS. This is a very useful method for characterizing the electrical properties of materials and interfaces [Park03, PogMa04, KraMor06].

Impedance is the totally complex resistance. It depicts a measure of opposition to alternating current that flows through a circuit made of resistors, capacitors or inductors. The phase shift and the magnitude of the alternative current can be determined by the configuration of the electronic components in the system. The electrochemical impedance can be measured by the current that passes through the cell, when an ac small potential is (e.g., sinusoidal excitation) applied to this cell (see Fig. 4.7) [Web4].

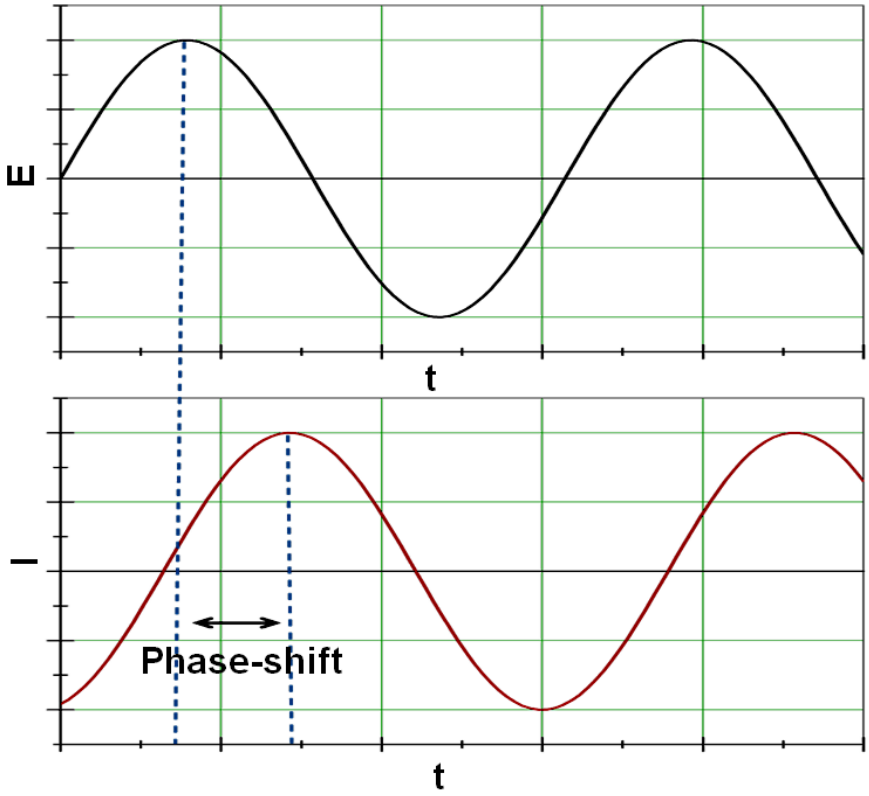

Fig. 4.7: Sinusoidal current response in a linear system (adopted from [Web4]).

The applied excitation ac potential has the form [Web4]:

$$E_t = E_0.\sin(\omega t) \tag{4.1}$$

where, E_t is the potential at time t, E_0 is the signal's amplitude, and ω is the radial frequency. The relationship between radial frequency ω (expressed in radians/second) and frequency f (expressed in Hertz) is [Web4]:

$$\omega = 2\pi f \tag{4.2}$$

In a linear system, the response signal (I_t), is shifted in phase (Φ):

$$I_t = I_0.\sin(\omega t + \Phi) \tag{4.3}$$

The impedance of the system (Z) can be calculated using Ohm's law as [Web4]:

$$Z = \frac{E_t}{I_t} = \frac{E_0.\sin(\omega t)}{I_0.\sin(\omega t + \Phi)} = Z_0.\frac{\sin(\omega t)}{\sin(\omega t + \Phi)} \tag{4.4}$$

The impedance is therefore expressed in terms of a magnitude (Z_0) and a phase shift (Φ).

To display the impedance characteristics, either a Bode plot of the absolute magnitude of the impedance ($|Z|$) versus frequency, or the well-known Nyquist plot or an impedance plane plot of $Z'' = |Z|.\sin(\Phi)$ (the imaginary or capacitive component of the impedance) versus $Z' = |Z|.\cos(\Phi)$ (the real or resistive component of the impedance) have usually been used. Each point in the Nyquist plot is the impedance at one frequency [Mac87].

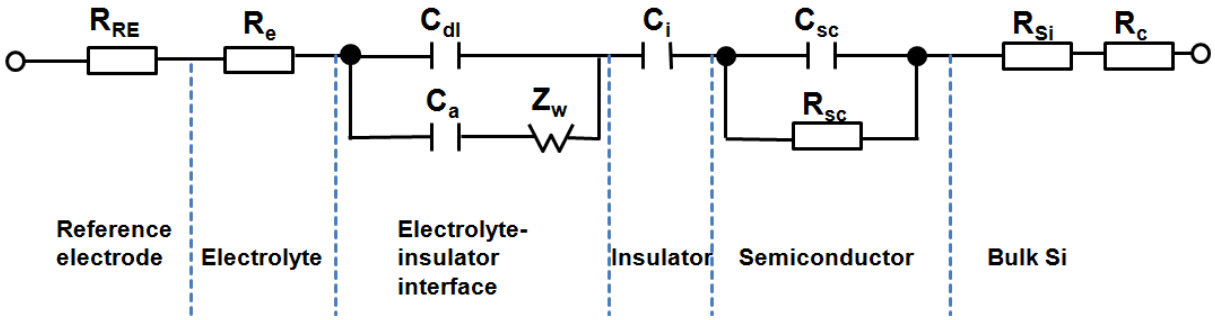

Fig. 4.8: The equivalent circuit of an EIS sensor (adopted from [BousB83]).

Very few electrochemical cells can be modeled using a single equivalent circuit element [Mac87, Web4]. Usually, IS models consist of a number of elements in network with both serial and parallel combinations of elements. The impedance characteristics of MIS and EIS structures are well studied [Dem95, Mac87, Bous83, Diot85, BousB83]. Figure 4.8 demonstrates a general equivalent circuit for an EIS structure. The equivalent circuit consists of the reference electrode's resistance (R_{RE}), the electrolyte resistance (R_e), the electrolyte-insulator interface impedance (it consist of double-layer capacitance, C_{dl}, a diffuse impedance Z_w and SiO_2/electrolyte interface capacitance, C_a), the insulator capacitance (C_i), space-charge capacitance in the semiconductor (C_{sc}) and space-charge resistance in the semiconductor (R_{sc}). The components of this model can be reduced depending on the applied voltage, applied frequency and system parameters [Mac87] (see next section).

In this work, the IS method was especially used for the characterization of the developed EISOI sensor array. An electrical equivalent circuit for the EISOI structure was developed and discussed, which explains the *C-V* and IS behavior of the EISOI sensors (sections 4.3.1 and 4.3.2). In addition, the IS method was applied to study the change of the phase and impedance via PEM build-up on EIS sensors (section 5.2.3).

4.3 Electrochemical characterization of EIS and EISOI sensors

4.3.1 Capacitance-voltage curves

Typical *C-V* curves of an EIS sensor as well as of an EISOI sensor recorded in pH 7 buffer solution at different frequencies from 30 Hz to 1000 Hz are presented in Figure 4.9. At a low frequency of f=30 Hz, the *C-V* curve of both the EIS and the EISOI structures shows the well-known low-frequency behavior with typical accumulation, depletion and inversion regions. The maximal capacitance in the accumulation region is frequency-dependent, whereas with increasing the frequency, the *C-V* curves shift along the capacitance axis towards smaller maximum capacitance values. This effect is a direct indication of a series resistance "problem" [Lun06, Est96]. Similar effects have been observed in EIS structures modified with high-resistive ion-selective membranes [Dem95, FaLa90, MoMa03] as well as in MIS structures with high-resistive substrates [Lun06, Est96].

At the same time, however, there are significant differences between the *C-V* curves of EIS and EISOI structures [AbMor11]:

- **First observation:** In comparison to an EIS sensor, the *C-V* curves of the EISOI structures show a stronger frequency dependence in the accumulation region. To explain this effect, an equivalent circuit of the EISOI structure should be considered.

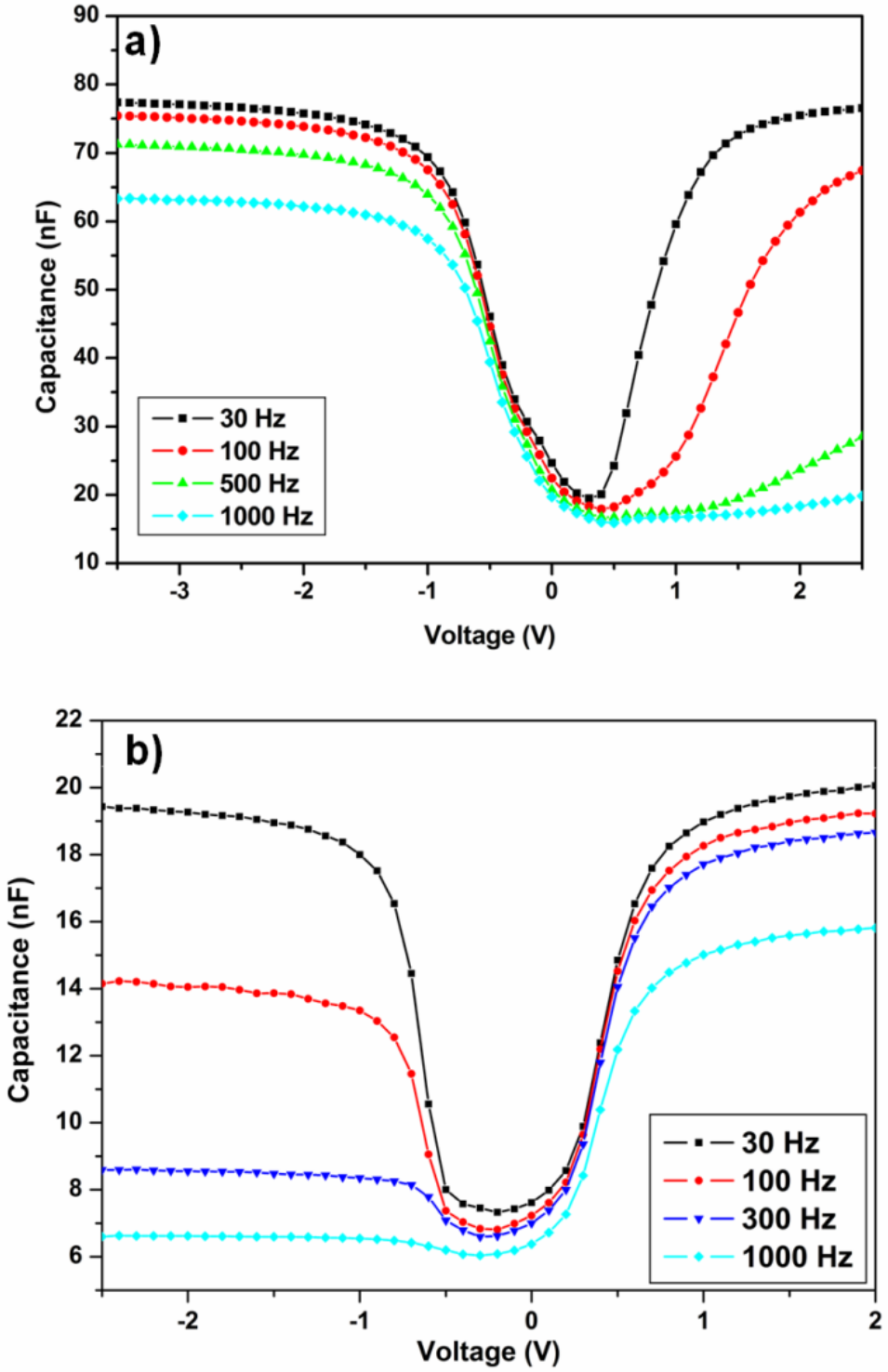

Fig. 4.9: Frequency-dependent *C-V* curves of an EIS (a) and an EISOI sensor (b).

The complete ac equivalent circuit of an EIS system is complex (see Fig. 4.8) and combines several components. However, for usual values of insulator thickness (10-100 nm) and electrolyte concentration (>10^{-4}-10^{-5} M) used, the interferences from several components are negligible [Berg91, Dem95]. Therefore, the equivalent circuit of an EIS system can be simplified as a series connection of C_i, C_{sc}, and the equivalent resistance (R=R_c+R_{Si}+R_{RE}) consisting of Al-Si contact resistance (R_c), bulk resistance of Si (R_{Si}), and resistance of the reference electrode (R_{RE}). As it has been demonstrated in [Dem95, FaLa90, MoMa03], the existence of any series resistance can lead to a frequency-dependent deformation of the C-V plots of the capacitive field-effect structure and even to practically flat curves at high frequencies.

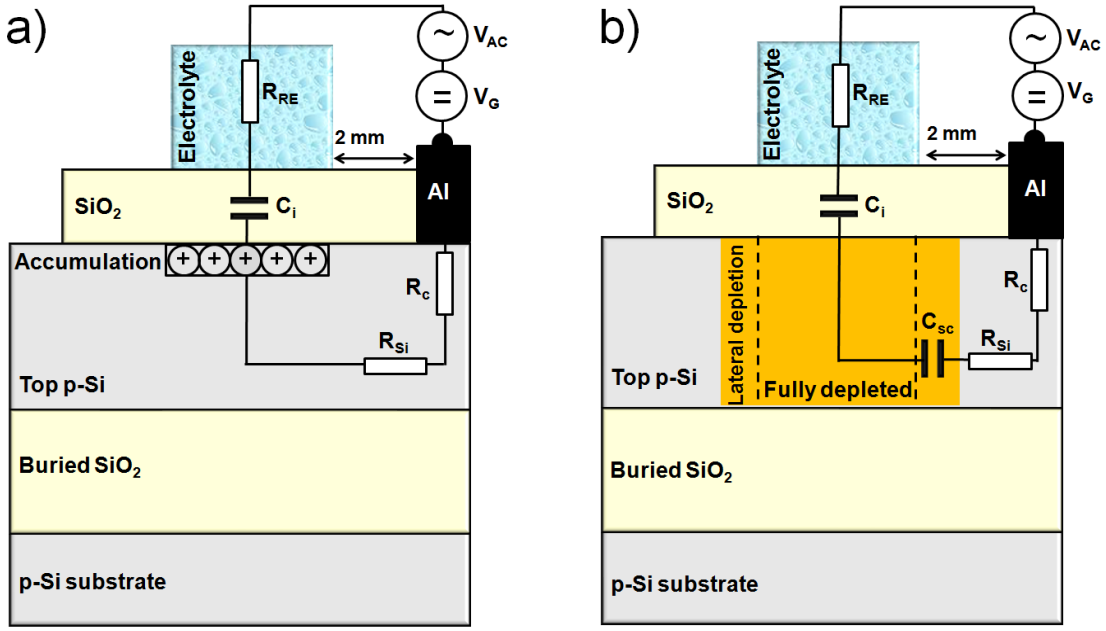

Fig. 4.10: Schematic of an EISOI structure with embedded simplified equivalent circuit in the accumulation (a) and depletion (b) region.

Figure 4.10 shows the schematic of an EISOI structure with the embedded simplified equivalent circuit in the accumulation (a) and depletion (b) region. If a large negative potential is applied to the reference electrode, an accumulation layer of positively charged holes is formed near the Si-insulator interface, and the total capacitance is determined by the insulator capacitance, C=C_i. The measured capacitance (C_m) will be given by:

$$C_m = \frac{C_i}{1+(2\pi f R C_i)^2} \tag{4.5}$$

As far as the condition $R << \frac{1}{2\pi f C_i}$ is met, the measured C_m will be equal to the real insulator capacitance. If this condition is not satisfied, the measured capacitance in the accumulation range will be affected by a series resistance. As a result, the measured capacitance can be much smaller than the real capacitance of the system.

For the EIS structures used in this study, R_{Si} is very small. The estimated values for R_c using the Al-Si specific contact resistance of 700-800 Ωcm^2 [Sze81] and a contact area of 1 cm^2 and 0.2 cm^2, respectively, were about 0.7 kΩ and 4 kΩ for the EIS and EISOI structures. The R_{RE} is in the range of 5-10 kΩ. Thus, the frequency-dependent *C-V* curves of the EIS structure will mostly be affected by the series resistance of the reference electrode. In contrast, due to the higher resistivity and smaller thickness of the top Si layer and the larger distance (2 mm) between the Al-Si contact and gate electrolyte region, the frequency-dependent *C-V* curves of an EISOI structure will mostly be affected by the large lateral resistance R_{Si}, resulting in a stronger frequency dependence, compared to the EIS capacitor.

Similar to EIS or MIS devices in the depletion region, the total capacitance of the EISOI structure can be modeled as a series connection of C_i and the depletion capacitance, C_{sc}. The measured frequency-dependent total capacitance in the depletion region will be given by:

$$C_m = \frac{C_i(1 + C_i / C_{sc})}{(1 + C_i / C_{sc})^2 + (2\pi f R C_i)^2} \tag{4.6}$$

As the total capacitance decreases with increasing the gate voltage (see Fig. 4.9), the measured C_m will get closer to the real value of the capacitance of the EISOI structure. The minimum value of capacitance (C_{min}) is usually defined by the maximum width of the depletion layer (w_m) [Sze81, Cobb70]:

$$C_{\min} = \frac{\varepsilon_i}{d + (\varepsilon_i / \varepsilon_s) w_m} \tag{4.7}$$

where ε_i and ε_s are the relative dielectric permittivity of SiO_2 (3.9) and Si (11.9), and d_i is the thickness of the gate insulator. In our capacitive EISOI sensor array, the thickness of the top Si (d_{Si}= 350 nm) is smaller than the maximum depletion width (0.8-1 µm [Sze81]), therefore, the top Si is fully depleted (see Fig. 4.10b), and $C_{sc} = \varepsilon_s / d_{Si}$ (the maximum width of the deple-

tion layer in the top Si layer is limited by the Si thickness). In the experiments performed in the study, the maximum depletion width will be defined by both the width of the lateral depletion layer and the thickness of the top Si layer due to the formation of an additional lateral depletion layer (see Fig. 4.10b).

- **Second observation:** In contrast to an EIS sensor, which shows a typical high-frequency *C-V* characteristic already at f>0.5-1 kHz (see Fig. 4.9a), it was not possible to achieve the high-frequency *C-V* behavior in the inversion region for EISOI sensors at a frequency of f=1 kHz (see Fig. 4.9b) and even at higher frequencies (up to 8 kHz, not shown). The following two mechanisms could be responsible for such a *C-V* behavior of EISOI structures:
  - It is known, that the frequency response of MIS capacitors in the inversion region depends on the rate (or response time) at which minority carriers (in our structures, electrons) can be supplied to, or removed from, the inversion layer. If the response time of the minority carriers is fast at high frequencies, the supply of charge carriers to the inversion layer is sufficiently rapid and therefore, the inversion charge can follow variations of the applied ac voltage. It has been demonstrated that in high-resistivity Si, the minority carriers respond much faster than in low-resistivity substrate [Ron03, Lun06, Est96, Nico82]. In our experiments, the resistivity of the top nanoplate Si in the EISOI structures is several times higher than that of the bulk Si substrate in EIS structures. As a consequence, even at high frequencies, the *C-V* curve of EISOI structures in the inversion region possesses a low-frequency behavior.
  - Another explanation could be the relatively small gate-contact area (0.19 cm^2) of the EISOI structures with the electrolyte solution, while the SiO_2 layer covers practically the whole top Si surface besides the Al contacts. As it has been discussed [Cobb70] for p-type FEDs, where the oxide layer extends over an area greater than the gate-contact area, the transition frequency between the low and high frequency *C-V* characteristics can be very high.

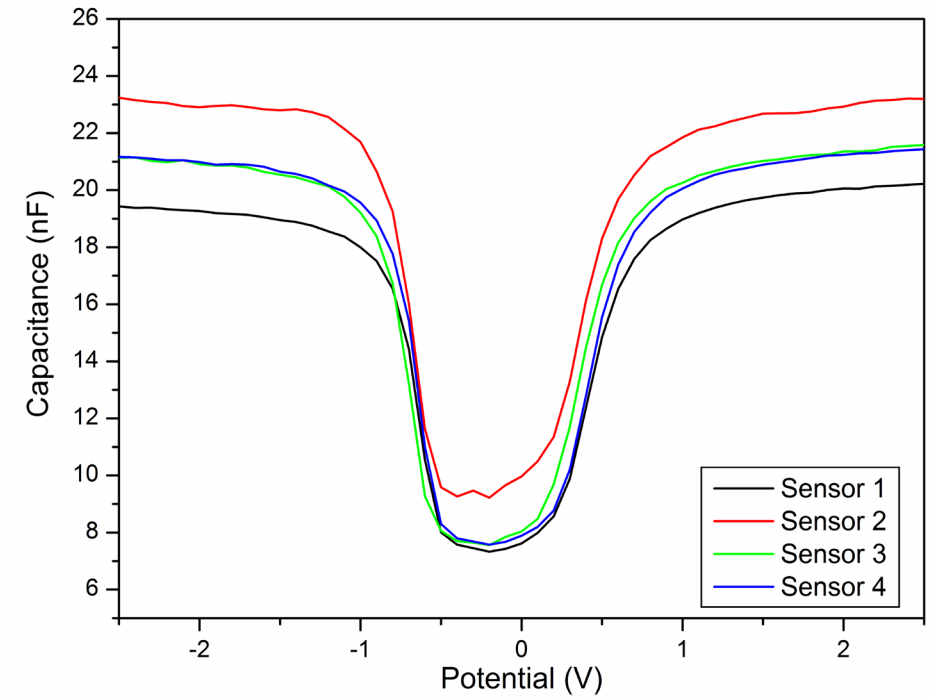

Fig. 4.11: *C-V* curves of the four EISOI sensors on the same chip measured in pH 7 buffer solution at a frequency of 30 Hz.

Fig. 4.11 shows exemplary *C-V* curves of all four EISOI sensors on the same chip recorded in pH 7 buffer solution at a frequency of 30 Hz. As can be seen, the maximum capacitance values of the sensors in the array in the accumulation range differ from each other. This can be attributed to discrepancies of the top Si [Sze81], SiO_2 layer thickness and/or different quality of the top Al/Si contacts.

4.3.2 Impedance spectroscopy

The impedance spectra for both developed capacitive EIS sensor and nanoplate EISOI sensor array were recorded in the accumulation, depletion and inversion ranges by applying different polarization voltages (see Fig. 4.12).

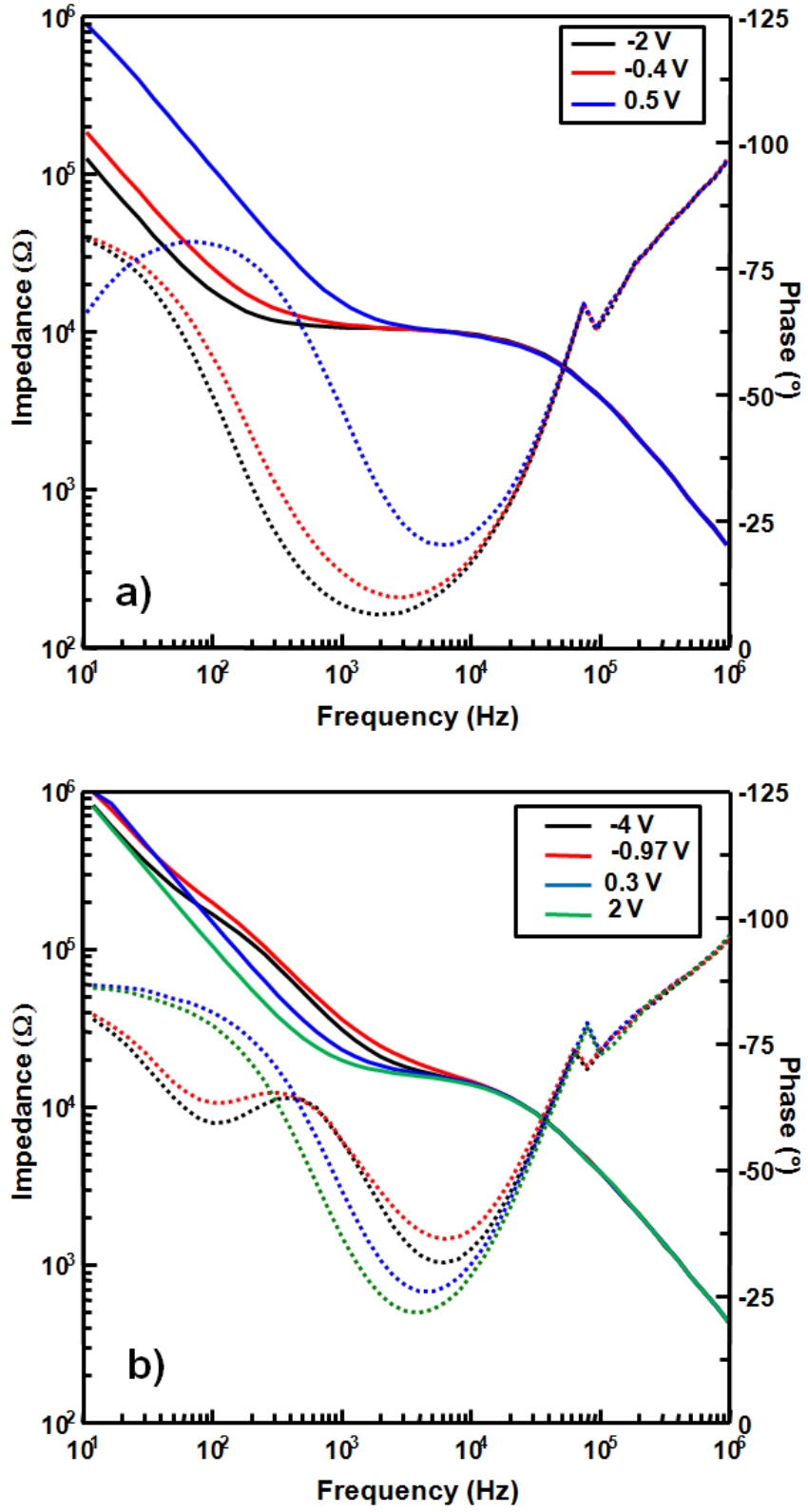

Fig. 4.12: Impedance-spectroscopy curves of an EIS (a) and an EISOI (b) sensor at different applied voltages.

As an example, Figure 4.12a shows the impedance spectra of an EIS sensor recorded at polarization voltages of -2, -0.4 and 0.5 V. The impedance spectra of an EISOI structure recorded at applied gate voltages of -4, -0.97, 0.3 and 2 V are presented in Figure. 4.12b.

For both structures, a linear behavior is observed at frequencies above 40 kHz which bends over to a plateau of constant impedance at lower frequencies (<10-15 kHz). Such behavior of the impedance curve can be due to the existence of a series resistance. The impedance value in the plateau range is about 22 and 11 kΩ for the EISOI and EIS structure, respectively, verifying the higher series resistance of the EISOI structure discussed in section 4.3.1.

The stronger deformation of the *C-V* plots in the accumulation region by the series resistance in the frequency range of 100 Hz - 3 kHz makes the impedance of the EISOI structure in the accumulation region (at V_G = -4 V) higher than in the inversion region (at V_G = 2 V). However, at very low frequencies (<30 Hz), the impedance of the EISOI structure in the accumulation range becomes equal to the impedance in the inversion range, which can be attributed to the low-frequency *C-V* behavior of the structure. These observations are in good agreement with the measured *C-V* curves of the EISOI structures [AbMor11].

4.3.2.1 Simulation of the electrical equivalent circuit

The equivalent circuit model introduced for the EIS and EISOI structures (Fig. 4.8) in composed of several discrete elements. As mentioned in section 4.3.1, the equivalent circuit can be simplified as demonstrated in Figure 4.10. The simplified model consists of several elements. The values of the "passive" elements in the circuit are almost constant and they do not depend on the applied voltage or frequency. In contrast, the values of the "active" elements varied with the change of applied voltage or frequency. In general, the values of the passive electrical elements included in the equivalent circuits can be calculated by knowing their geometry. The defined value of the passive elements can be used in a fitting program (as fixed value) to find out the values of the "active" elements, which cannot be easily calculated or measured. The passive elements for the EIS and EISOI structures have been defined as follow:

R_{RE}: The value of R_{RE} in the model includes also the electrolyte resistance. The resistance of the electrolyte is about 100 Ω, which is defined by the salt concentration of the electrolyte used for the measurements that is negligible in comparison to the value of the reference electrode resistance. The resistance of the reference electrode is about 11 kΩ for both EIS and EISOI structures.

R_c: Using the Al-Si specific-contact resistance of (R_{sp}~700-800 Ωcm^2) and the Si-Al contact area for the EIS (1 cm^2) and EISOI (0.2 cm^2) structures, R_c (R_{sp} /A) has been calculated, namely ~0.7 kΩ and ~4 kΩ for the EIS and EISOI structures, respectively.

C_{ox}: As shown in section 2.1, the theoretically calculated C_{ox} is about 75 nF and 22 nF for

the EIS and EISOI structures, respectively.

The values of the "active" electrical elements, which depend on the applied voltage and Si properties, was estimated using the "Zview" program in the fitting mode. The "active" elements in the EIS and EISOI structures are as follow:

R_{sc}: R_{sc} is the resistance of the space-charge region. In the equivalent circuit for strong accumulation as well as in the depletion condition, it can be neglected, because $\omega.C_{sc}>>1/R_{sc}$. For this reason, it is not included in the equivalent circuit [Nico82, Sze81].

R_{si}: The value of the Si bulk-resistance depends on the resistivity of the Si substrate and the geometry of the structure. The series resistance R_{si} (bulk resistance) represented by the high-resistivity substrate consists of a resistance due to the volume directly under the area of the upper electrode of the capacitor, which can be estimated as $R_{si} \sim \rho.\frac{L}{A}$, where ρ is the resistivity of the substrate, L its thickness and A the area of the capacitor [Est96, Nico82]. Therefore, in the case of EISOI structures, the lateral R_{si} is bigger than that of EIS sensors as explained in section 4.3.1 (see Fig. 4.10).

C_{sc}: The value of the space-charge capacitance especially in the depletion region extremely depends on the value and polarity of the applied voltage. As it is an "active" element in the structure, it was given free for the fitting program.

Using defined fixed values for the passive elements in the equivalent circuit and fitting program, the values of the "active" elements, namely R_{si} and C_{sc} have been suggested using the "Zview" software in the fitting mode. The values of the equivalent circuits parameters of IS characteristics of the EIS and EISOI structures in the depletion region are summarized in Table 4.1. The measured and the simulated/fitted Bode diagram of the EIS and EISOI structures using the presented equivalent circuit (Fig. 4.10) in the depletion region at different frequencies (from 10 Hz to 1 MHz) are demonstrated in Fig. 4.13a and 4.13b, respectively.

Tab. 4.1: Values of the equivalent-circuit parameters used for the simulation/fitting of IS characteristics of an EIS sensor (at -0.4 V) and EISOI sensor (at 0.3 V) in depletion area.

	$R_{RE} + R_e (k\Omega)$	$R_c (k\Omega)$	$R_{Si} (k\Omega)$	$C_{sc} (nF)$	$C_i (nF)$
EIS	11	0.7	0.5	150	75
EISOI	11	4	5	17	22

The results in Table 4.1 show a higher bulk resistance for the EISOI structure (5 kΩ) in comparison to that of the EIS structure (0.5 kΩ), which has been expected and explained by the higher resistivity of the Si substrate and the geometry of the EISOI structures, previously. The validity of the results obtained by fitting program was proven as follow: The values of C_{sc}, which are obtained from the fitting program for the space-charge capacitance at -0.4 V (for EIS sensor) and at 0.3V (for EISOI sensor) was used to calculate the total capacitance (C) of the structures at these specific applied voltages (C is the series combination of C_{sc} and C_i). The calculated total capacitance for the EIS and EISOI structures are C (-0.4 V)= 50 nF and C (0.3 V)=9.5 nF, respectively. The experimentally measured total capacitance of the EIS (at -0.4 V) and EISOI (at 0.3 V) structures can be read out from the C-V curves (see Fig. 4.9), namely ~40 nF for the EIS and ~10 nF for the EISOI sensor.

The results from fitting data are in good agreement with that of the experimentally measured C values at the above mentioned applied bias voltages (see Fig 4.9a and Fig. 4.9b). It confirms the validity of the developed equivalent circuit for the EISOI structure and the predictions about the effect of the "active" elements of the structure on its C-V and impedance spectroscopy characteristics.

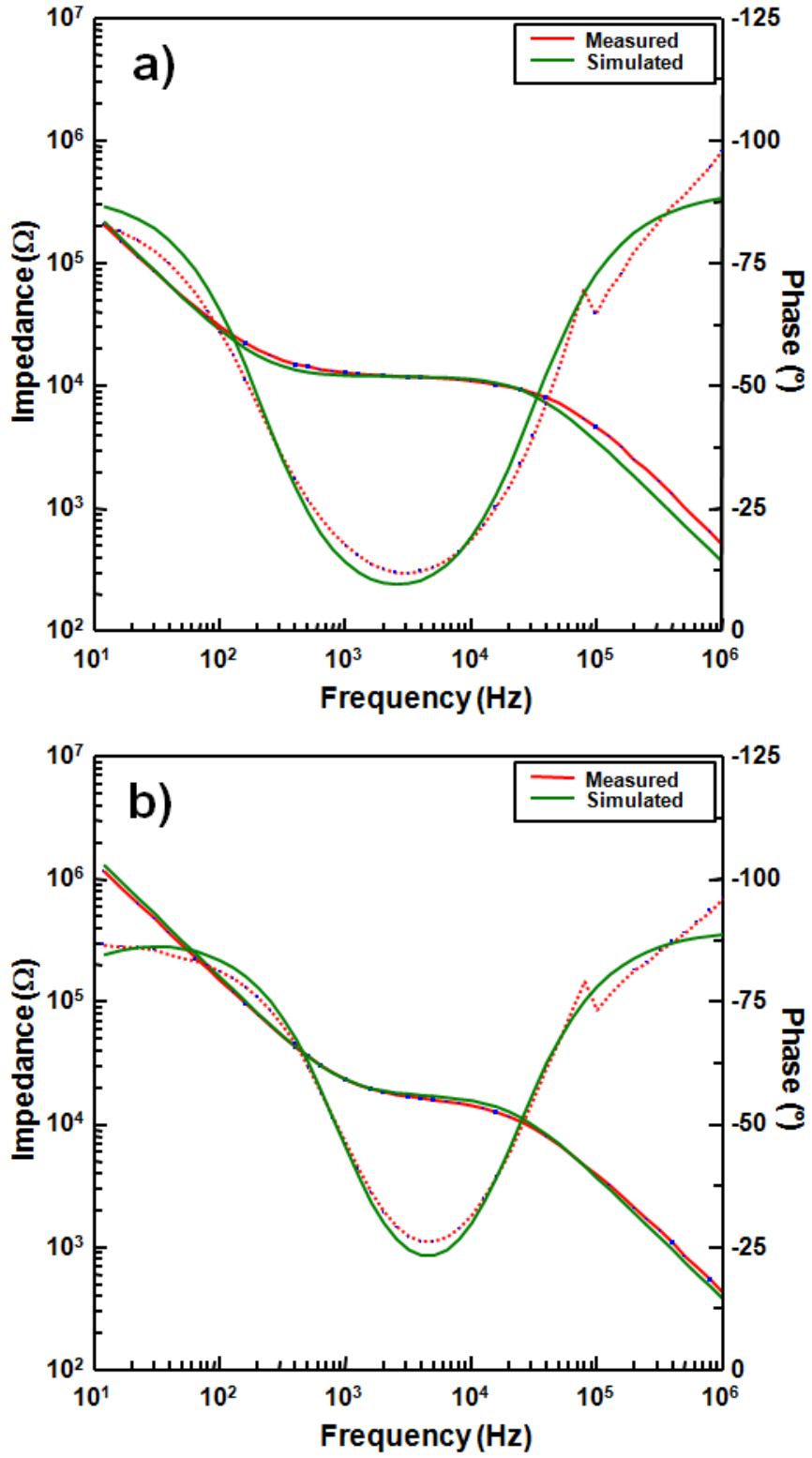

Fig. 4.13: Measured and simulated Bode diagram of an EIS sensor (-0.4 V) (a) and an EISOI structure (0.3 V) at depletion region.

4.3.3 pH sensitivity

In this work, bare EIS and EISOI sensors with a SiO_2 gate insulator were used for pH control (see also Fig. 4.14), realization of an enzyme-based penicillin sensor and as a reference sensor for DNA hybridization/denaturation detection in the differential mode setup.

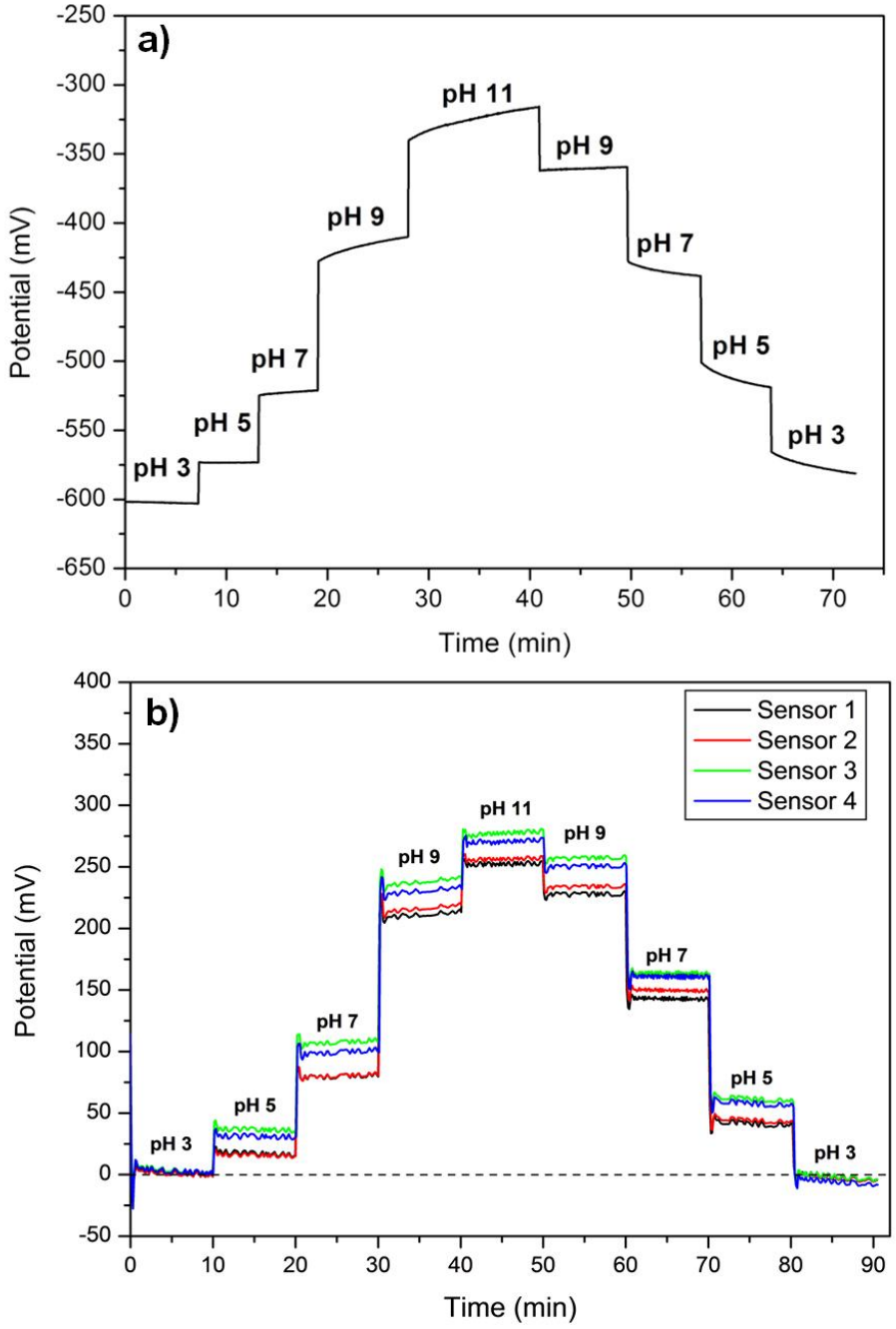

Fig. 4.14: Typical ConCap responses for an EIS sensor (a) and a 4-channel EISOI sensor array (b) measured in buffer solutions with different pH values from pH 3 to pH 11.

To determine the pH sensitivity of the sensors, about 1.2 ml working buffer (Titrisol buffer) was applied to the gate surface of the sensors and the output signals of the EIS sensors and EISOI sensor array (four sensors in an array simultaneously) were recorded.

As an example, Figure 4.14 depicts the typical dynamic ConCap response for an EIS sensor (a) and a 4-channel EISOI sensor array (b) in buffer solutions with different pH values from pH 3 to pH 11. The bare EIS sensor and all four sensors in the array show a nearly identical ConCap behavior with an average pH sensitivity of ~37 mV/pH, which is in good agreement with pH-sensitivity values for SiO_2 layers reported in literature (34-40 mV/pH) [Hal96, Hal95, BergSib88; PogSchg06]. The mechanism of the pH sensitivity of oxide surfaces is usually explained using the site-binding model [Yate74], which has been explained in chapter 2.3.2. According to this model, the presence of hydroxyl groups at the oxide surface results in pH-dependent changes of the surface charge, thus, modulating the space-charge capacitance of the EIS and EISOI sensors, respectively.

In the following part of this work, the physically and electrochemically characterized EIS and EISOI structures are used for the detection of PEM formation and DNA hybridization/denaturation, respectively.

Chapter 5

5 Detection of PEM build-up using capacitive EIS sensors

This chapter mainly deals with the detection of formation of PEMs (as a model system for planar-like molecular layers) on capacitive EIS sensors. The first section is a theoretical study of the change of the sensor's surface potential via PEM formation. It includes the effect of distance between the charged molecular layer and sensor surface as well as the ionic strength of the surrounding electrolyte on the sensor's surface potential. All simulations in this chapter are calculated and plotted using "Origin" software (version 8).

In the experimental part, the formation of PEMs ($(PAH\text{-}PSS)_n$) on the surface of EIS sensors was systematically investigated using physical and electrochemical characterization methods. Thickness, surface morphology, roughness and hydrophilicity of the PE mono- and multilayers have been physically characterized by ellipsometry, SEM, AFM and water contact-angle (CA) methods, respectively. For electrochemical characterization of the PEMs build-up, *C*-*V*, ConCap and IS methods were applied. The effect of ion concentration of the solution, polyelectrolyte concentration, buffered/unbuffered solution, number and polarity of the PE layers on the characteristics of the functionalized EIS sensors with PEMs was studied. In addition, the pH and ion sensitivity of the sensors functionalized with mono- and multilayers of PE were investigated. Based on these experiments, the validity of a developed theoretical model is discussed. Finally, a new strategy for enhanced field-effect-based biosensing using PE layers was introduced. This chapter contains results that are partially published in scientific journals [AbPog09, AbPog10, PogAb06, PogAb07, PogAb08, PogIn07, SchgAb09].

5.1 Electrostatic model for PEM formation

Field-effect-based capacitive EIS sensors allow the determination of the change of the surface potential and surface charge at the insulator/electrolyte interface (see Eq. 2.4 and Eq. 2.5). As polyelectrolytes are polyions which are charged in aqueous solutions, their adsorption, deposition or binding on the sensor surface changes the sensor's surface potential that results in the modulation of the capacitance of the structure. The total capacitance of the EIS structure, modified with a PE layer, $C(\psi_{s-PE})$, can be expressed as:

$$C(\psi_{s-PE}) = \frac{C_{eff} C_{sc}(\psi_{s-PE})}{C_{eff} + C_{sc}(\psi_{s-PE})} \tag{5.1}$$

with

$$\frac{1}{C_{eff}} = \frac{1}{C_i} + \frac{1}{C_{PE}} \tag{5.2}$$

where C_{eff} is the effective gate capacitance of the EIS structure modified with a PE layer, CPE is the capacitance of the PE layer that adsorbed on the insulator surface, and ψ_{s-PE} is the potential at the electrolyte/gate interface after the PE adsorption (see Fig. 5.1). If $C_{PE} >> C_i$ (because of very thin PE layer or larger PE dielectric constant in comparison to that of the SiO_2 layer), the capacitance of the PE layer can be neglected in the circuit, which results to $C_{eff} = C_i$.

The capacitance change of the whole structure via adsorption of the PE layer modulates the *C-V* curve and the output signal of the EIS sensor. Generally, the flat-band voltage of an EIS system is given by Eq. 2.5. In this equation, all terms can be considered as constant expect for sensor's surface potential, which is a function of pH, ion or analyte concentration as well as charge of adsorbed molecules. As a first approach for the EIS device covered with PE layer, the shift of the flat-band voltage (ΔV_{fb}) can be considered as a change of the potential at the gate/electrolyte and/or gate/PEM interface:

$$\Delta V_{fb} \cong f(\psi_s - \psi_{s-PE}) \cong f(-\psi_{PE}) \tag{5.3}$$

where, ψ_s, ψ_{s-PE} and ψ_{PE} are the gate/electrolyte, gate/polyelectrolyte and polyelectrolyte/electrolyte interface potentials, respectively.

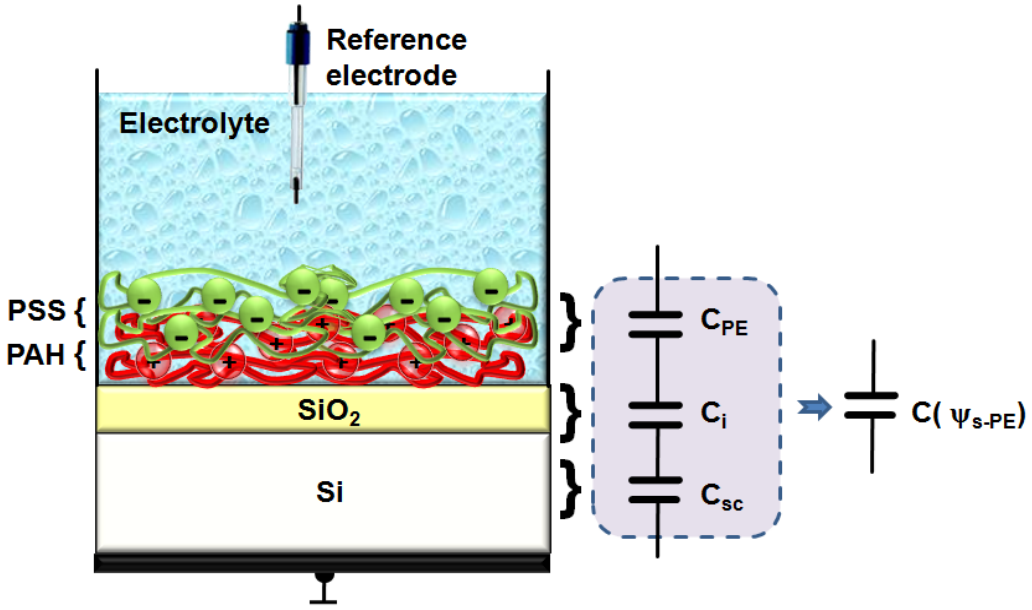

Fig. 5.1: Schematic of an EIS sensor functionalized with PE layers and simplified electrical equivalent circuit.

Beyond this, the output signal of the EIS sensor (ΔV_{fb}) is a function of ψ_{PE}. Using the simplified Grahame equation (Eq. 2.10), the surface potential of a PE layer with a defined charge density (σ_{PE}), can be calculated as follow:

$$\psi_{PE} = \frac{\sigma_{PE}\lambda_D}{\varepsilon\varepsilon_0} \tag{5.4}$$

The electrostatic surface potential of the charged layer is proportional to the charge density of the molecular layer (σ_{PE}) and the Debye screening length of the surrounding electrolyte (λ_D).

Figure 5.2 shows the calculated relationship between ψ_{PE} and PE layers surface charge (with different surface charge densities, from 10^{15} to 10^{20} charged groups/m^2) for different concentrations of monovalent salt (10^{-4}-1 M), using (Eq. 5.4). Decreasing the salt concentration in

the electrolyte leads to increasing of the Debye length (decreasing of the screening effect of counter ions in solution on the surface charge) and a higher surface potential.

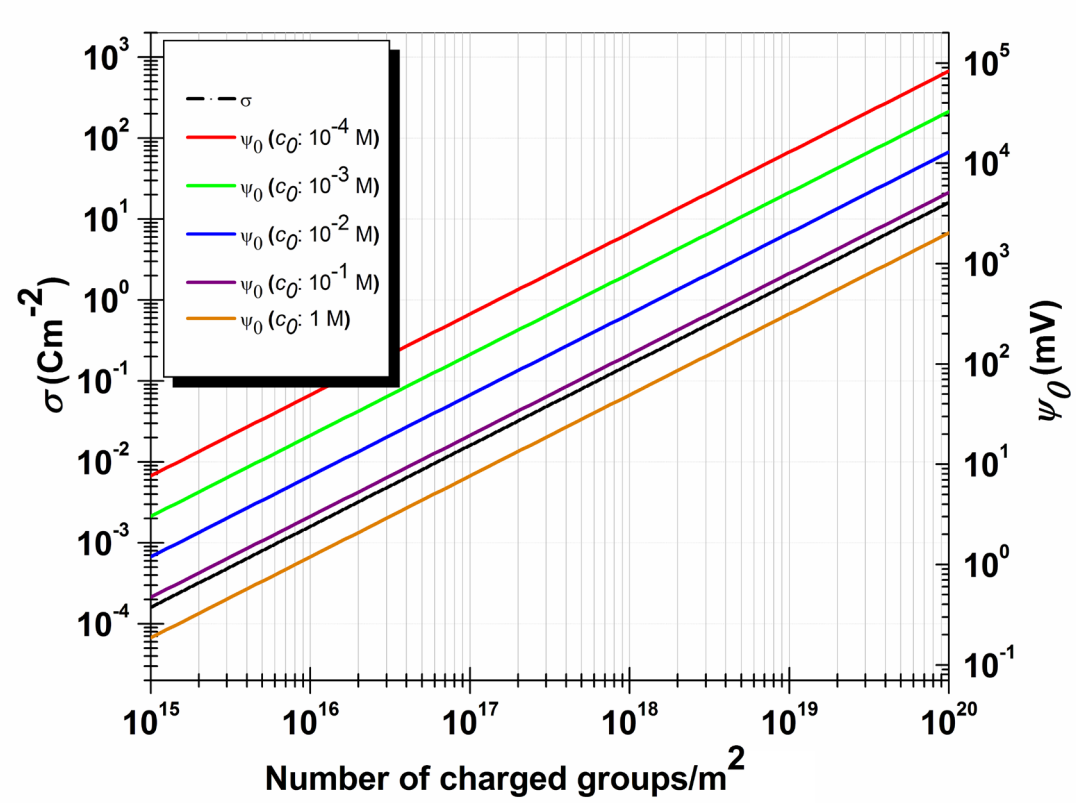

Fig. 5.2: Surface-charge density and surface potential of a PE layer as a function of number of charged groups per surface area in electrolyte solutions with different monovalent salt concentration (using Eq. 5.4 and "Origin" software). c_0: Concentration in electrolyte.

Via LbL build-up of PEM (planar-like formation) on the surface of an EIS structure, the distance between the terminated PE layer and sensor surface increases, which influences the sensor response. The potential distribution of a PE layer ($\psi_{PE}(x)$) with a distance x from the sensor surface can be calculated using the "linearized Poisson-Boltzmann equation" for planar surfaces:

$$\psi_{PE}(x) = \psi_{PE}.e^{-kx} \tag{5.5}$$

The potential decreases exponentially. The decay length is given by x and $k = 1/\lambda_D$ (see section 2.3.1). Figure 5.3 demonstrates the plotted potential distribution as a function of distance in electrolytes with different ion concentrations (10^{-1}-10^{-3} M) for a charged surface with a charge density of 3×10^{17} ionized groups/m^2 (using Eq. 5.5).

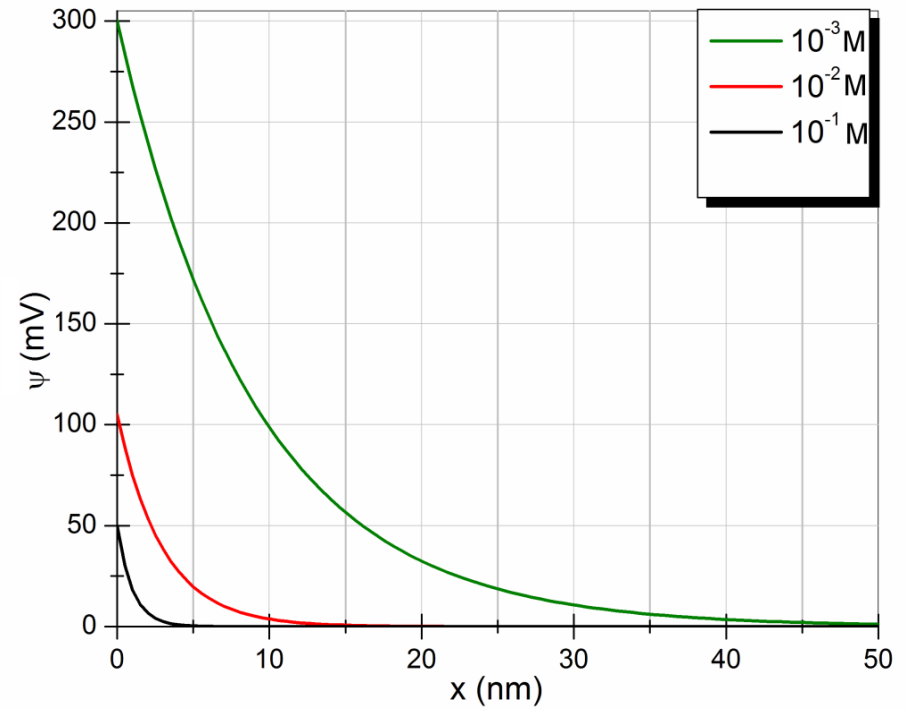

Fig. 5.3: Potential versus distance for a surface with a charge density of 3×10^{17} ionized group/m^2 in solutions with different ionic strength (using Eq. 5.5 and "Origin" software).

A model of the functionalized SiO_2 surface with multilayers of positively and negatively charged polyelectrolytes and system parameters is demonstrated in Figure 5.4.

This model introduces three regions:

- PEM/electrolyte interface (region 1);
- PEM (region 2);
- SiO_2/PEM interface (region 3).

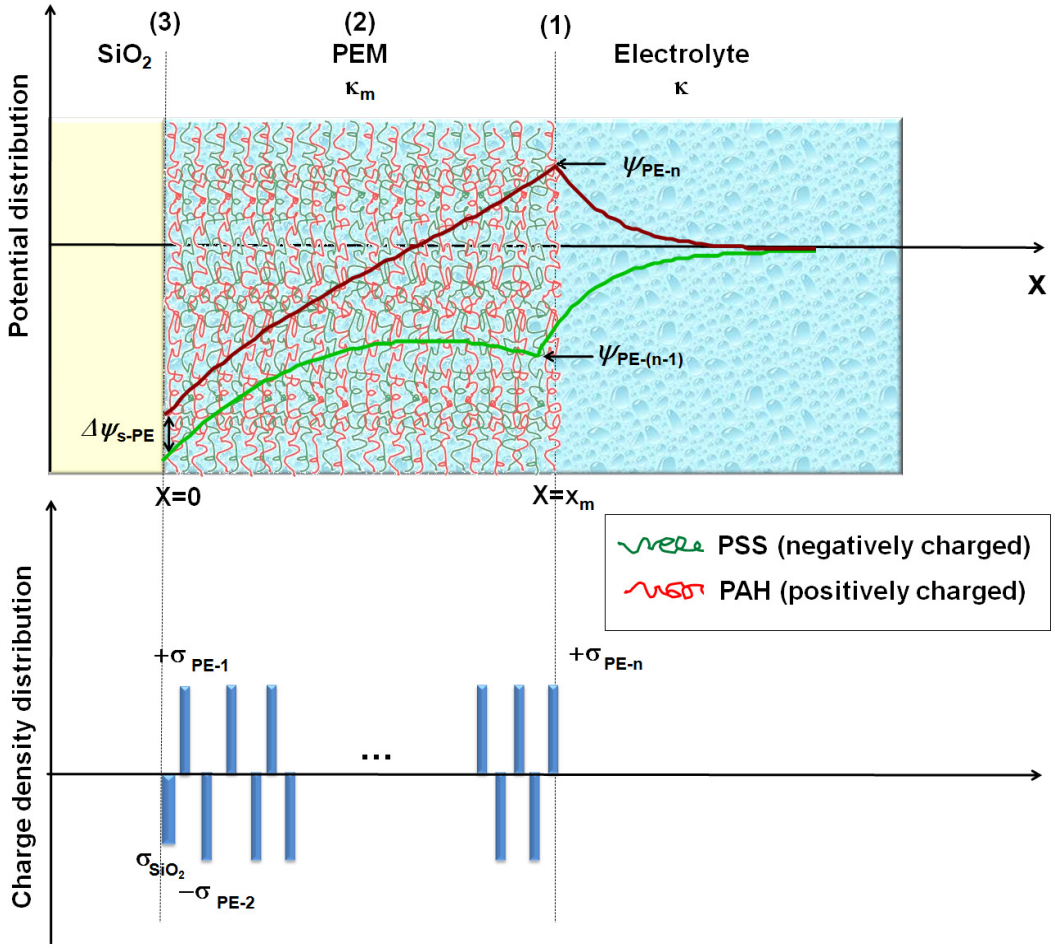

Fig. 5.4: Definition of the model parameters and sketch of a typical potential distribution in the Si/SiO_2/PE/electrolyte system for the negatively and positively charged outermost PE layer. For the screening lengths inside the PEM that are comparable to the PEM thickness, the variation of electrostatic potential from the terminating PE layer and from the sensor surface overlap inside the PEM structure as shown in the figure. On the contrary, for screening lengths $1/k_m$ that are much shorter than the PEM thickness x_m, the potential variations inside the PEM take place only close to $x = 0$ and $x = x_m$ boundaries and there exists a bulk of PEM structure, where the potential is nearly zero.

The potential at the PEM/electrolyte interface after adsorption of the nth layer of polyelectrolyte (ψ_{PE-n}) can be calculated, using Equation 5.4, by a given σ_{PE-n} and the concentration of electrolyte. The effect of potential change at PEM/electrolyte interface should be reflected via the PEM on SiO_2/PEM interface, to be detected by the EIS sensor.

In this model, the PEM interior is considered as a fully charge-compensated electrolyte medium of thickness $x_m \sim n_{PE}$ (number of adsorbed layers) $\times\, d_{PE}$ (thickness of each layer) containing some concentration of mobile ions. The screening effects inside the PEMs originate both from small mobile ions trapped inside the multilayer structure and from partially mobile

charges on the adsorbed PE chains. The concentration of the mobile ions in the PEM (c_m) is 100 to 1000 times lower than the concentration in the electrolyte (c_0) [NefWu07b, Schf03a].

The variation of the sensor's surface potential ($\Delta\psi_{s-PE}$) upon consecutive adsorption of positively and negatively charged PE layers in consideration of ionic strength of the electrolyte as well as distance of adsorbed layer to the sensor surface is predicted from the combination of Eq. 5.4 and Eq. 5.5, respectively, as follows:

$$\Delta\psi_{s-PE} \cong \psi_{PE-n}(x) = \psi_{PE-n}.e^{-k_m x_m} \rightarrow \Delta\psi_{s-PE} \cong \frac{\sigma_{PE-n}}{k\varepsilon\varepsilon_0}.e^{-k_m.n_{PE}.d_{PE}} \tag{5.6}$$

where, $1/k_m$ represents the screening length in the PEM (due to the ion concentration in the PEM).

Simulations of potential oscillation on the sensor surface ($\Delta\psi_{s-PE}$) upon adsorption of PE layers from solution with different ionic strength as a function of layer number and layer thickness (using Eq. 5.6) are presented in Fig. 5.5a and Fig. 5.5b, respectively. The potential on the sensor surface becomes more positive upon PAH adsorption and it turns more negative when the outermost adsorbed layer is PSS. The influence of the charge of the terminating PE layer thus "propagates" towards the sensor surface. It was obtained that for longer Debye lengths in the electrolyte solution the potential amplitudes $\Delta\psi_{s-PE}$ are larger and the potential value reaching the sensor surface decays slower with the number of PE layers adsorbed n_{PE}.

It should be noticed here that in contrast to zeta-potential measurements of PEMs, where the potential at the PE/electrolyte interface is determined, FED devices detect the potential changes at the PEM/gate-insulator interface. The latter strongly depends not only on the amount of surface charges of the terminating PE layer but also on the charge distribution and screening effects within the PEM. This might be the reason why electro-kinetic studies on PEMs' zeta-potential measurements [ScSchf02] showed almost no change in the amplitude of the detected alternating potential over a large range of deposited PE layers.

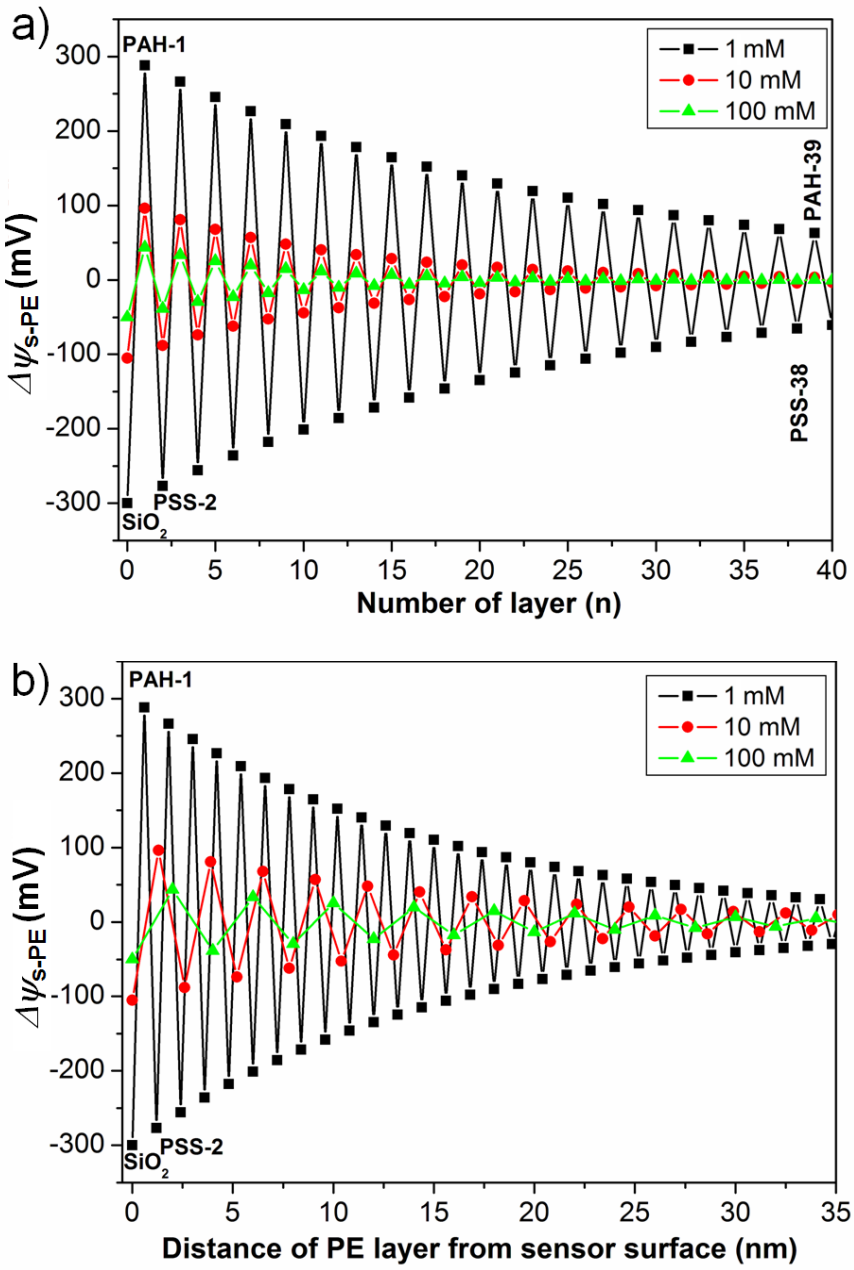

Fig. 5.5: Simulated potential variations on the sensor surface with a charge density of 3×10^{17} ionized groups/m^2 (using Eq. 5.6) upon repetitive adsorption of positively and negatively charged PE layers (a) and distance from the surface (b).

5.2 Physical and electrochemical characterization of PEM build-up

5.2.1 LbL deposition of PEM on EIS sensors

For the PEM deposition, the surface of the capacitive EIS sensors was first cleaned in a 5% Hellmanex (Hellma, Germany) solution for 5 min followed by rinsing with distilled water and

drying with nitrogen. Then, the surface of the sensors was cleaned and activated by treatment in oxygen plasma (45 s, 100 W). The build-up of PEMs on the sensor surface was achieved using the LbL technique by consecutive adsorption of PAH and PSS (with molecular weight of Mw~ 70,000, Sigma Aldrich). In order to find out the role of the PE-solution composition on the PEMs formation and the sensor-output signal, the PEMs were deposited on the sensor surface from unbuffered PE solutions with different PE (10 µM and 50 µM PAH or PSS) and salt (1 mM, 10 mM, and 100 mM NaCl) concentrations as well as in a 1 mM phosphate buffer solution, containing 100 mM NaCl. During the experiments, the EIS sensors were consecutively exposed to the respective PE solution for a time necessary for the adsorption of a single monolayer (usually 3-5 min), followed by rinsing with a solution of the same salt concentration and pH value as the respective PE solution or with ultrapure water before exposing to the next PE solution without any drying steps (for electrochemical characterization) or with drying steps (for physical characterizations). These procedures were repeated until the desired number of layers was achieved. The pH value of all solutions used was adjusted to pH 5.4. Here, the surface of SiO_2 is negatively charged, thus the PEM formation was started with positively charged PAH. The pH value and conductivity of PE solutions were controlled with a Mettler-Toledo MPC227 pH/Conductivity Meter.

5.2.2 Determination of multilayer thickness, morphology and hydrophilicity

As a basis for future study of PEM build-up detection using EIS sensors, it is necessary to physically characterize the system that gives information about the step-by-step change of the thickness and morphology of the molecular film after adsorption of each PE layer. To investigate the effect of PE concentration, ionic strength of the solution and the number of PE layers on the thickness of the PE layers, the PEMs with up to thirteen bilayers of (PAH-PSS) were prepared from a 10 and 50 µM PAH or PSS solutions with different salt concentration. After the adsorption of each PE layer, the samples were rinsed with water and dried in a nitrogen stream. The thickness of the PEMs was controlled after each adsorption step by imaging ellipsometry (EP3, Nanofilm, Germany). The average thickness per monolayer deposited from 50 µM PE solutions with 100, 10, and 1 mM NaCl was 2±0.2, 1.3±0.1, and 0.6±0.1 nm, respectively. This tendency of the layer thickness decreasing with lowering the salt concentration is consistent with the results reported [Schf03b, Nef06], and can be explained by the fact that electrostatic forces responsible for the complexation of oppositely charged PEs and subsequent PEM formation are stronger in electrolyte solutions with a lower ionic strength (see section 3.1). The average thickness per monolayer prepared from 10 and 50 µM PE solutions

containing 100 mM NaCl was nearly the same of about 2 nm, indicating that there is no influence of PE concentration on the PEM thickness (at least in the range of PE concentration used in this study). Moreover, no influence of the number of layers on the thickness of each adsorbed layer has been observed and the thickness of the PEMs increased linearly with the adsorption of PE layers, which is in good agreement with reported results in literature [Schf03b, Nef06, Han06, Bos04].

In addition, AFM images were taken after the adsorption of each PE layer to gain a picture of how the morphology of PEMs evolves during the multilayer build-up. Tapping mode liquid-cell AFM images were obtained in 0.1 M NaCl, pH 5.4, using a Digital Instrument AFM with Nanoscope IV controller and multimode base (Veeco Instruments, USA). The scan size was 1 µm × 1 µm. The morphology and roughness of the PE mono- and multilayers were obtained from the height images. The surface roughness was quantified using the root-mean-square value, R_{ms}, and the surface-area difference. As an example, Figure 5.6 shows AFM images of a bare SiO_2 surface (a) and a SiO_2 surface with the adsorbed $(PAH\text{-}PSS)_5$-PAH multilayer (b), and height profiles along the lines indicated in the scan images (c) and (d). For a better comparison between the samples, the *z*-axis displaying the height was scaled to 20 nm. The average roughness of the bare SiO_2 estimated from the AFM-height images was approximately 0.2 nm. The roughness increased with the number of adsorbed PE layers and the value of R_{ms} = 6 nm was obtained after the adsorption of a $(PAH\text{-}PSS)_5$-PAH layer similar to reported results in literature [Bos04].

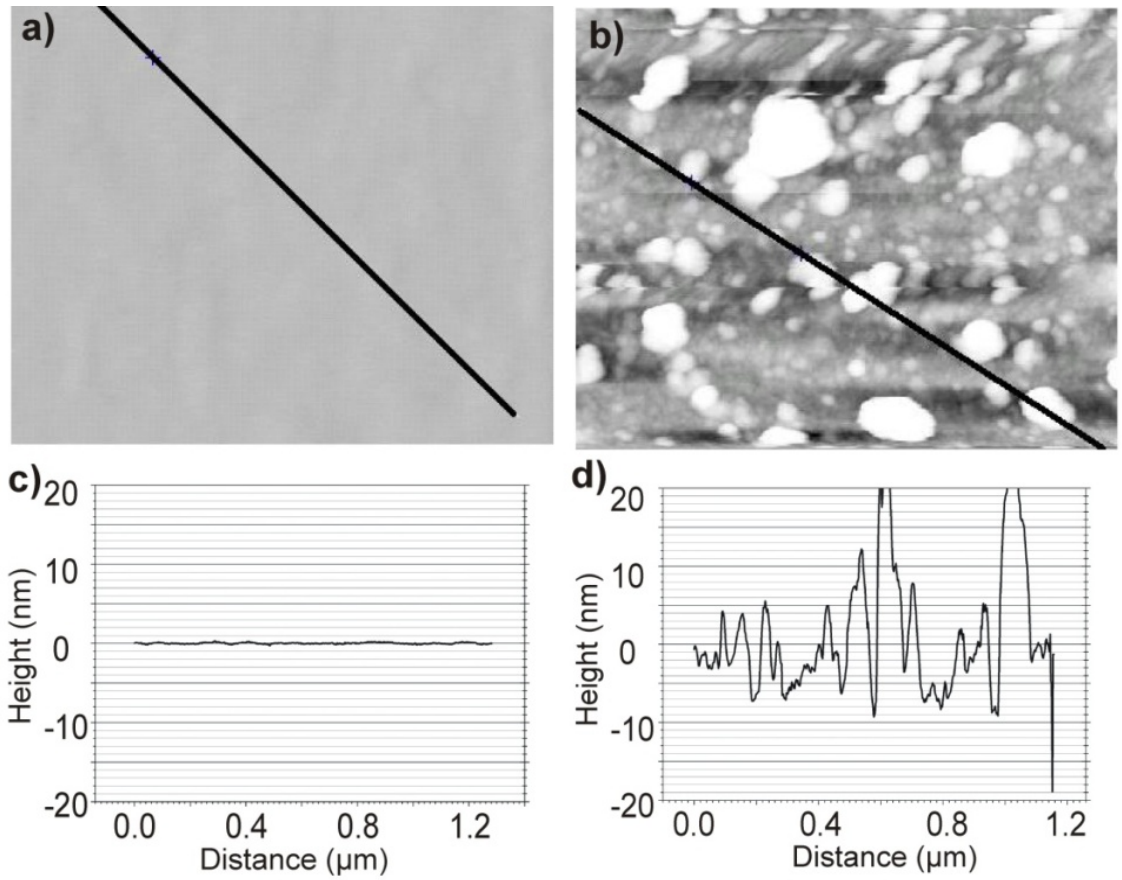

Fig. 5.6: Liquid-cell AFM images of a bare SiO_2 surface (a) and a SiO_2 surface with the adsorbed $(PAH\text{-}PSS)_5$-PAH layers. Scan size is 1 µm×1 µm. The figures (c) and (d) below the images are height profiles (section graphs) along the lines indicated in the scan image. For better comparison between the samples, the z-axis displaying the height was scaled to 20 nm for all images and height profiles. The greyscale of the images was applied as 20 nm corresponding to 256 grey values. [Frank Amberger's diploma thesis, FH Aachen, 2006].

Moreover, SEM images visualize the change of the sensor-surface morphology via the PEMs' formation. Fig. 5.7 demonstrates an SEM picture of the SiO_2 surface covered with one PAH layer (a) and eleven PE layers (b) deposited, from a PE solution of 50 µM PAH or PSS, containing 100 mM NaCl. These figures illustrate that both the roughness and morphology of the sensor surface change upon the PEM formation. A pretty irregular surface of PEMs emerges after deposition of eleven PE layers. Progressive build-up of PEM thickness roughness is likely due to a stronger coiling of the PE chains adsorbed for higher numbers of deposited PE layers.

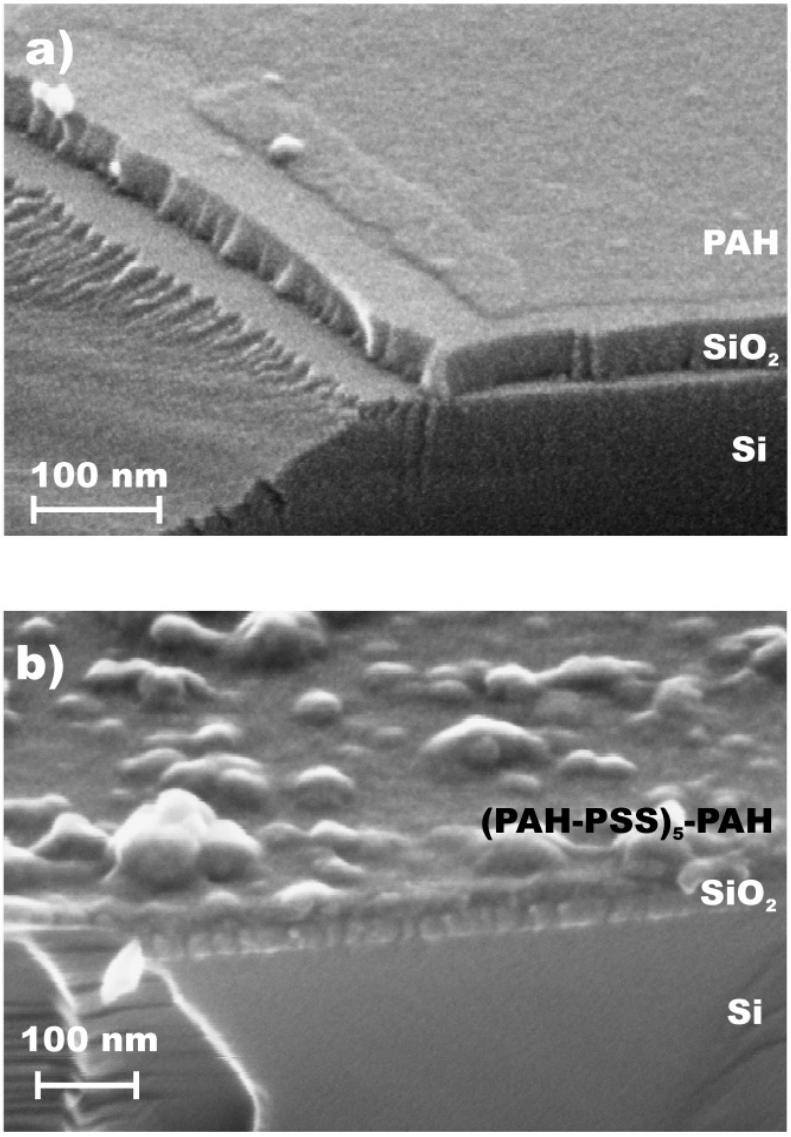

Fig. 5.7: SEM picture of the p-Si/SiO_2 (30 nm) structure functionalized with one PAH layer (a) and multilayer of $(PAH\text{-}PSS)_5$-PAH prepared in 100 mM of NaCl and 50 µM of PE solution (b).

Furthermore, the hydrophilicity of the sensor surface as prepared and after deposition of mono- and multilayers of PE has been studied by water contact-angle measurements. Figure 5.8 depicts results of the water droplet (5 µL) contact-angle measurements on PEM films with different number of PAH/PSS bi-layers prepared from PE solutions with 1 and 100 mM NaCl. After the adsorption of each PE layer, the sensor surface was rinsed in water and dried for 5 minutes in nitrogen atmosphere. For a freshly cleaned SiO_2 surface, the measured contact angle was nearly 0°. The adsorption of a first PAH layer increases the contact angle up to 45-55°, whereas by adsorption of a second layer (PSS) the contact angle decreases down to 38-45°. Moreover, the contact angle measured on the PEM surface with negatively charged PSS as outermost layer was always lower than that with previous positively charged PAH

layer as outermost layer. This shows the influence of the outermost PE layer on the wetability of the surface and it is in good agreement with results reported in literature [YoSh98].

A drastic decrease of the contact angle with increasing the layer number has been observed. This study is in contrast to results reported in [YoSh98], where the samples have been dried in 90 °C for 1 h and stored in room temperature for 1 day before contact-angle measurements. The decreasing could be explained by the presence of water molecules in the prepared PEMs in this work.

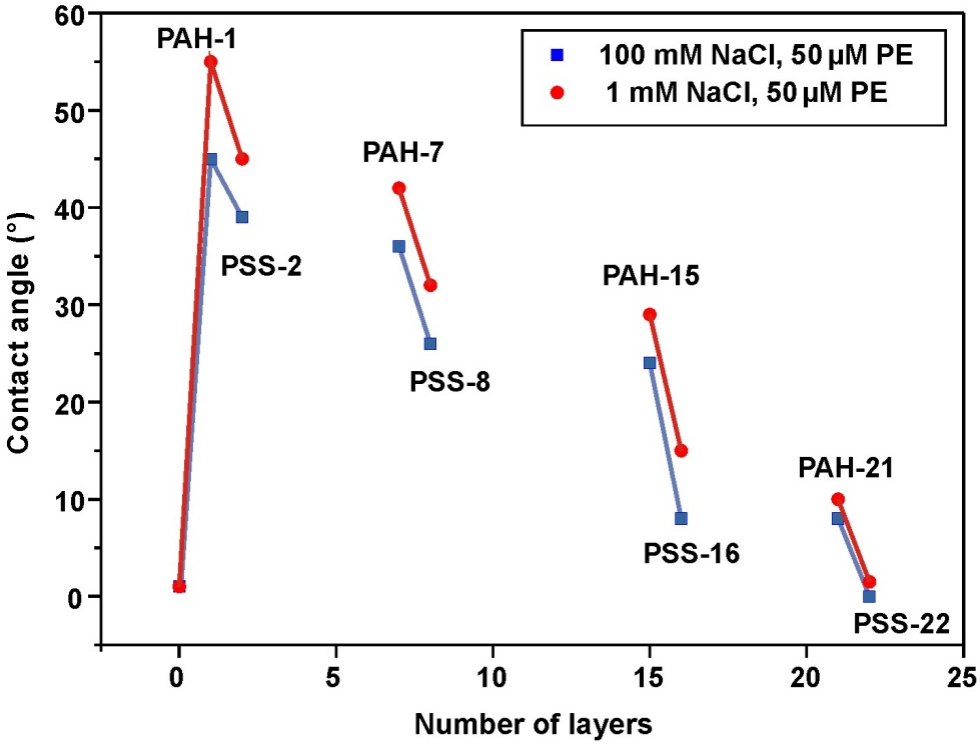

Fig. 5.8: Water contact angle vs. layer number of the PEM prepared from PE solution with different NaCl concentrations.

The water contact angles of PEMs prepared in a 100 mM NaCl solution were slightly but systematically smaller than those prepared in a 1 mM NaCl solution. This could be attributed to the changes in morphology and the increase in the surface roughness of PEMs prepared in solutions with a higher ionic strength.

In this part of the Ph.D. thesis, physical characterization methods have been used to gain information about the PEM build-up on EIS sensors and the parameters, which can influence the PEM characteristics (e.g., thickness and porosity, morphology). In the next section, the PEM formation was studied by means of field-effect EIS sensor using *C-V*, IS and ConCap

methods. The results will show the possibility of using such sensors as an alternative cost-effective tool for the full characterization of the PEMs' build-up.

5.2.3 Electrical monitoring of PEM build-up

For dynamic monitoring of PE adsorption on the sensor surface and in order to find out the time necessary for the adsorption of each layer, the measurements were done in the ConCap mode (Fig. 5.9). Here, the capacitance of the EIS sensor is kept constant with the use of a feedback-control circuit that allows a direct dynamic recording of potential changes during the PE adsorption and PEM build-up (see section 4.2). The bare EIS sensor was first equilibrated in electrolyte solution. After obtaining a stable sensor signal, the certain amount of high-concentrated PAH solution (pH 5.4) was injected to the electrolyte (100 mM NaCl) to adjust the PE concentration in the electrolyte to 50 μM. The sensor response decreased immediately (~52 mV), which can be attributed to the change of the sensor surface-charge due to PAH adsorption on the sensor surface. The sensor response was recorded (~20 min) till no change in the potential was observed (no more adsorption), then the measurement was interrupted and the sensor surface was washed with electrolyte to remove not completely adsorbed PAH from its surface. The same procedure was repeated for adsorption of PSS on the PAH layer. The results showed that 98% of the signal change due to the adsorption of each PE layer took place in the first 3 min and was very fast. The results clearly demonstrate the felicitous use of EIS sensors for PEM-formation detection. Nevertheless, the results of this experiment are not enough to answer the questions about the exact mechanism of signal generation and possible system parameters that influence the EIS-output signal. Therefore, the subject of the next section is the study of the EIS sensor response as a function of adsorbed PE layers.

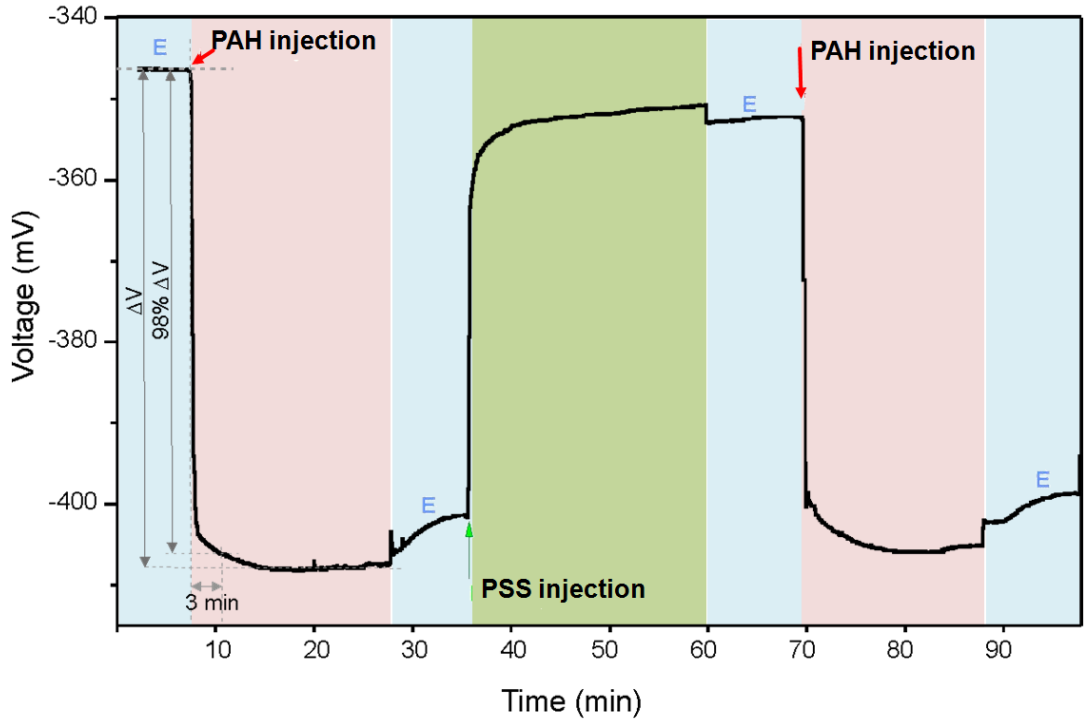

Fig. 5.9: ConCap response of the EIS sensor upon PAH and PSS adsorption measured at 100 Hz. E: electrolyte solution.

5.2.3.1 Effect of PE-layer number on sensor response

EIS sensors covered with mono- and multilayers of PAH/PSS have been characterized by means of *C-V*, ConCap and IS methods using an impedance analyzer (see section 4.2).

The *C-V* curves for a p-type EIS structure as prepared and after the adsorption of each positively charged PAH and negatively charged PSS layer from the PE solution of 50 µM PAH or PSS, 100 mM NaCl are shown in Figure 5.10a. Similar to the bare EIS structure and depending on the magnitude and polarity of the applied V_G, three regions in the *C-V* curve, namely accumulation, depletion and inversion, can be distinguished. As can be seen, the existence of an additional PE layer shifts the *C-V* curves of the original EIS structure along both the capacitance and voltage axis. The changes in the maximum (or geometrical) capacitance in the accumulation range of the *C-V* curve were very small only amounting to about 1.5-2 nF (<2.5-3%). Taking into account Eq. 5.2, this indicates that C_{PE} is much higher than C_i.

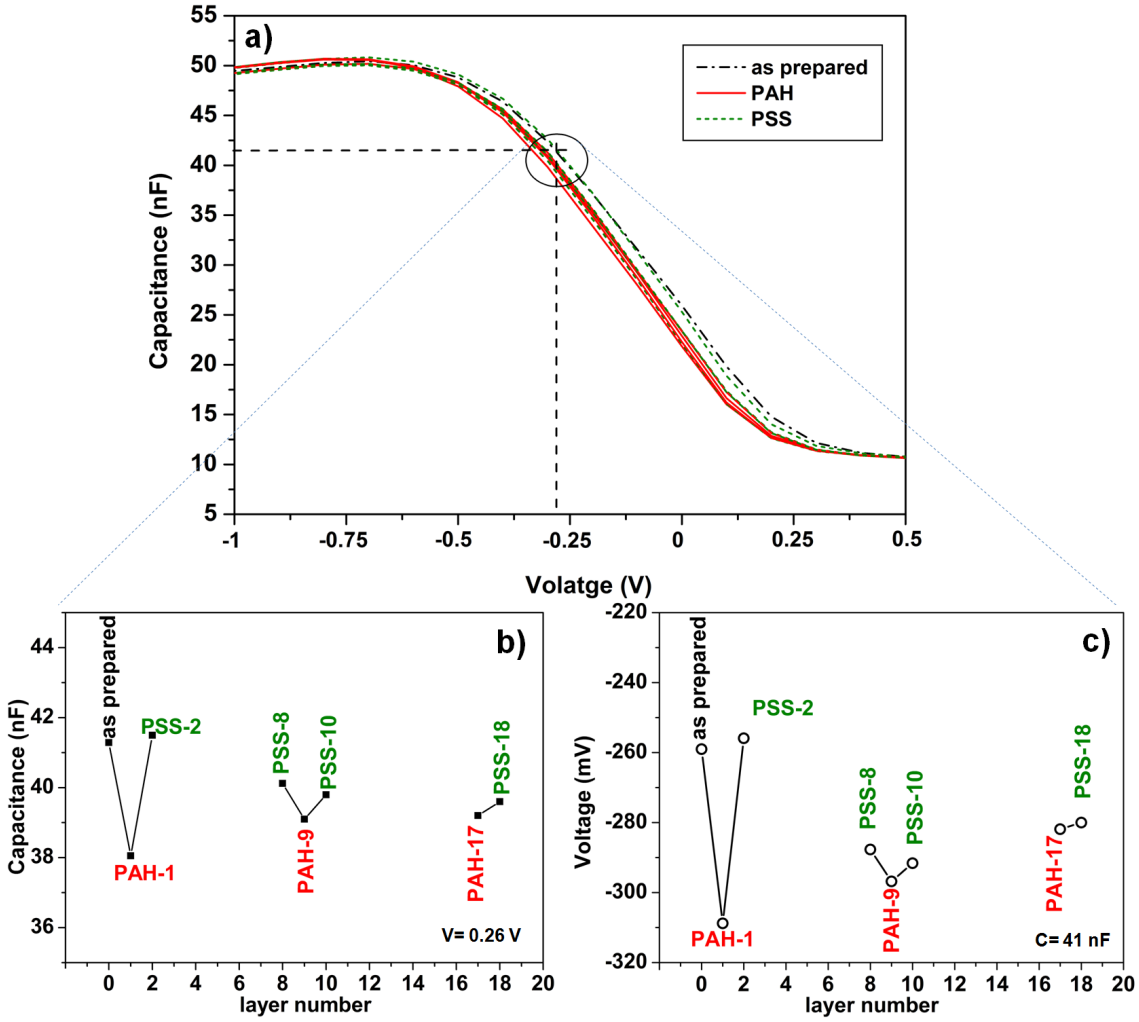

Fig. 5.10: *C-V* curves for a capacitive p-Si/SiO_2 EIS sensor as prepared and after adsorption of each polyelectrolyte layer (a) and zoomed graphs of the capacitance (b) and potential (c) changes in the depletion region as a function of the PE-layer number. The maximum number of adsorbed PE layers was 18.

If the adsorbed layers are considered as a homogeneous dielectric film of defined thickness and dielectric constant, changes in the geometrical capacitance due to the additional 18 PE layers should be much higher, which was not the case in this experiment. This is probably due to the incompletely dense as well as porous structure of the adsorbed PE multilayer containing a large amount of water molecules and small ions.

For sensor applications, the most interesting part of the *C-V* curve represents the depletion region. In contrast to the accumulation range, the capacitance changes as well as shifts in the *C-V* curves along the voltage axis in the depletion region (~60% of the C_{max}) have alternating character (see Figs. 5.10(b) and (c)). Incidentally, the direction of these shifts depends on the sign of the charge of the outermost or terminating PE layer. This indicates that the molecular layer may also induce an interfacial potential change resulting in a change in the flat-band

voltage of the EIS structure. Moreover, it was observed that both the capacitance and the potential shifts have the tendency to decrease with increasing the number of PE layers [Abpog09, PogAb06, PogAb07, PogIn07, PogAb08]. For example, potential shifts decrease from 50-53 mV for an EIS structure with one to two PE layers to 10-6 mV and 2-3 mV for an EIS structure with 8 to 10 and 17 to 18 PE layers, respectively. Figure 5.10 shows a distinct decrease of the capacitance and potential shifts with increasing the number of layers deposited. A similar effect has been observed for field-effect thin-film resistors [NefNa06, NefWu06] and EIS sensors with nanocrystalline diamond as sensitive-gate material [AbPog09, AbPog08a] functionalized with PE multilayers.

Beside the *C-V* method, impedance spectroscopy is a useful tool for electrochemical characterization of modified/functionalized EIS sensors (see e.g., [PogAb08, Abd06, KraMor06, Bar05, Ben06, PogMa04, Hou06]). Figure 5.11(a) shows Bode plots in the accumulation and depletion regime for an EIS structure as prepared and functionalized with PE mono- and multilayers. Similar to the *C-V* curves, IS plots in the depletion region have an alternative character. This can be clearly recognized from the zoomed Figure 5.11(b), where the impedance values at a frequency of 100 Hz (100 Hz are chosen to compare the results with *C-V* measurements in Figure 5.10) are depicted as a function of the layer number. In contrast to the accumulation region, where practically no changes in the impedance of a functionalized EIS structure have been observed, the impedance in the depletion region depends on both the layer number (with a tendency to decrease with increasing the number of PE layers) and the sign of the charge of the terminating PE layer, which is a consequence of the change in the depletion capacitance.

In further experiments, the adsorption of PE layers was monitored in electrolyte solution (after rinsing step) by means of dynamic ConCap measurements. In this experiment, the bare EIS sensor was first equilibrated in electrolyte solution. After obtaining a stable sensor signal, the measurement was interrupted and the PAH solution was applied to the sensor for 5 min. This was followed by rinsing the measuring cell and sensor surface with electrolyte solution, and ConCap measurements were performed in electrolyte (100 mM NaCl, pH 5.4) for about 3 min. In the next step, the PSS solution was applied to the sensor surface for 5 min, and after the cleaning step the ConCap response was recorded in electrolyte for about 3 min again. The same procedure was done for each adsorbed PE layer.

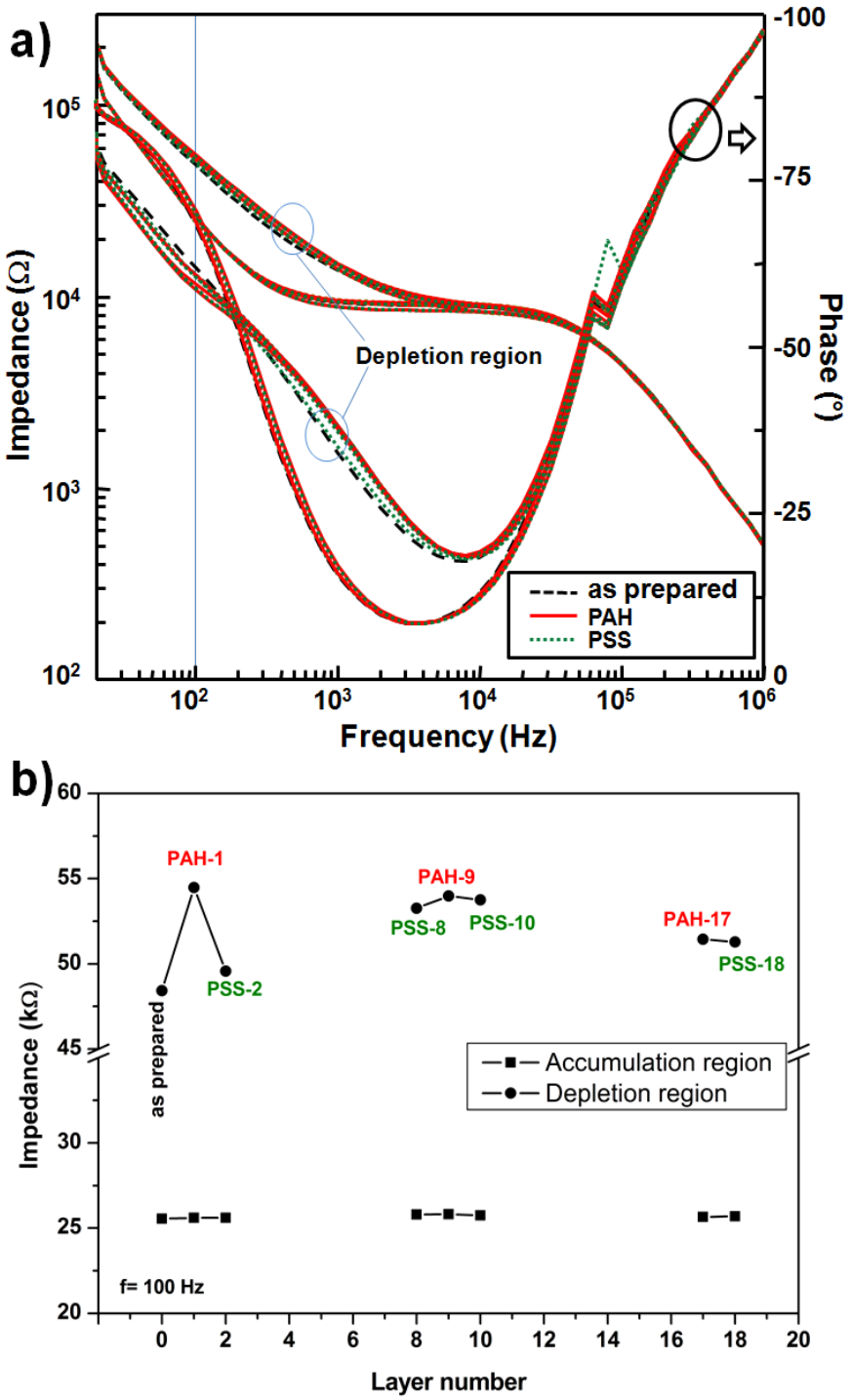

Fig. 5.11: Bode plots in accumulation and depletion regions for an EIS structure as prepared and functionalized with the PE mono- and multilayers (a) and impedance values in accumulation and depletion region at a frequency of 100 Hz as a function of the PE-layer number (b).

Figure 5.12 shows an example of ConCap response of the EIS sensor during the deposition of seven bi-layers from the PE solution of 50 µM PAH or PSS, 100 mM NaCl. The ConCap measurements also reveal alternating changes in the sensor signal upon adsorption of each polycationic and polyanionic layer, correlated with the charge sign of the terminating PE lay-

er. This shows a good agreement with results achieved by *C-V* measurements. The adsorption of the PAH shifts the sensor signal in the direction as if additional positive charges emerge on the SiO_2 surface. This corresponds to a more negative sensor signal in Figure 5.12 due to the feedback control in the ConCap mode. In contrast, the adsorption of PSS shifts the potential towards the direction corresponding to a more negatively charged gate surface. Such an alternating behavior of the ConCap response has been observed during all experiments on PEM build-up, independent of the PE and salt concentration or buffered/unbuffered solution.

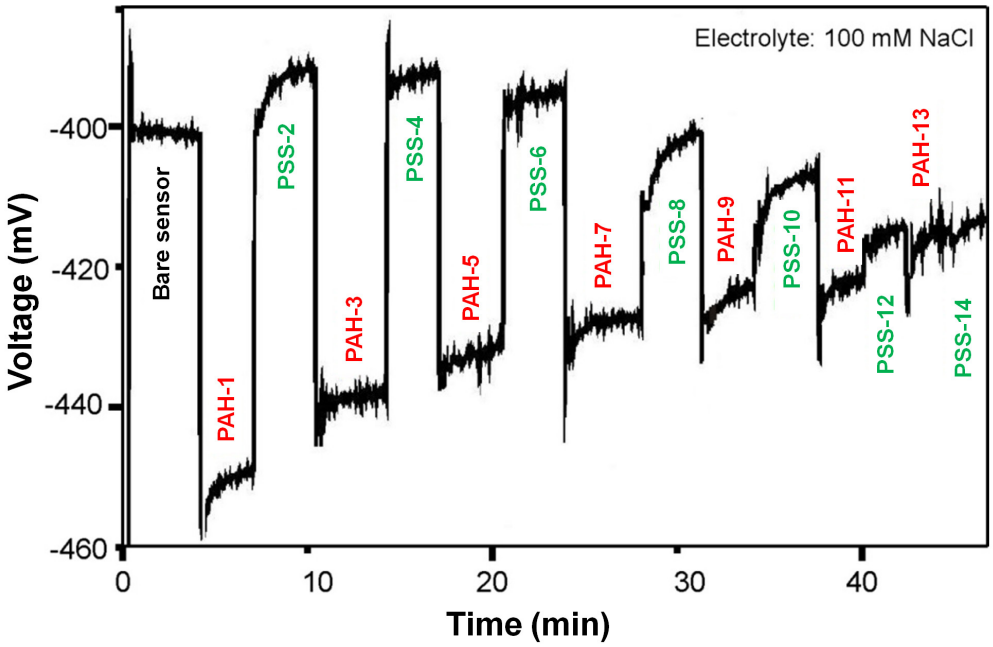

Fig. 5.12: ConCap response of the EIS sensor upon PAH and PSS adsorption measured at 100 Hz.

The results of the experiments demonstrated that the output signal of the EIS sensor via formation of PEMs is extremely affected by the number of PE layers. The output signal has the tendency to decrease by increasing the number of adsorbed layers and increasing the distance between the last layer and sensor surface. As all measurements using EIS structures for detection of charge macromolecules were performed in aqueous solutions containing ions, the screening and condensation of the molecular charge by counterions in solution is unavoidable. Therefore, the following section focuses on the study of the effect of ion concentration of the applied electrolyte on the EIS-output signal via the PEM formation.

5.2.3.2 Effect of electrolyte concentration on sensor response

In order to find out the role of ionic strength of PE solution on the sensor output signal, the PEM were deposited from a 50 µM PE solution with different NaCl (1 mM, 10 mM, and 100

mM) concentrations. Figure 5.13 summarizes the potential shifts as a function of the PE-layer number evaluated from *C-V* and ConCap curves of p-Si/SiO_2 sensors using electrolytes with different ion concentrations (for each concentration six sensors have been characterized).

Here, two important effects can be recognized:

- The amplitude of the potential shifts decreases with increasing salt concentration. This can be attributed to the stronger screening of the PE charge of the terminating layer as well as inside the PEM by mobile ions with increasing the ionic strength of the solution. As a result, the electrostatic effect of the charge of the terminating layer on the gate-surface potential and therefore, on the sensor-output signal, will be diminished.
- Up to the first several adsorbed bi-layers (dependent on the salt concentration), any distinct decrease of potential shifts with the number of layers deposited that is in agreement with previous results [PogAb07, PogIn07, PogAb06] was not observed. Thereafter, the potential shifts have a tendency to decrease with increasing the number of adsorbed PE layers, whereas the decay is stronger and started early at a high salt concentration. For example, for the PEM deposited from a 100 mM NaCl solution, potential shifts decrease from originally 53-50 mV for an EIS structure with 1-2 PE layers to 10-6 mV and 3-2 mV for an EIS structure with 8 to10 and 17 to18 layers, respectively.

Due to the limitation of molecular charge detection using FEDs by the Debye screening-length [Berg91] from the experimental results for the decay of the sensor signal upon PEM formation in Figure 5.13, the Debye lengths inside the PEMs ($\lambda_{D(m)}$) can be expected to be almost equal to the PEM thickness, where no more signal was detected as a result of the future adsorption of PE layers. For instance, for measurements in 100 mM NaCl solution (see Fig. 5.13), the Debye length was estimated to be ~26 nm (for 13 PE layers with a thickness of ~2 nm for each layer). Using the expression for the screening length as a function of the ionic strength inside the PEM (I_m) taken in Moles, $\lambda_{D(m)} = \frac{3\text{Å}}{\sqrt{I_m(M)}}$, and assuming that the dielectric permittivity in the PEM interior is the same as in aqueous solution, and is independent on the electrolyte concentration, the ionic strength inside the PEM was estimated to be ~0.14 mM in the case of a 100 mM bulk solution. The obtained value of ion concentration inside the PEM is then, about 1000 times less than that of the bulk-electrolyte solution. These extremely small ionic strengths inside the PEM are in agreement with several other experimental evidences demonstrating that mobile electrolyte ions are almost entirely excluded from the PEM interior [Kli95,Nef06].

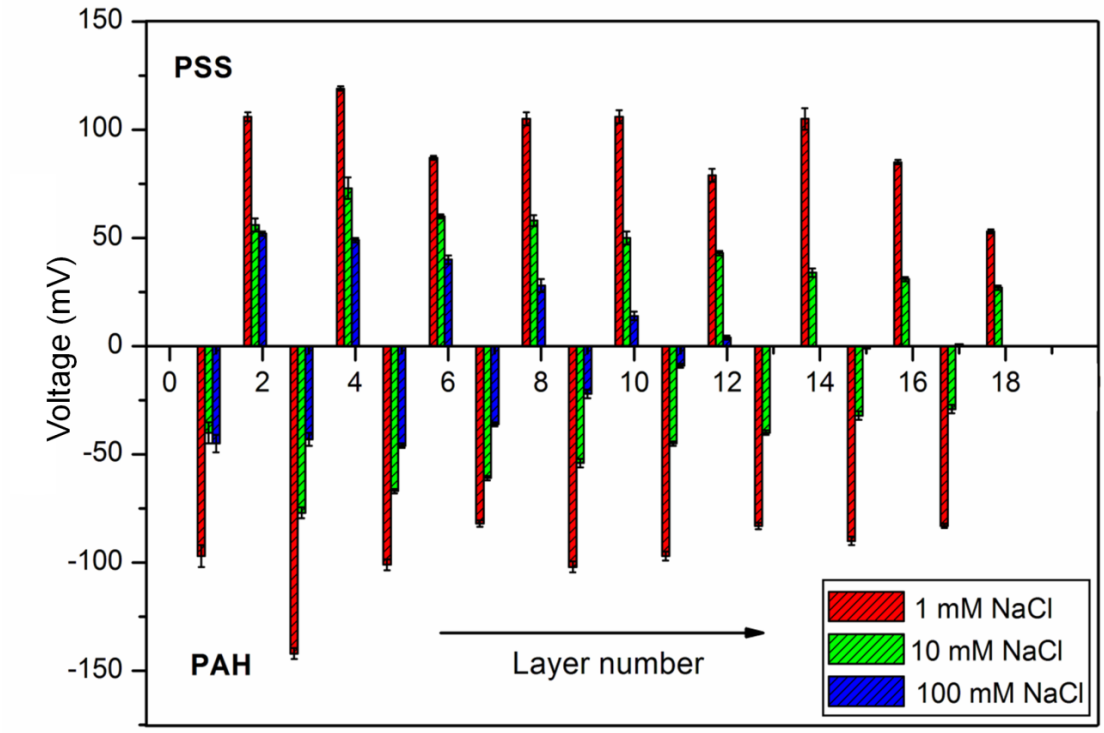

Fig. 5.13: EIS sensor-response shifts upon PEM formation evaluated from *C-V* and ConCap measurements in different NaCl concentrations (1 mM, 10 mM, and 100 mM) at pH 5.4 (six sensors in each group). The PE concentration is 50 µM for all measurements.

In addition to experimental observations, the potential-decay effect and its salt-concentration dependence was theoretically discussed in section 5.1 using the developed electrostatic model. This showed the decay of the sensor response connected to the different Debye lengths inside and outside of the PEMs as well the thickness of the PEMs prepared from the PE solutions with different salt concentrations (the higher the electrolyte concentration, the thicker the adsorbed PE layer).

To prove the validity of the introduced model in section 5.1, simulated and experimentally measured EIS sensor-output signals (V_{fb}) caused by the PEM build-up in electrolyte with ionic strength of 100 mM and 10 mM are demonstrated in Figures 5.14a and 5.14b, respectively.

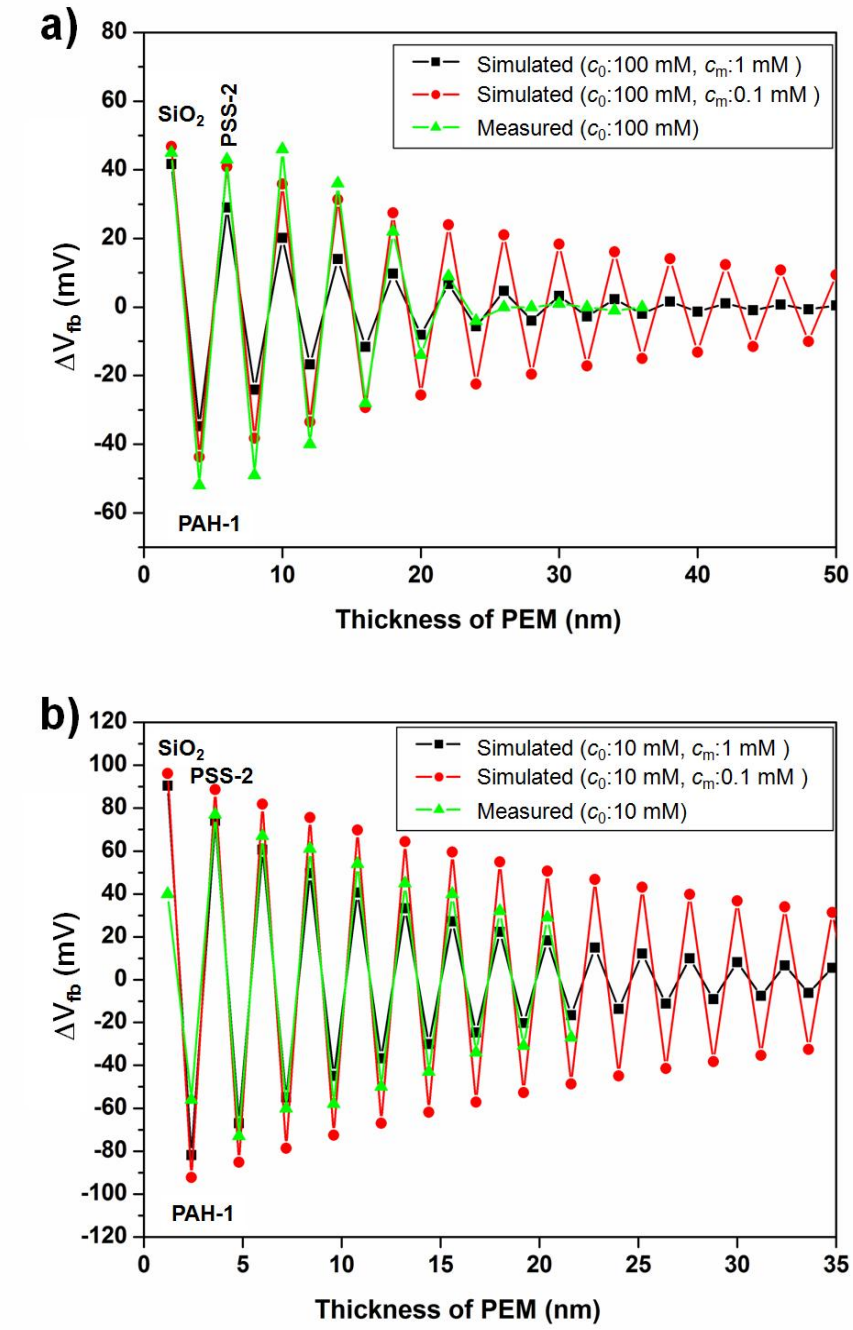

Fig. 5.14: Simulated and experimental EIS-sensor responses (~ΔV_{fb}) upon PEM build-up in electrolytes with ion concentration of (a) 100 mM and (b) 10 mM.

For the simulations (using Eq. 5.6), two different values for the ion concentration inside the PEM, namely 1 mM and 0.1 mM were used. The result of simulation for an ion concentration inside the PEM of 1 mM is in good agreement with the experimental data. The results show the feasibility of EIS sensors for studying the PEM properties.

5.2.3.3 Effect of polyelectrolyte concentration on a sensor response

To investigate the effect of PE concentration in solution on the sensor response (see Fig. 5.15), PEMs were prepared from PE solutions of 10 µM and 50 µM PAH or PSS, 100 mM NaCl.

The potential shifts evaluated from ConCap measurements after adsorption of each PE layer are shown in Figure 5.15. As can be seen, the PE concentration does not significantly affect the potential shifts suggesting a nearly identical amount of adsorbed PE on the gate oxide for both PE concentrations. This suggestion is supported by the fact that the average thickness per monolayer prepared from 10 and 50 µM PE solutions was nearly the same (about 2 nm).

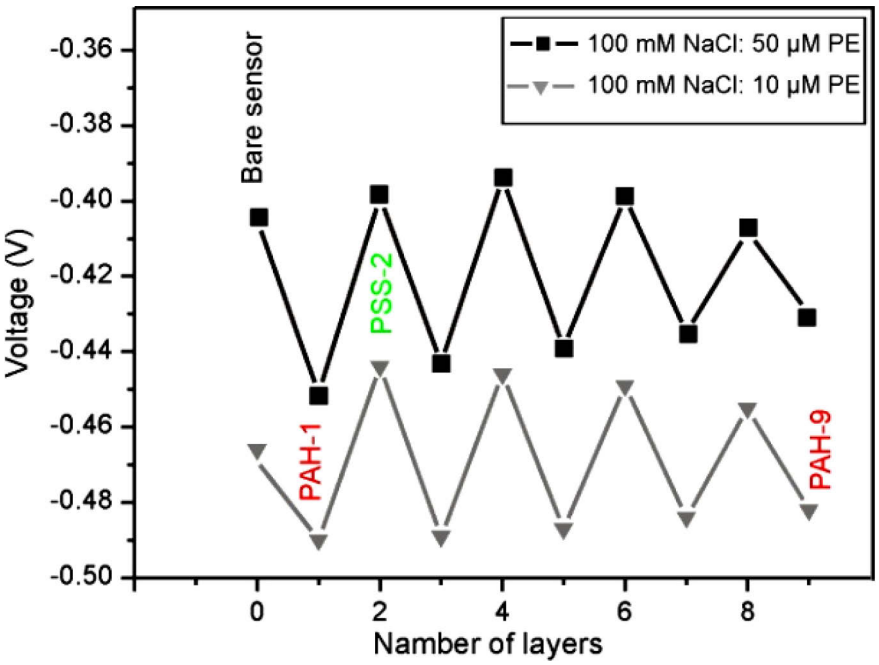

Fig. 5.15: Potential changes in the depletion region as a function of the PE-layer number evaluated from ConCap measurements in solutions with different PE concentration.

5.2.3.4 Effect of using buffered and unbuffered solutions on sensor response

The results obtained from the last sections demonstrate the feasibility of EIS structures for studying effects induced in field-effect sensors by the adsorption and binding of charged macromolecules. Since the EIS sensors with SiO_2 as gate material are pH-sensitive, this section is focusing on the study of the origin of the change in the flat-band voltage of the EIS structure via PEM formation and the reason for the induced effect in EIS sensors caused by the intrinsic

charge of adsorbed macromolecules and/or caused by the ion-concentration (including proton concentration) redistribution within the intermolecular spaces or in the multilayer.

Therefore, the measurements and PEM preparation using buffered (PE: 50 µM, NaCl 100 mM, PBS: 1 mM) as well as unbuffered (PE: 50 µM, NaCl 100 mM) solutions were applied. Figure 5.16a depicts the ConCap response of the EIS sensor upon adsorption of PAH and PSS layers prepared in 10 mM phosphate buffer solution of pH 5.4, with a background solution of 100 mM NaCl. It was observed that the potential shifts are much smaller for the PEMs prepared in pH-buffer solution and the potential oscillations decay much more rapidly with the number of adsorbed layers, as compared to PEMs formed from unbuffered solution (see Fig. 5.16b). With the buffer, the potential changes decay after 3-4 layers, while in unbuffered solutions the potential decay starts, after about 8-10 PE layers have been deposited. These measurements underline that PEM structures are permeable for protons that in turn influence quite dramatically the magnitude of the sensor response because the underlying SiO_2 layer is pH-sensitive.

The permeation of PEM structures to water molecules, small ions and protons has been reported in literature [Ham00, Schf07, Kli06]. Moreover, it was found that the pH profile and absolute pH values inside the PEM film drastically depend on the charge/potential at the interface between the outermost layer and electrolyte solution. In addition, the ionization degree of a weak PE such as PAH embedded in the layer was shown to oscillate with the net charge of the outermost PEM layer [Carr04]. Thus, it can be suggested that the local electric field emerged from the outermost PE layer redistributes protons (ions) in the PEMs, which in turn can change the local pH values on the SiO_2 surface and nearby the PAH layers. As result, the EIS sensor with a pH-sensitive gate material detects both molecular charge and the redistribution of protons and alternating pH profiles inside the PEMs upon PAH/PSS adsorption.

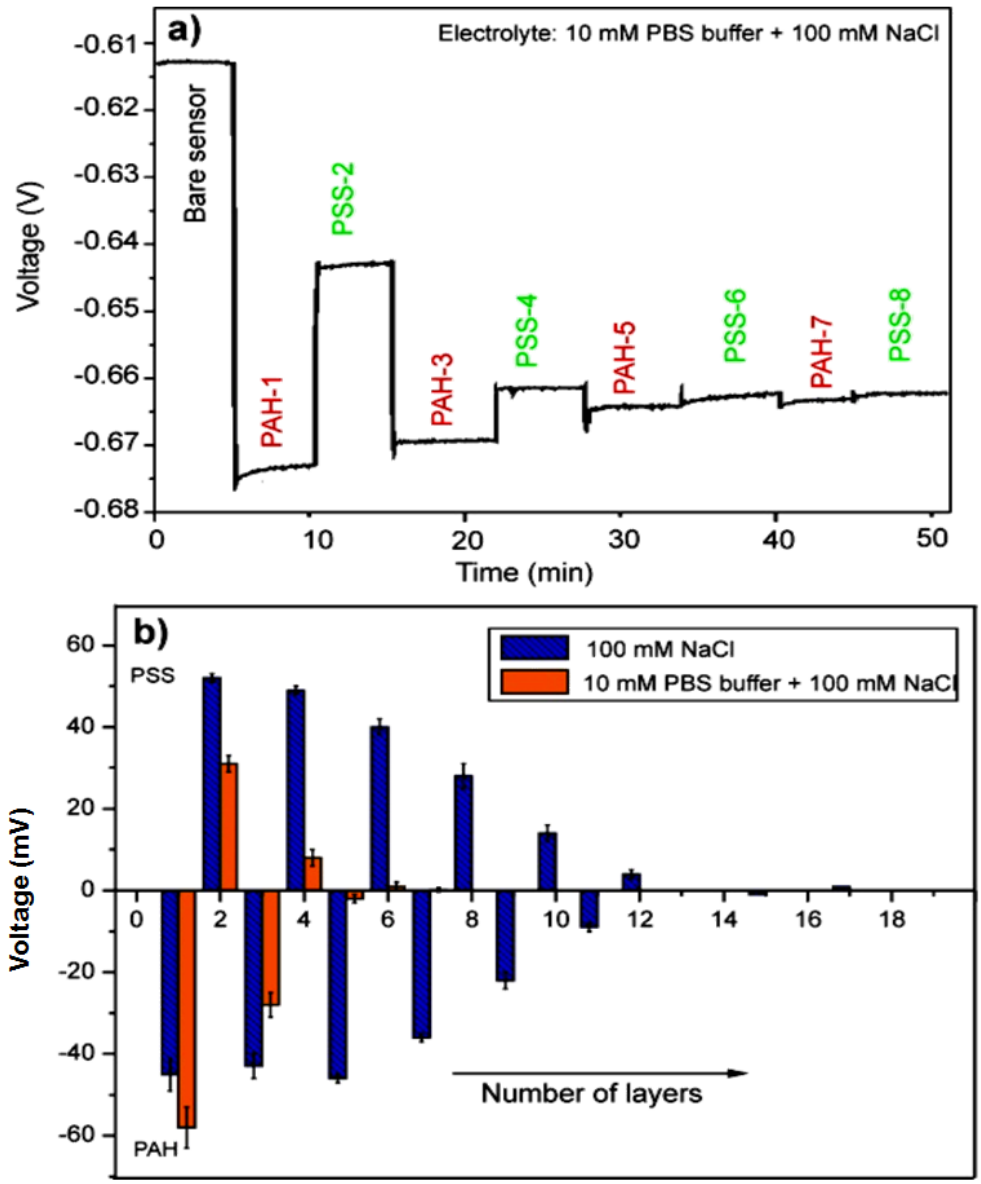

Fig. 5.16: ConCap response of the EIS sensor upon polyion adsorption measured in buffer solution (a) and the potential shifts evaluated from the *C-V* and ConCap curves for p-Si/SiO_2 sensors (3 sensors for each group) with PEMs in buffered and unbuffered solutions with 100 mM NaCl concentration at pH 5.4 (b). The PE concentration is 50 µM for all measurements.

5.2.3.5 pH and ion sensitivity of functionalized EIS sensors with PEM

In the present section, permeation of PEMs (with different layer numbers) to protons and sodium ions using EIS sensors (SiO_2 as gate insulator) was investigated. As an example, Figure 5.17 demonstrates the pH response of modified EIS structures with (a) fourteen (PSS-14) and (b) fifteen (PAH-15) PE layers.

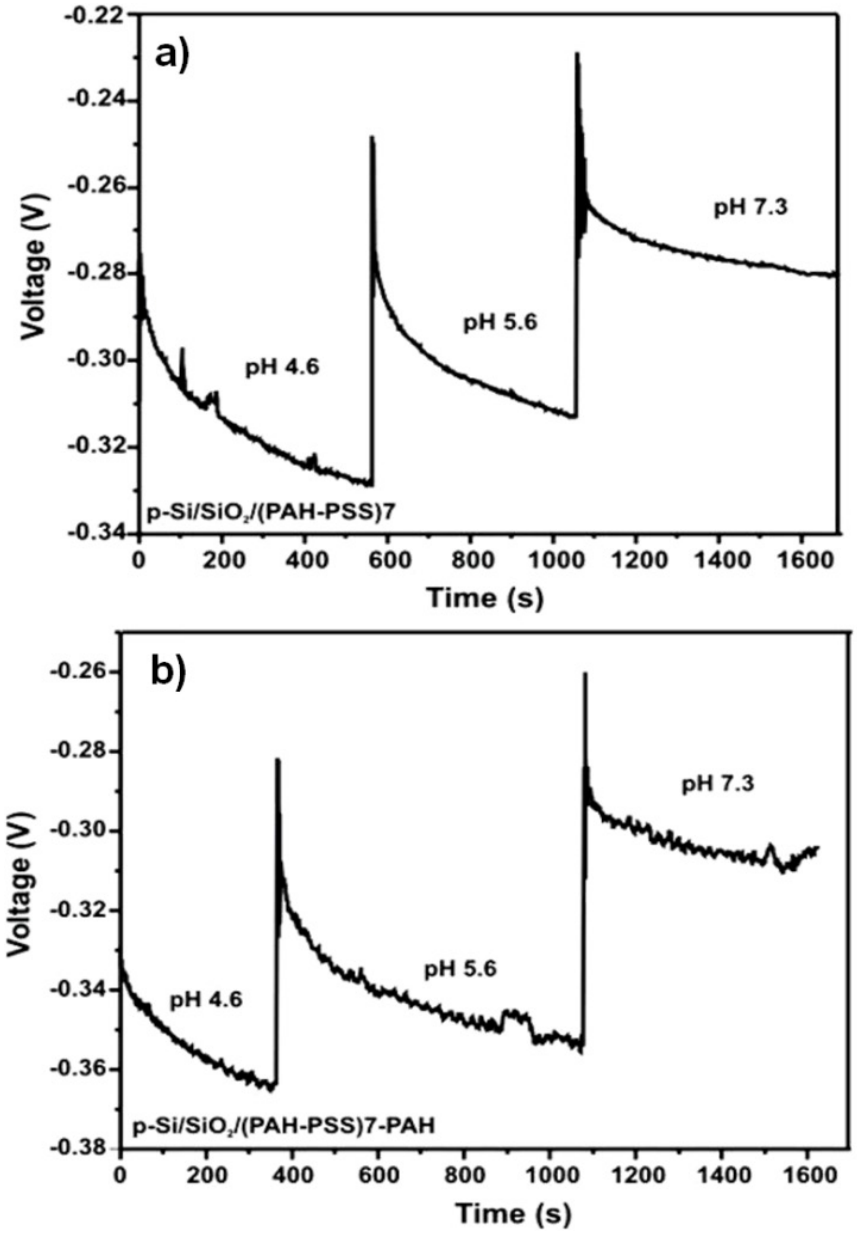

Fig. 5.17: pH sensitivity of post-deposited PEMs: ConCap response of EIS structure with the 14th PSS14 (a) and 15th PAH15 (b) layer as outermost layer. The measurements have been performed at a frequency of 1 kHz in 0.1 M NaCl solution with different pH values from 4.6 to 7.3.

The measurements were performed in 100 mM NaCl solution with different pH values between 4.6 and 7.3. The PE-modified EIS sensors show a clear dependence on the pH value of the solution. The average pH sensitivity of the sensor with the PSS-14 and PAH-15 layer as terminating layer was about 18 mV/pH and 21 mV/pH, respectively. A slightly higher pH sensitivity of about 20 and 25 mV/pH was observed for an EIS structure with a PSS-8 and PAH-11 terminating layer, respectively. Thus, the pH sensitivity slightly depends on the sign of the charge of the terminating layer (the difference between the pH sensitivity of the sensor with

PAH and PSS as terminating layer was about 3-5 mV/pH) as well as on the number of adsorbed PE layers.

These experiments confirm the high permeability of the PAH/PSS system for protons that is in good agreement with results for a PDADMAC (poly(diallyldimethylammoniumchlorid))/PSS system [Nef06]. On the other hand, the observed values of pH sensitivity were almost 1.5-2 times smaller than those of bare, unmodified SiO_2 layers. The possible reason for such a behavior could be the partial screening of surface active groups of the SiO_2 by the first adsorbed layers of PAH. This is inconsistent with results reported in [Nef06], where it was found that the pH sensitivity of a silicon thin-film resistor is not changed considerably by the adsorption of charged polymers. Note however, that in another experimental study, local pH variations across PAH/PSS PEMs have been measured using the changes in fluorescence intensity of pH-sensitive dyes, incorporated into the first adsorbed PAH layer [Kli95]. The dye intensity was shown to increase with the pH value of the buffer. Upon adsorption of a PSS layer, the increase in the dye intensity was detected that is indicative for larger pH values in the first PAH layer for PSS-terminated PEMs. Thus, the proton concentrations are smaller there, contrary to the expectation that negative potentials inside the PEMs due to the terminating PSS layer should accumulate more protons in such structures. It was argued that the influence of the Donnan equilibrium is relatively small for such PEM systems, in contradiction to recent results reported in [Schr07]. For the PEMs with terminating PAH layers, the dye fluorescent intensity in the first PAH layer was shown to correspondingly decrease as compared to PSS-terminated PEMs. These alternating changes in the pH close to the sensor surface upon the PEM formation are due to the permeability of the multilayer structure to protons. This permeability effect decreases with the number of adsorbed PE layers. Thus, the pH sensitivity slightly depends on the sign of charge of the terminating PE layer as well as on the number of adsorbed layers. This is another indication of the thickness-dependent permittivity of PEM structures to external pH-regulating protons [SchgAb09].

In addition to the pH-sensitivity study, the sensitivity of the functionalized EIS sensor with PEMs to the other cations in the applied electrolyte, namely to sodium ions has been investigated. Figure 5.18 depicts the ConCap response of EIS structures with the fourth PSS-4 (a) and eighth PSS-8 (b) layer as outermost layer measured in NaCl solutions with different concentrations.

In the case of PSS as a terminating layer, the sensor signal is changed towards the direction of an additional positive charging of the EIS sensor surface (corresponding to a more negative

sensor signal in Fig. 5.18 due to the feedback control in the ConCap mode) with increasing NaCl concentration.

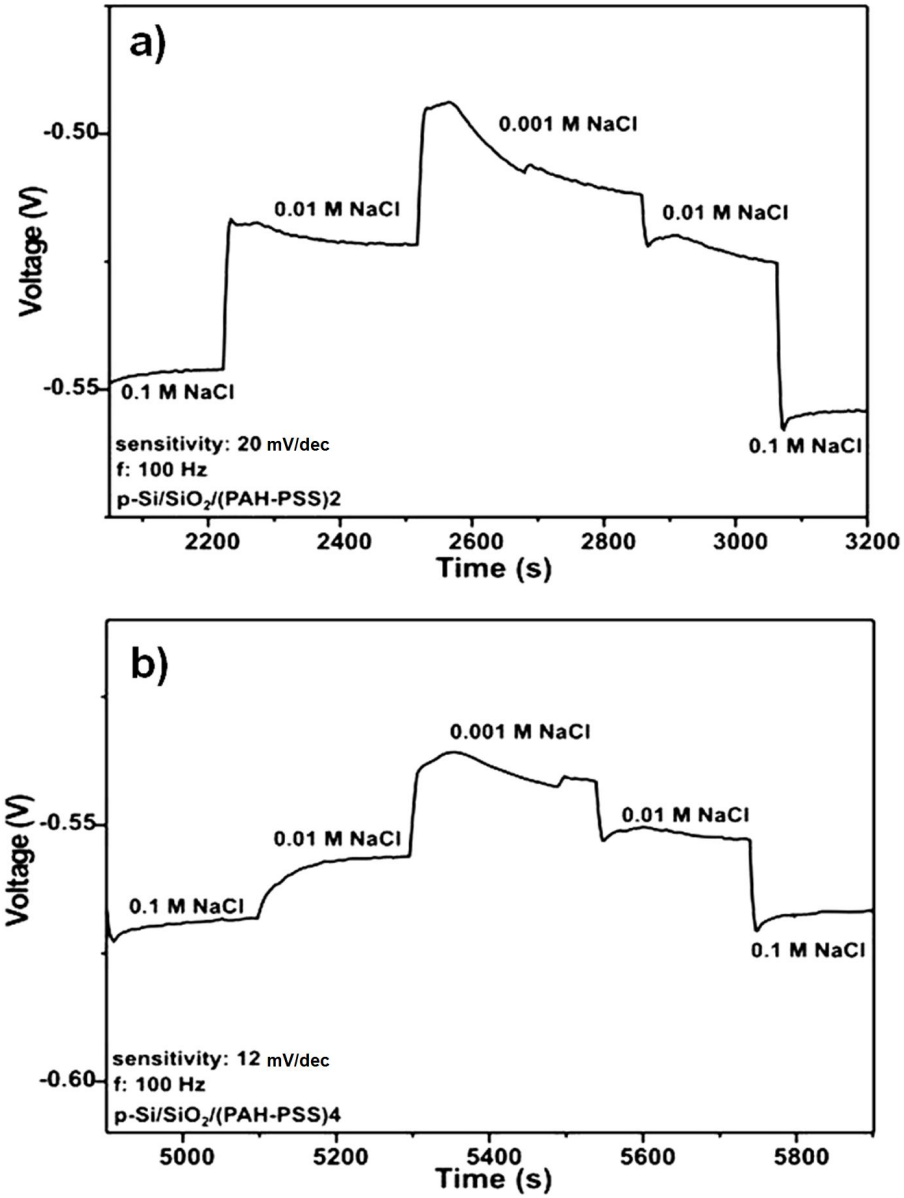

Fig. 5.18: ConCap response of EIS structures with post-deposited PEMs with the 4th PSS-4 (a) and 8th PSS-8 (b) layer as outermost layer measured in NaCl solutions with different concentrations.

These observations are in good agreement with similar measurements performed on bare p-Si/SiO_2 structures. The average ion sensitivity was about 20 and 12 mV/pNa for the EIS sensors with PSS-4 and PSS-8 as terminating layers, respectively. Thus, a decrease in ion sensitivity with increasing number of adsorbed polyelectrolyte layers has been observed. On the other hand, the obtained sensitivity values are much higher than those of bare SiO_2 layers (3-5 mV/pNa). Therefore, the ion sensitivity of the functionalized EIS sensor can not be addressed to or at least only to the SiO_2 layer [SchgAb09].

As PEMs are permeable to ions and molecules, they are also favorable for (bio-)chemical sensing applications. Recently, PEMs have been used for the immobilization of the enzyme urease or glucoseoxidase onto the electric transducers [WuGu02, GaCha00]. The permeability of PEMs allows the penetration of the analyte to reach the particular enzyme. On the other hand, the enzymatic reaction product can penetrate through the PEM and reach the transducer, where it can be detected. In the next section, a new method for enhanced biosensing using PEMs is, therefore, introduced.

5.2.4 Polyelectrolyte/enzyme multilayer: New strategy for enhanced field-effect biosensing

In this research study, PEs have been used not only as a model system for studying of molecular interactions but also for preparation of a field-effect-based biosensor by functionalization of the gate surface of the FED with a pH-responsive weak polyelectrolyte/enzyme multilayer, prepared by LbL technique. The proposed sensor structure is capable to sense changes in both the local pH value near the gate surface and the charge of macromolecules induced via enzymatic reaction, thus resulting in a higher sensitivity.

5.2.4.1 EnFEDs functionalized with weak polyelectrolyte/enzyme multilayer

The generic approach is exemplarily demonstrated by realizing a penicillin biosensor using a field-effect capacitive p-Si/SiO_2 EIS structure functionalized with a PAH/penicillinase multilayer. For comparison, the characteristics of an EIS penicillin biosensor with adsorptively immobilized penicillinase (but without PEMs) was studied. The determination of penicillin is very important in medicine, fermentation processes, food and drug industries.

Fig. 5.19 shows the schematic structure and functioning principle of a capacitive enzyme-modified EIS biosensor (in this work, penicillin biosensor with the adsorptively immobilized enzyme penicillinase; Scheme 1) and an EIS biosensor functionalized with a pH-responsive weak polyelectrolyte/enzyme multilayer (Scheme 2). The commonly used operational principle of penicillin-sensitive EnFEDs (enzyme-based FEDs) is as follows [CarJan80, DzySol06, SchgPog06, PogTh01, AbPog08b]: the pH-sensitive transducer material (here: SiO_2) detects variations in the H^+-ion concentration resulting from the catalyzed hydrolysis of penicillin by the enzyme penicillinase according to the reaction presented in Figure 5.19.

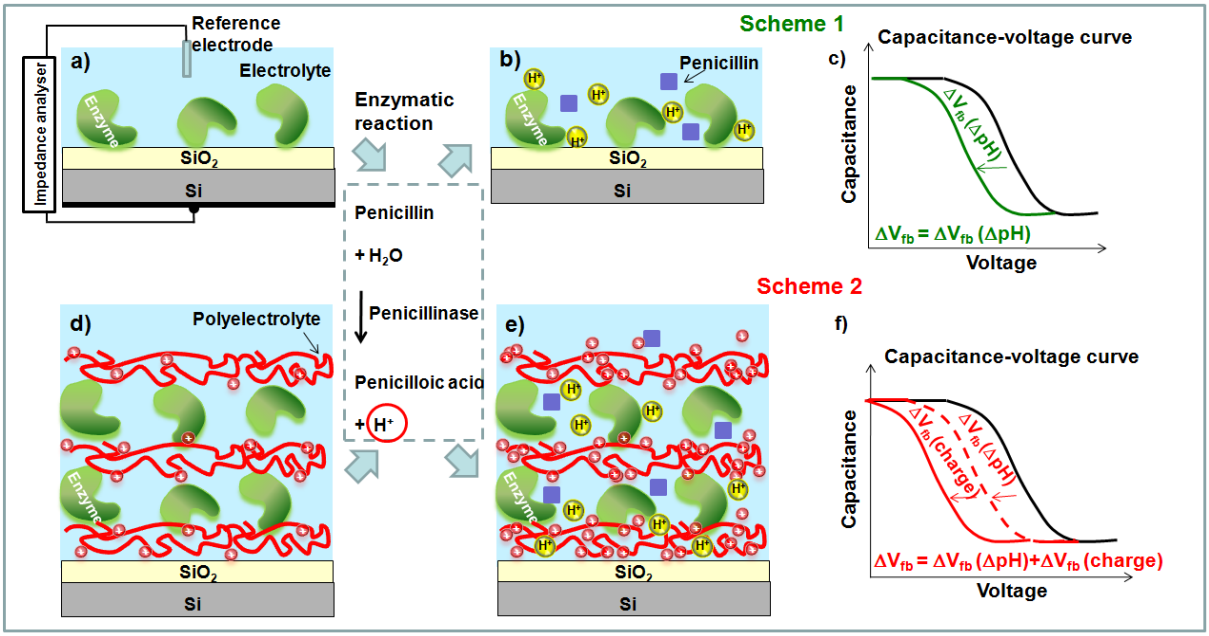

Fig. 5.19: Schematic structure (a,d), operation principle (b,e) and capacitance-voltage curve (c,f) for an EIS penicillin biosensor with adsorptively immobilized enzyme penicillinase (Scheme 1) and an EIS biosensor functionalized with a pH-responsive weak polyelectrolyte/enzyme multilayer (Scheme 2), respectively.

The resulting local pH decrease near the surface of the SiO_2 layer will change the surface charge of the SiO_2 and thus, modulate the space-charge capacitance in the Si and consequently, the flat-band voltage and capacitance of the EIS structure (Scheme 1, Fig. 5.19c). The recorded shift of ΔV_{fb}, or sensor signal depends on the penicillin concentration-dependent pH change (ΔpH) near the gate surface: $\Delta V_{fb} = \Delta V_{fb}(\Delta pH)$.

In case of the EIS sensor with the enzyme penicillinase embedded within the multilayer of a pH-responsive weak polyelectrolyte of PAH (Scheme 2), the local pH changes induced by the enzymatic reaction will also alter the effective charge in the polymer chains [Maus04] and the charge density in the multilayer, causing an additional shift of the *C-V* curve along the voltage axis (Fig. 5.19f). The resulting ΔV_{fb} or sensor-output signal will be defined by both the penicillin concentration- or pH-dependent charge changes of the SiO_2 surface and within the polyelectrolyte/enzyme multilayer: $\Delta V_{fb} = \Delta V_{fb}(\Delta pH) + \Delta V_{fb}(PEM)$. Thus, for the EnFEDs functionalized with a weak polyelectrolyte/enzyme multilayer, an amplification of the sensor-output signal and higher analyte sensitivity can be expected. Moreover, in contrast to the adsorptive immobilization method, an entrapment of enzymes in a stable polyelectrolyte multilayer could provide a larger amount of enzymes immobilized per sensor area as well as reducing enzyme leaching effects and thus, enhance the stability and shelf life of the biosensor.

5.2.4.2 Preparation of EIS penicillin biosensors

Two types of penicillin biosensors have been prepared using different enzyme immobilization methods:

- p-Si/SiO_2/penicillinase structure with adsorptively immobilized penicillinase;
- p-Si/SiO_2/(PAH-penicillinase)$_3$-PAH structure with three bilayers of PAH/penicillinase, and PAH as outermost layer fabricated by LbL technique.

The enzyme solution was prepared by dissolving the enzyme penicillinase (EC 3.5.2.6., Bacillus cereus from Sigma, specific activity: 1650 units/mg protein) in a 200 mM TEA (trimethanolamine) buffer, pH 8. For the adsorptive immobilization of penicillinase, 80 µl enzyme solution per sensor were pipetted onto the chip surface, incubated at room temperature for about 1 h and dried in N_2 atmosphere.

For the preparation of the p-Si/SiO_2/(PAH/penicillinase)$_3$-PAH biosensor, the sensor chip was exposed to the PAH (50 µM PAH, 0.1 M NaCl, pH 6) solution for 5 min followed by rinsing with ultrapure water and dried with N_2. Then, the enzyme penicillinase was immobilized on the modified sensor surface using the same immobilization protocol for the p-Si/SiO_2/penicillinase sensor described above. These procedures were repeated until the desired number of PAH/penicillinase bilayers (in this study, three bilayers) was prepared.

Before their first use, the prepared penicillin biosensors were incubated in a working buffer for at least 1 hour to let the enzyme membrane equilibrate. When not in use, the sensors were stored in Titrisol buffer, pH 7, at 4 °C.

The morphology and coverage of the functionalized sensor surface was studied by means of SEM. As an example, Figure 5.20 shows a SEM picture of the surface morphology of the penicillin biosensor with the adsorptively immobilized enzyme penicillinase (a) and functionalized with a (PAH-penicillinase)$_3$/PAH LbL film (b), respectively. As can be seen, an incorporation of enzymes within the polyelectrolyte multilayer provides a higher surface coverage and larger amount of penicillinase immobilized per sensor area in comparison to the adsorptive immobilization method.

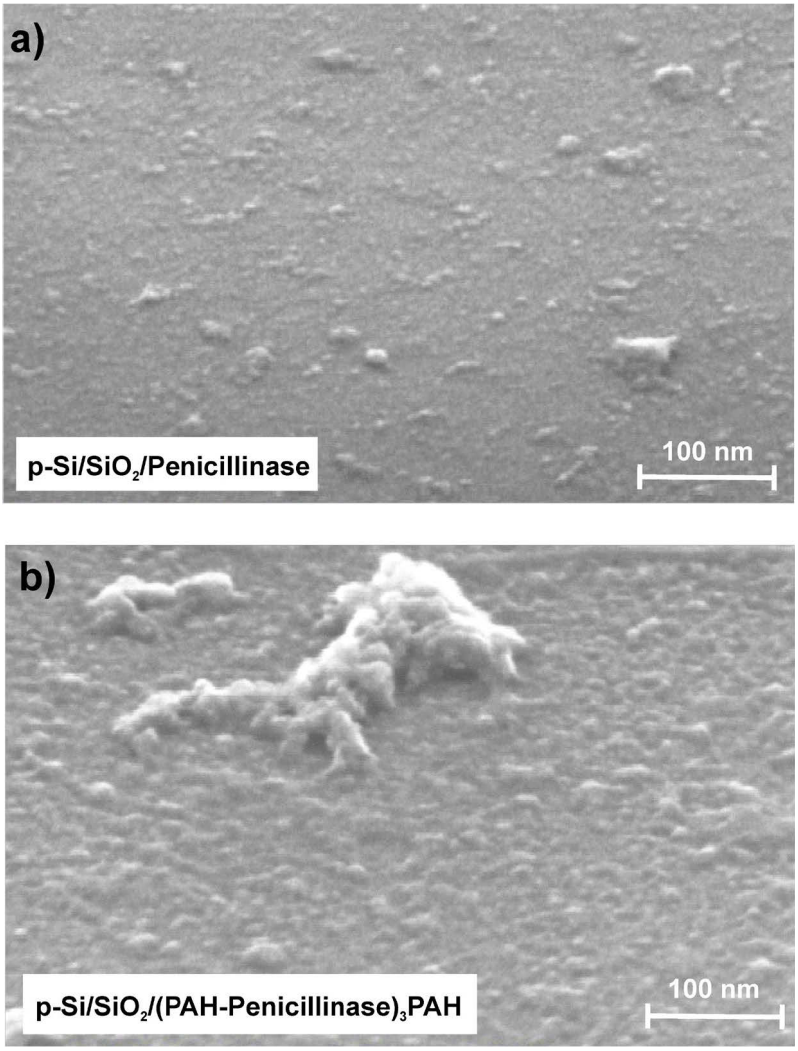

Fig. 5.20: SEM picture of the surface morphology of a 30 nm thick SiO_2 film functionalized with penicillinase (a) and (PAH-penicillinase)$_3$PAH (b).

This is also supported by additional spectrophotometric measurements of the enzyme activity. Spectrophotometric assays for determining the β-lactamase activity were carried out by measuring changes in the absorbance at 482 nm using the spectrophotometer XION-500 (Hach Lange, Germany). The measurements were performed at 25 °C in 0.2 mM polymix buffer solution (pH 8, 100 mM KCl) containing 300 µM nitrocefin as substrate. The obtained values of enzyme activity for freshly prepared p-Si/SiO_2/penicillinase and p-Si/SiO_2/(PAH-penicillinase)$_3$/PAH structures were 0.11 µM/min and 0.32 µM/min, respectively. As expected, the higher enzyme activity was achieved in the case of the enzyme entrapment within the polyelectrolyte multilayer.

5.2.4.3 pH sensitivity of EIS sensors functionalized with PAH

Since the functioning principle of the presented sensors is based on the detection of variations in the H^+-ion concentration induced by the enzymatic reaction before penicillin measurements, the pH sensitivity of the p-Si/SiO_2, p-Si/SiO_2/PAH and p-Si/SiO_2/(PAH-penicillinase)$_3$/PAH structures was respectively verified.

As an example, Figure 5.21 depicts a typical dynamic ConCap response of an EIS structure before and after functionalization of the sensor surface with PAH recorded in Titrisol buffer with different pH values. The bare (non-functionalized) EIS sensor shows an average pH sensitivity of 38 mV/pH in the range from pH 5 to pH 8. After the adsorption of a PAH monolayer on the sensor surface and after the functionalization with a (PAH-penicillinase)$_3$-PAH LbL film, an increase in the pH sensitivity (48.5 mV/pH and 52 mV/pH, respectively) was observed (see Fig. 5.21b). The higher pH sensitivity of the functionalized EIS sensors could be explained by the assumption that both the underlying gate insulator (SiO_2) and the mono- or multilayer of weak polyelectrolyte itself contribute to the pH-dependent sensor response. In fact, recent investigations as well as experiments in section 5.2.3.5 show that LbL polyelectrolyte multilayers are not completely dense and permeable to protons, amongst others [SchgAb09, Nef06, Schf03b]. Therefore, pH changes in the surrounding electrolyte will change the local pH within the LbL film that will be additionally detected by the underlying pH-sensitive SiO_2 layer.

On the other hand, PAH is a weak polyelectrolyte having pH-responsive ionisable groups [Maus04]. It has been reported that the ionisation degree and therefore, the molecular charge of weak polyelectrolytes in the embedded layer changes with both the pH of the surrounding solution and the net charge of the outermost layer [Carr04, Xie02]. The dissociation constant (pK_a) reported for PAH in bulk solution is 8.6 [Petr03, KhaSuk03]. However, an incorporation of the PAH into multilayer shifts the pK_a value of PAH by approximately 2-3 pH units to the alkaline region, i.e. pK_a ~10.6 [Maus04]. The whole protonation of PAH in a multilayer is achieved at approximately pH 3 [Maus04]. Thus, for pH values used in the experiments in Figure 5.21, the PAH can be considered as positively charged. Variations in pH between pH 5 and pH 8 will change the polymer charge that, in fact, has been detected in this study.

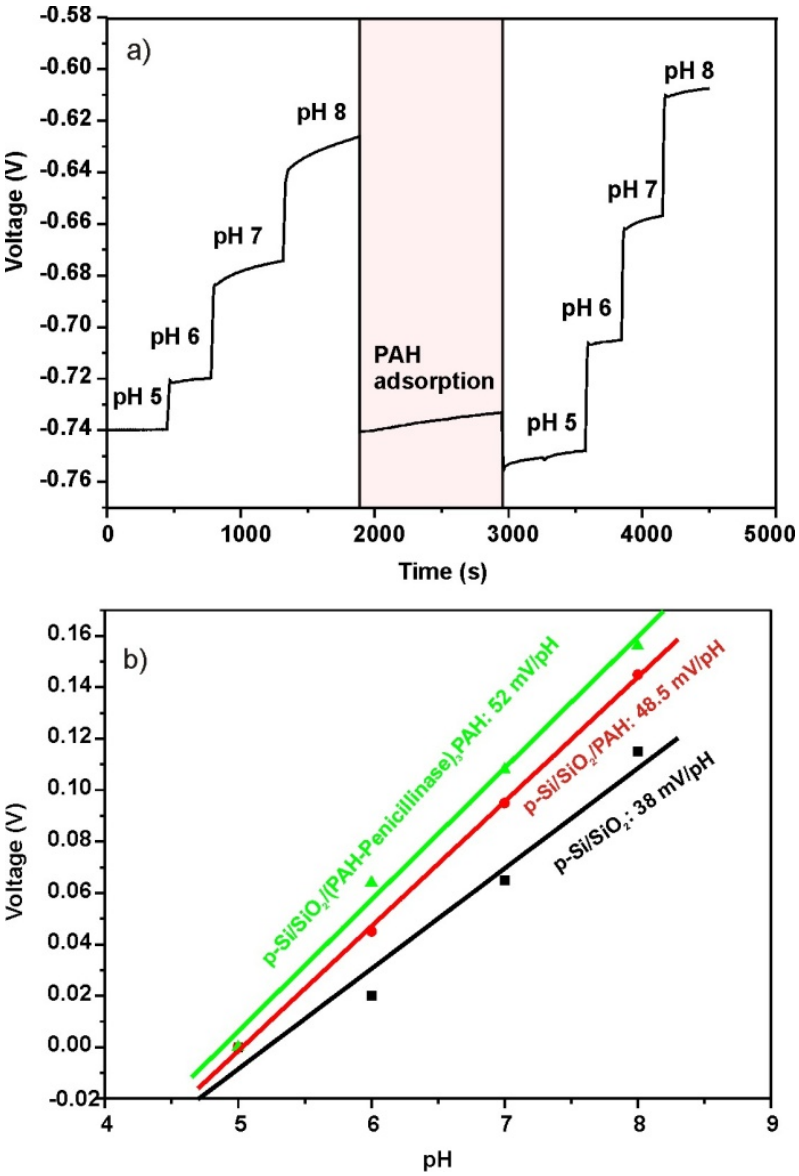

Fig. 5.21: The ConCap response of an EIS structure before and after functionalization of the sensor surface with PAH recorded in Titrisol buffer with different pH values (a) and corresponding calibrations curves (b). The calibration curve for the EIS sensor functionalized with a (PAH/penicillinase)$_3$/PAH LbL film is presented, too.

Hence, the pH-responsive effective molecular charge of the outermost weak polyelectrolyte (in this study, PAH) or the polyelectrolyte multilayer will contribute to the pH response of the functionalized EIS sensor, resulting in a higher sensitivity in comparison with a bare EIS sensor. It is well known that FEDs are capable of detecting of charge changes that occur directly at the gate surface or within the Debye length from the surface. The counter-ion condensation effect will mask or reduce the expected signal, especially in high-ionic strength solutions, where the Debye length is small (~1 nm in a 100 mM KCl solution). The results of this study (see section 5.2.3) as well as other reported results (see e.g., [Nef06]) have demonstrated that the ion concentration within the multilayer can be 2-3 orders of magnitude smaller than in the

bulk solution. Therefore, the Debye length within the multilayer could be ~10 nm and more. Thus, field-effect sensors are feasible for the detection of charge changes in a PEM consisting of up to 5-6 bilayers [AbPog10].

5.2.4.4 Penicillin detection

The EIS penicillin biosensors have been characterized in penicillin solutions with different content of penicillin G from 5 μM to 10 mM by means of ConCap method. The number of tested biosensors from each group was n=3. The penicillin solutions were prepared by dissolving penicillin G (benzyl penicillin, 1695 units/mg, Sigma) in the working buffer. As working buffer, a 0.2 mM polymix multi-component buffer solution containing 100 mM KCl as an ionic strength adjuster was used [PogTh01]. The pH of the polymix buffer was adjusted to pH 8 by titration with NaOH solution.

For the measuring procedure, about 1 ml of the working buffer or particular penicillin solution was applied to the EIS gate surface and the sensor-output signal was monitored for about 4-8 min. Typical ConCap responses of freshly prepared p-Si/SiO_2/penicillinase and p-Si/SiO_2/(PAH-penicillinase)$_3$/PAH biosensors measured in polymix buffer solution with different penicillin concentrations from 0.005 to 10 mM are shown in Figure 5.22.

With increasing penicillin concentration, the concentration of the H^+ ions resulting from the enzymatic reaction is also increased. As a result, the capacitance-voltage curve is shifted in the direction of a more negative flat-band voltage, the voltage that is necessary in order to adjust the constant capacitance. The recorded sensor-output signal is directly correlated with the respective penicillin concentration in the solution. The average penicillin sensitivity for three tested biosensors from each group was about 45 mV/dec and 100 mV/dec in the linear range of 0.25-2.5 mM penicillin G for the p-Si/SiO_2/penicillinase and p-Si/SiO_2/(PAH-penicillinase)$_3$-PAH sensors, respectively.

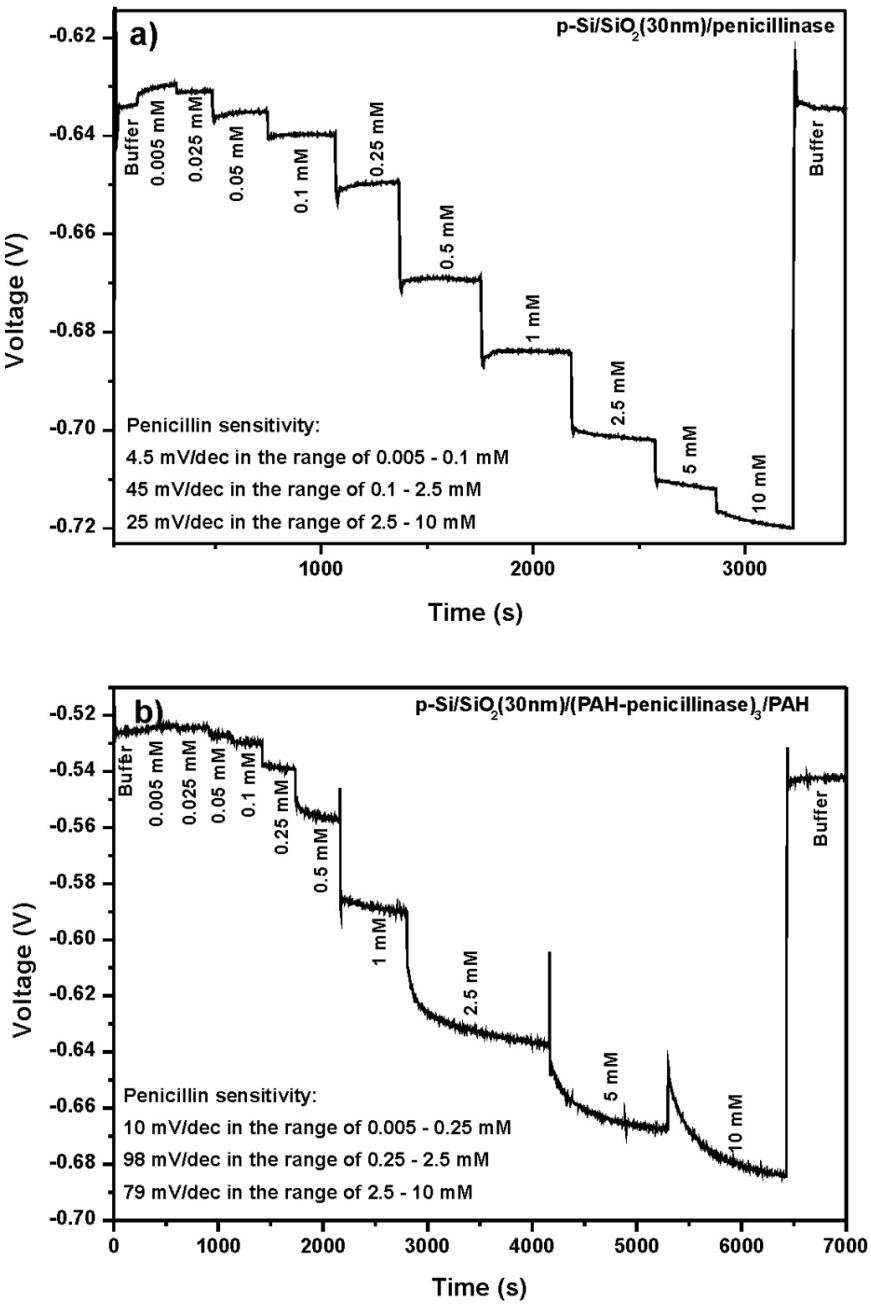

Fig. 5.22: Typical ConCap response of the developed p-Si/SiO_2-penicillinase (a) and p-Si/SiO_2/(PAH-penicillinase)$_3$/PAH (b) penicillin biosensor, respectively.

The lower and upper detection limit is around 0.02 and 10 mM, respectively. Since the penicillin molecules need time to penetrate in the multilayer and to diffuse to the penicillinase molecules, the response time of the p-Si/SiO_2/(PAH-penicillinase)$_3$-PAH sensors was somewhat higher than that of the p-Si/SiO_2/penicillinase sensors.

As expected, the higher penicillin sensitivity has been achieved for EIS sensors where the enzyme penicillinase has been embedded within the weak polyelectrolyte multilayer (PAH). The reason for the high pH and penicillin sensitivity of these biosensors and mechanism of

signal generation is already discussed in previous sections. In addition to the higher pH sensitivity of the p-Si/SiO_2/(PAH-penicillinase)$_3$-PAH structures, the higher surface coverage and/or higher activity of enzymes embedded in the more stable polyelectrolyte multilayer will also result in a higher penicillin sensitivity. Even after two months, the same biosensor has shown a clear dependence on the penicillin concentration with a sensitivity of about 90 mV/dec. The loss of the penicillin sensitivity was around 10-12%. Thus, an incorporation of enzymes in a stable, weak polyelectrolyte multilayer reduces enzyme-leaching effects as it also enhances the shelf life of the biosensor [AbPog10].

In summary, this chapter focused on the theoretical and experimental study of the PEM build-up using capacitive EIS sensors as a model system for planar-like, molecular layer formation. An electrostatic model taking into account the Debye screening by mobile ions in PEMs was developed, which shows that the amplitude of the change of the surface potential via formation of the PEM has the tendency to decrease by increasing the layer number and ionic strength in the electrolyte. In the experimental part, the change of the thickness of the PEM, morphology and hydrophilicity of functionalized sensor surface upon the PEM build-up was investigated using physical characterization methods. The systematic increase of the PEM thickness, roughness and hydrophilicity after adsorption of each PE layer (up to 26 layers) was observed. Moreover, the PEM formation and the effect of ionic strength of the electrolyte as well as the influence of using buffered and unbuffered solution were electrochemically studied using EIS sensors. It seems that both the intrinsic PE molecular charge and ion-concentration redistribution in the PEMs contributed to the detected sensor signal. Furthermore, the pH- and ion-sensitivity measurements of functionalized EIS sensors with PEMs showed the permeability of the PEM structure to protons and sodium ions, which were used as the basis for the preparation of enzyme based biosensors. As an example, the use of LbL deposition of a PAH/penicillinase multilayer on EIS sensors as a penicillin biosensor with a wide detection range led to high sensitivity and longer life time. Generally, this new method can be used for the preparation of other EnFED-type biosensors.

The information gained was applied in choosing an optimized strategy for the DNA hybridization/denaturation detection using field-effect sensors shown in the next chapter. This includes the choice of a suitable measuring buffer solution, DNA immobilization method and measuring setup.

Chapter 6

6 Label-free detection of DNA using capacitive FEDs

In this chapter, a new approach for label-free electrical detection of DNA hybridization and denaturation using an array of individually addressable EISOI capacitors modified with gold-nanoparticle/DNA hybrids is presented. The capacitive field-effect-based structures detect charge changes of the Au-NP/DNA hybrids induced by the hybridization and denaturation event. In order to achieve a high sensor signal, DNA hybridization was performed in a high ionic-strength buffer, whereas the corresponding signal changes were detected in a low ionic-strength buffer using differential mode measurements. In addition, fluorescence microscopy was applied to proof the DNA immobilization, hybridization and denaturation events. Furthermore, based on the Grahame equation and the linear Poisson-Boltzmann theory, an electrostatic model for a brush-like formed DNA layer on the sensor surface was developed, which demonstrates the potential variations on the sensor surface upon DNA immobilization, hybridization and denaturation. The presented results in this chapter are partially published or submitted in scientific journals [AbPog11a, AbPog11b, AbPed10]

6.1 DNA immobilization, hybridization and denaturation procedures

The method in which nucleic acids are bound to the substrate is critical for the performance of a DNA sensor. Binding via the bases is potentially detrimental to the performance, as the bases are responsible for any hybridization event that occurs. Whatever the nature of the substrate, there are only a few attachment techniques, including covalent linkage (for example, through silanization of the substrate), assembly of the probe on the substrate, physical adsorp-

tion, etc. While the physical adsorption method presents a convenient procedure, a covalent immobilization method may be more favored [Zou08, Han06]. Covalent binding of oligonucleotides assures long-term stability and thus maintenance of the device's performance. As defined, the density of the immobilized ssDNA molecules is important for controlling the interaction and hybridization of the ssDNA with the complementary one [Pirr02]. Commonly used immobilization strategies of DNA on the chip surface involve chemical modification of silicon oxide based surfaces. First, it is necessary to coat the chip surface with an organosilane that can covalently bind to the silicon oxide surface (silanization). The other end of the organosilane bearing the molecule is properly functionalized for the following conjugation with a probe ssDNA [Zou08].

In this study, ssDNA probe molecules were immobilized on the surface of Au-NPs deposited on the silanized gate of capacitive EIS and EISOI sensors, which provides a defined density of immobilized ssDNA. Figure. 6.1 illustrate a flowchart of the steps of surface modification.

Silanization and functionalization of sensor surface with Au-NPs

Before ssDNA immobilization, the cleaned sensor surface was first silanized by exposing it to a freshly prepared mixture of 10% MPTES (3-mercaptopropyl trimethoxysilane) and toluol for 1 hour followed by washing in toluol, acetone, isopropanol and water, respectively (Fig. 6. 1a). For silanization, the reactive methoxyl groups are first hydrolyzed by the surface water on a hydrated silanol surface, followed by condensation. Simultaneously, the formed silane oligomers in-situ bind (physisorption via hydrogen binding) to the surface. By further condensation between free silanol groups of silane oligomers and the surface silanols, the film attaches covalently across the surface [SilLe91]. The thickness of the silane layer was controlled by imaging ellipsometry and was about 1.2±0.2 nm.

For deposition of Au-NPs on the sensor surface, the thiol-functionalized surface was made to react overnight with a dispersion of TOA (tetraoctylammonium)-stabilized Au-NPs (obtained from Hebrew University) in toluene (1 mM) [GuAb08] followed by washing with toluol (5 times), acetone, isopropanol and distilled water. The sulfur atoms of the MPTES will replace some of the TOA molecules, thus binding the Au-NPs to MPTES (Fig. 6.1b). In a similar manner, the thiol-modified probe ssDNA molecules bind to the Au-NPs. The sulfur-gold bond is a strong covalent bond with a high bond enthalpy of 418 ± 25 kJ/mol [Web5].

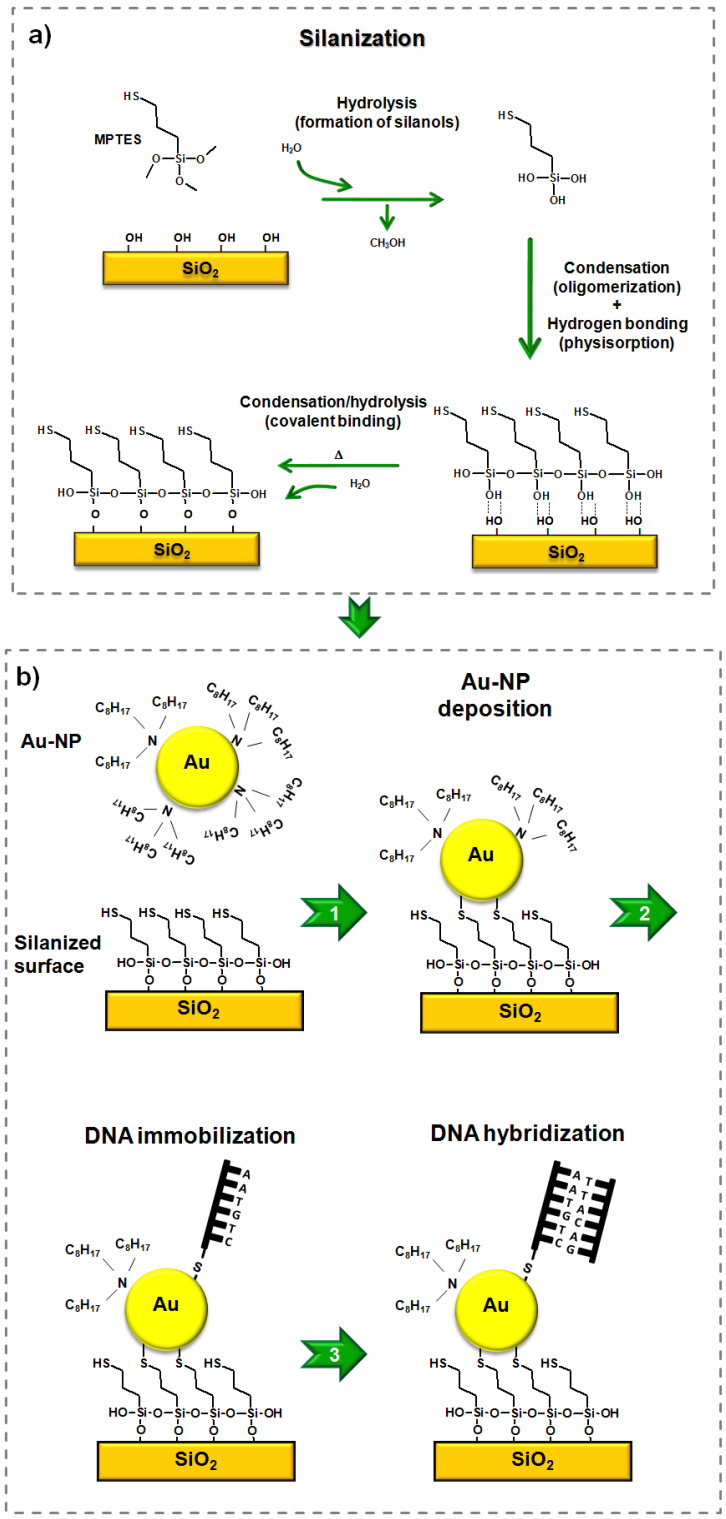

Fig. 6.1: Flowchart of the (a) silanization (adopted from [Zou08]) and (b) further surface-modification steps.

To control each modification step, the sensor surface was characterized (after each functionalization procedure) by means of water contact-angle measurements with an OCA 20 System (Dataphysics, Germany) with a 5 µl drop of ultrapure water. Figure 6.2 presents results of the water contact-angle measurements of a bare SiO_2 surface, after O_2-plasma treatment of the SiO_2 surface, after silanization and after functionalization of the surface with Au-NPs. The

hydrophilicity of the surface is increased significantly after the O_2-plasma treatment from a contact angle of ~75° for a bare SiO_2 (Fig. 6.2a) to ~5° after O_2-plasma treatment (Fig. 6.2b). The increasing of surface hydrophilicity is due to the increase in hydroxyl groups. The sensor surface modified with MPTES was more hydrophobic (the measured water contact angle was ~63°, see Fig. 6.2c) than that of after O_2-plasma treatment. Water contact-angle measurements show that the functionalization of the MPTES-modified sensor surface with Au-nanoparticles increases the hydrophobicity of the surface again (water contact angle was ~92°, see Fig. 6.2d).

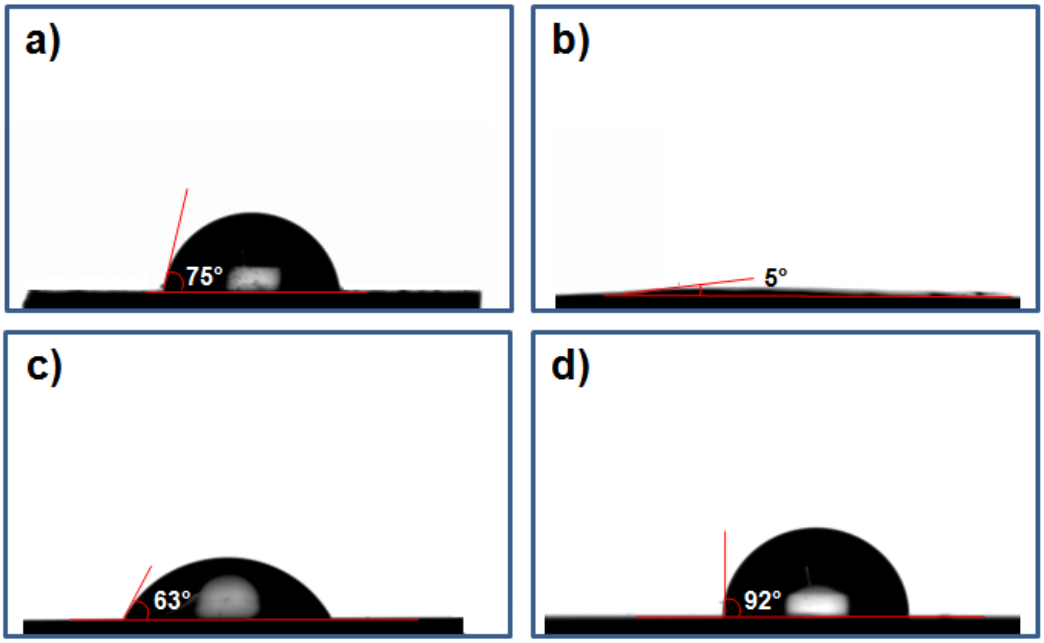

Fig. 6.2: Water contact angles on a bare SiO_2 surface (a), after O_2-plasma treatment (b), after silanization with MPTES (c) and after modification of silanized sensor surface with Au-nanoparticles.

The surface coverage of the Au-NPs was examined by means of scanning electron microscopy. The SEM micrograph in Figure 6.3 demonstrates a homogeneous coverage of the SiO_2 surface with Au-NPs. The diameter of Au-NPs (D_{Au-NP}) is ~5-8 nm. The average surface coverage with Au-NP (α_c) evaluated from several SEM images using the program ImageJ was 60-70%. Using Eq. 6.1, the density of Au-NPs (ρ_{Au-NP}) can be calculated as follows:

$$\rho_{Au-NP}\left(\frac{\mathrm{N_{Au\text{-}NP}}}{m^2}\right) = \frac{1(m^2)}{\pi.\left(\frac{D_{Au-NP}}{2}\right)^2}.\alpha_c \qquad (6.1)$$

This results in a density of ~(1-1.3) $\times 10^{16}$ Au-NPs/m^2 for Au-NP with an average diameter of D_{Au-NP} ~6 nm.

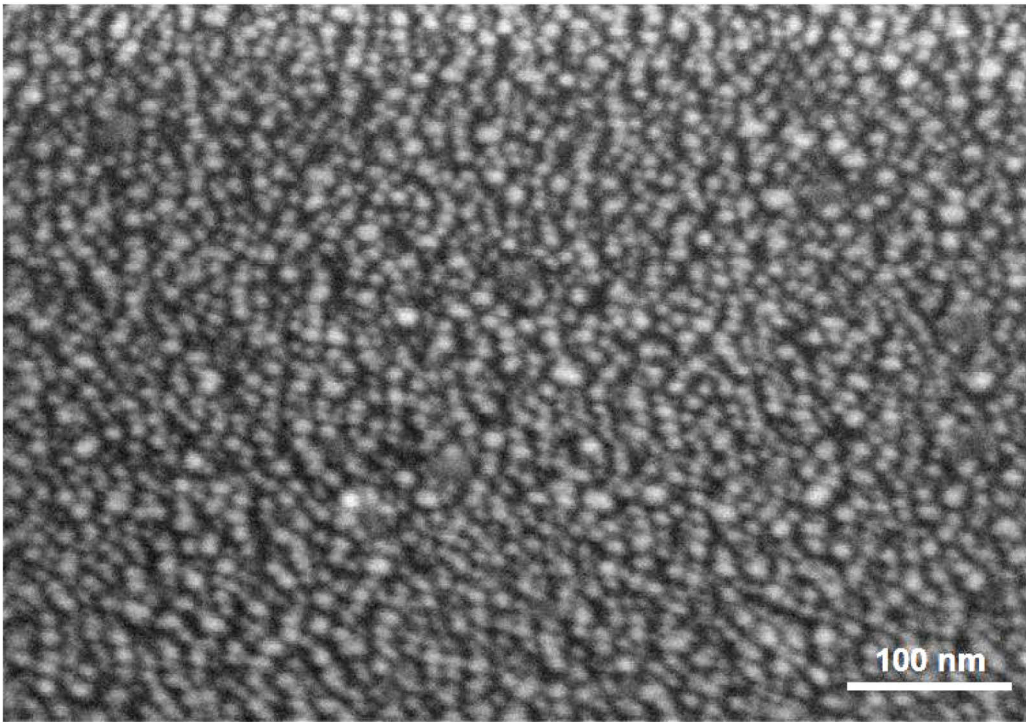

Fig. 6.3: SEM image of a SiO_2 surface covered with Au-NPs.

ssDNA immobilization

The immobilization of thiol-modified 20 base pair ssDNA (Eurofins MWG Operon, Germany) probe molecules on the surface of the Au-NPs was done by pipetting of 40 µl immobilization solution (5 µM ssDNA, 0.1 M phosphate buffer solution (PBS), pH 8.5) into the particular sensor surface, followed by incubating the sensors in humid conditions at 37 °C overnight. After immobilization, the sensor surface was washed in ultrapure water to remove not-attached ssDNA molecules and dried with nitrogen (see also Fig. 6.4).

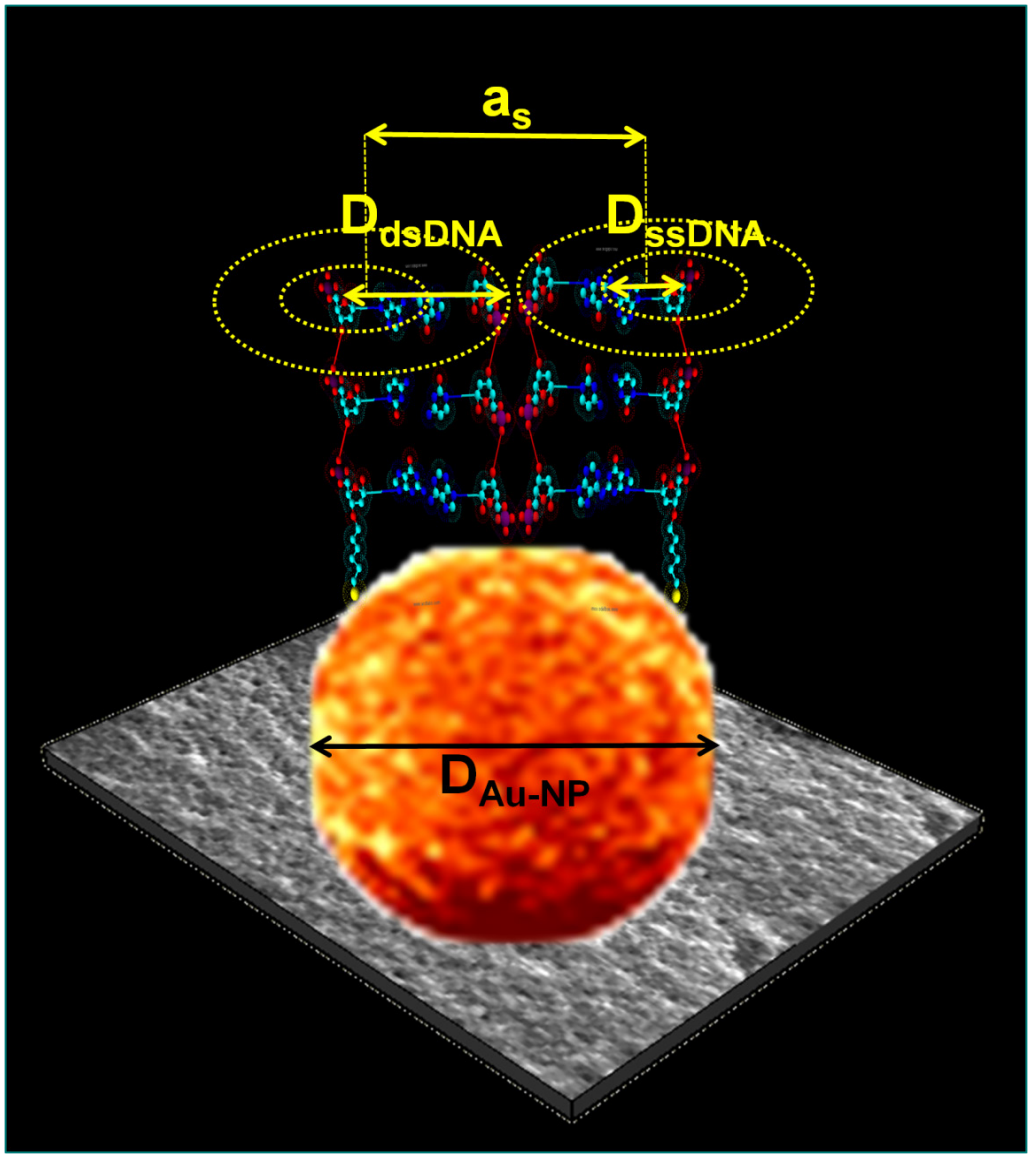

Fig. 6.4: Schematic of functionalized sensor surface with a Au-NP/DNA hybrid. The ssDNA and dsDNA form a hexagonal lattice of uniformly negatively charged, 6.4 nm long cylinders with a diameter of D_{ssDNA} =1 nm and D_{dsDNA} = 2 nm, respectively. The cylinders are arranged normal to the Au-NP surface with a center-to-center average separation distance of a_s. The oligonucleotides in this figure are sketched using "ChemSketch" software.

Using a density of deposited Au-NPs on the sensor surface of ρ_{Au-NP} ~1.2*10^{16} Au-NPs/m^2, the density of thiol-modified ssDNAs quasi-covalently bound to the Au-NPs was estimated. Geometrically, the upper hemi-sphere of every Au-NP is accessible for ss- and ds-DNA. Dense packing of dsDNAs with a dsDNA diameter of D_{dsDNA}=2 nm implies the minimum separation distance (a_s~2.D_{dsDNA}) of ~4 nm between the immobilized ssDNA axes (see Fig. 6.4) [PogCh05]. Thus, for Au-NPs with an average diameter of ~6 nm up to m=3-4 dsDNAs can potentially be deposited. The density of attached 20 base pair long DNA fragments is then $\sim 1.2\times10^{16} - 4.8\times10^{16}$ ssDNA/m^2 ($\rho_{DNA} \sim m \times \rho_{Au-NP}$).

DNA hybridization

For hybridization, a high concentrated solution (0.1 M PBS, pH 7, adjusted with 0.9 M NaCl) containing 5 μM of the target ssDNA (see Tab. 6.1) was utilized. The hybridization solution was heated to ~70 °C, and was then pipetted on the gate surface of the particular sensor. The sensors were left at room temperature for 15-30 min. After incubation, the sensor surface was washed (with distilled water for 1 min, 2 × SSC (sodium chloride-sodium citrate buffer) for 1 min, 1 × SSC for 1 min and rinsed again with distilled water) to remove non-hybridized target DNA molecules and finally, dried with nitrogen.

Tab. 6.1: DNA sequences used in this work.

Type	Sequence
Target ssDNA	5'-TGACTACATGCAGTGTTCAT-3'
Perfectly-matched thiol-modified ssDNA	5'THI-ATGAACACTGCATGTAGTCA-3'
Fully-mismatched thiol-modified ssDNA	5'THI-TACTTGTGATGTACATCAGT-3'
Fluorescent-labeled target ssDNA	5'-Cy3-TGACTACATGCAGTGTTCAT-3'
Fluorescent-labeled perfectly-matched thiol-modified ssDNA	5'THI-ATGAACACTGCATGTAGTCA-Cy3-3'
Fluorescent-labeled fully-mismatched thiol-modified ssDNA	5'THI-TACTTGTGATGTACATCAGT-Cy3-3'

The DNA denaturation process was done by applying a drop of 0.1 M NaOH to the sensor surface and leaving it for 1 min. Afterwards, the sensors were washed using the same protocol as for the hybridization procedure described above.

The sequences of the probe and target ssDNA molecules used in this work are presented in Table 6.1.

6.2 Optical detection of DNA immobilization, hybridization and denaturation

For verification of the DNA immobilization, hybridization and denaturation on the sensor surface, optical detection of DNAs labeled with Cy3 fluorescence markers was done.

For this purpose, separate p-Si/SiO_2 structures with a 100 nm SiO_2 layer were prepared and modified with Au-NPs. Fluorescence-microscopy measurements were carried out using an Axioplan 2 Imaging microscope (Zeiss, Germany). Since Cy3 markers on DNA emit at a wavelength of 570 nm, a specific filter for this wavelength was used. Digital images were taken after the immobilization, hybridization and denaturation experiments using the color CCD camera of the microscope.

To prove DNA immobilization, thiol-modified Cy3 fluorescence-marked fully-mismatched and perfectly-matched ssDNA molecules (see Tab. 6.1) were immobilized on different spots of the Au-NP-covered p-Si/SiO_2 chip. These spots with homogeneous distribution of fluorescence intensity are clearly visible in the fluorescence-microscopy images (Figures 6.5a, 6.5b).

This indicates that fluorescent-labeled probe ssDNAs were bound to the Au-NP-modified surface. Figure 6.5c shows the mean fluorescence-intensity values for six spots with immobilized perfectly-matched and fully-mismatched ssDNAs, as evaluated from fluorescence microscopy using the ImageJ program. These results indicate a reproducible density of ssDNAs immobilized on the Au-NP-modified surface by applying the immobilization protocols described above.

Figure 6.6 demonstrates fluorescence-microscopy images taken from the two spots with perfectly-matched and fully-mismatched ssDNA after the first hybridization (a), followed by denaturation (b) and re-hybridization (c) steps. The complementary target ssDNAs used in this experiment were fluorescence-labeled (Tab. 6.1).

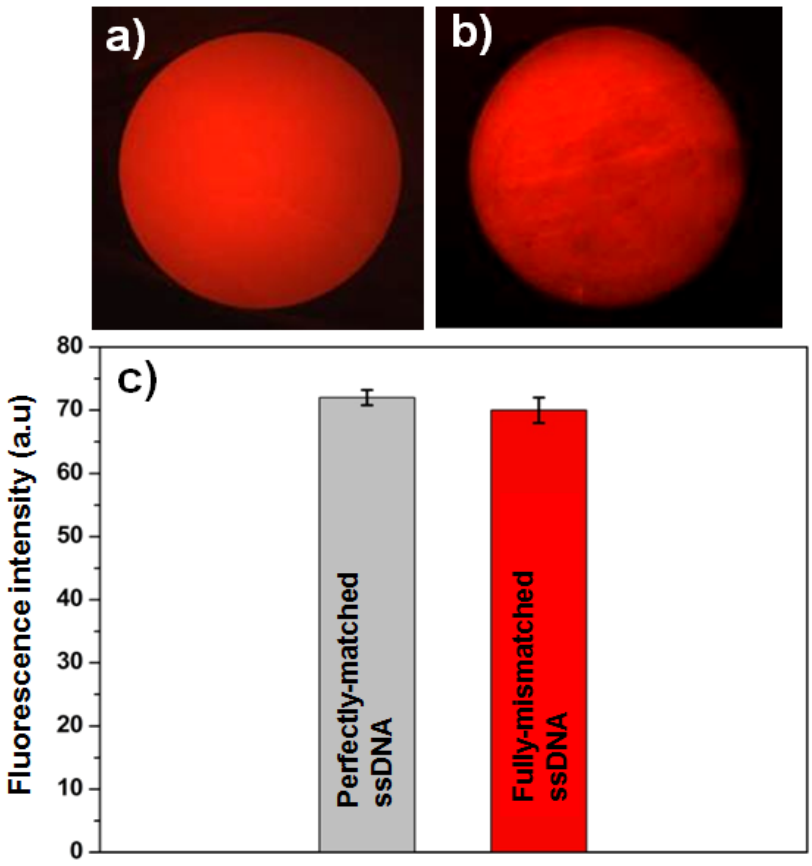

Fig. 6.5: Fluorescence-microscopy images taken from Au-NP-covered surface spots with immobilized Cy3-labeled thiol-modified perfectly-matched (a) and fully-mismatched (b) ssDNA molecules. c) The mean values of fluorescence intensity for six spots with corresponding probes as evaluated from fluorescence-microscopy images.

The images show a high fluorescence intensity after hybridization from the spot with immobilized ssDNA perfectly-matched to the target ssDNA sequence. This verifies the successful hybridization with complementary target molecules. In contrast, there was almost no fluorescence effect from the spot with fully-mismatched ssDNAs, indicating that no hybridization has occurred. After the denaturation, practically no fluorescence effect (the intensity was negligible compared to background) can be seen from the spot with perfectly-matched ssDNA. This confirms the removal of fluorescent-labeled target ssDNA and successful denaturation.

To study the replicability of DNA hybridization and denaturation procedures as well as stability of the sensor surface modified with Au-NPs/ssDNA hybrids, fluorescence-microscopy images were taken from the same spots after multiple hybridization and denaturation cycles. The results of these investigations are illustrated in Figure 6.6d. Even after four consecutive hybridization/denaturation cycles, the fluorescence intensity from the spot with immobilized ssDNA perfectly-matched to the fluorescence-labeled target ssDNA was sufficiently high,

≈87% of the intensity registered after the first hybridization step. These findings are in good agreement with results obtained for Au-NP/DNA-modified silicon surfaces [StrHa00, StrCa00].

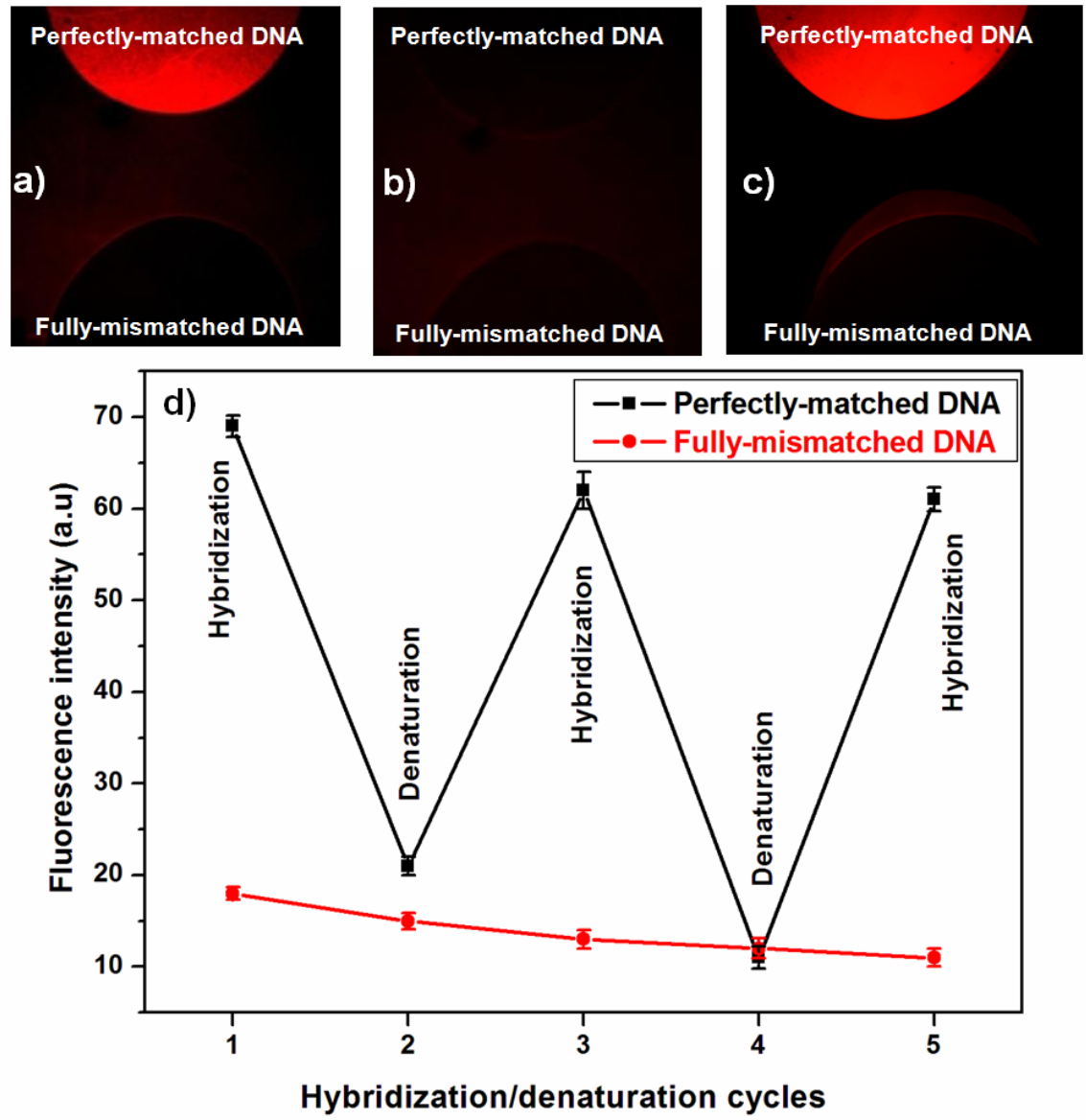

Fig. 6.6: Fluorescence-microscopy images taken from the two spots with perfectly-matched and fully-mismatched ssDNAs after consecutive steps of hybridization (a), denaturation (b), re-hybridization (c). Reproducibility of hybridization/denaturation procedure follows from a "zig-zag" variation in measured intensity (d).

6.3 Label-free electrical detection of DNA hybridization and denaturation

To reduce the effects of different disturbing factors (e.g., possible pH or ionic strength changes, adsorption of target ssDNA on the gate surface not covered with Au-NPs, temperature

change, sensor drift, etc.) and thus, to achieve more reproducible signals, the DNA-hybridization and denaturation measurements were carried out in a differential mode setup (see Fig. 6.7).

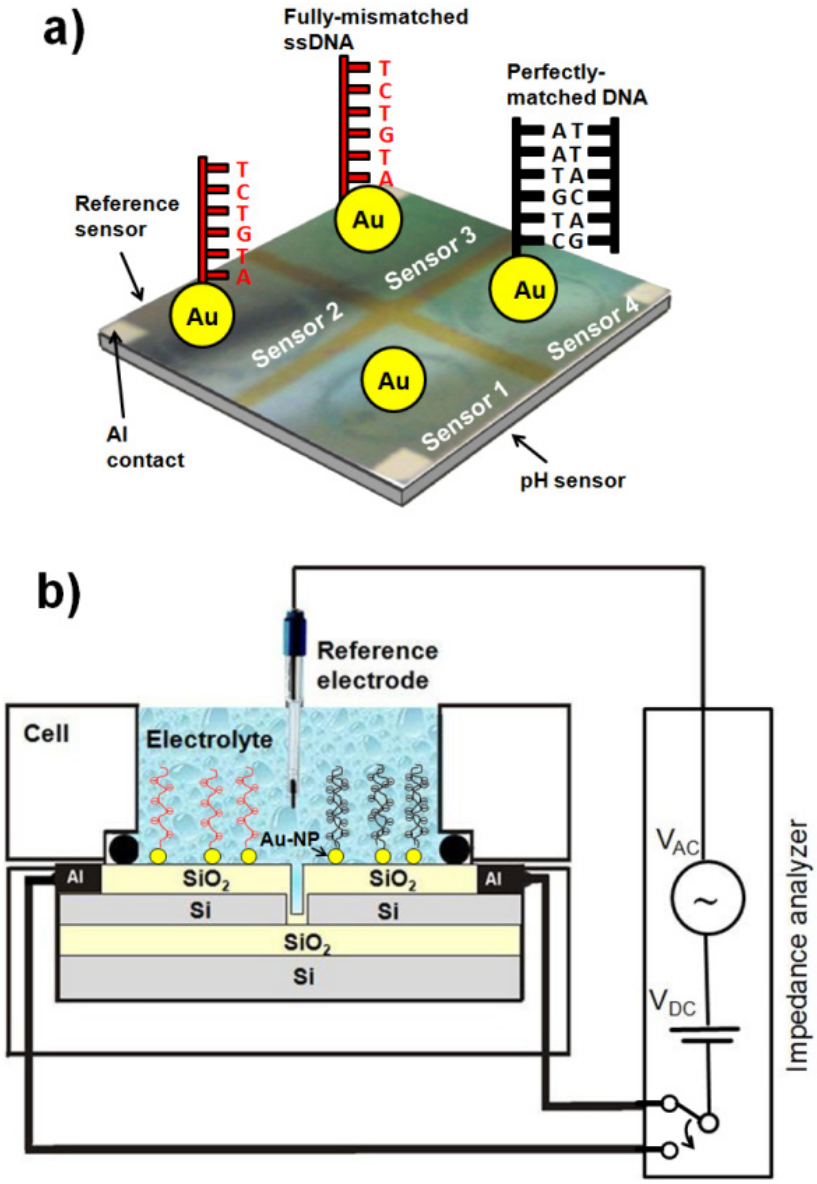

Fig. 6.7: Schematic of a 4-channel EISOI chip modified with Au-NP/DNA hybrids (a) and measurement setup (b) used for the label-free electrical detection of DNA hybridization and denaturation in differential mode.

Moreover, in order to minimize the screening of the DNA's intrinsic charge by counterions and to achieve a high sensor signal, the DNA hybridization was performed in a high ionic strength solution. The changes in the sensor-output signal caused by hybridization and denaturation events were on the contrary readout in a low ionic strength solution (0.2 mM PBS, pH 7.5).

Figure 6.7 presents the schematics of a 4-channel EISOI sensor modified with Au-NP/DNA hybrids (a) and the measurement setup (b) applied for the label-free, electrical detection of DNA hybridization and denaturation. In contrast to conventional capacitive EIS sensors on a Si chip, the developed sensor array allows an addressable biasing and readout of multiple nanoplate EISOI capacitive sensors on the same SOI chip. In this study, sensor 4 was immobilized with the probe ssDNA perfectly matching to the target ssDNA sequence, while sensor 2 and sensor 3 were immobilized with the fully-mismatched probe ssDNAs. Sensor 2 was not exposed to the hybridization solution and was used as a reference sensor for differential mode measurements. Sensor 1 was used for pH control.

The EISOI sensors have been characterized by means of ConCap method, which allows a direct dynamic monitoring of potential changes at the gate/electrolyte interface caused by the DNA hybridization or denaturation.

Figure 6.8 shows an example of DNA-hybridization and denaturation detection with the nanoplate EISOI chip in a differential mode setup. The ConCap curves in Fig. 6.8 represent the net differential output signals between sensor 3 and sensor 2 ($\Delta V_{3\text{-}2}$) as well as sensor 4 and sensor 2 ($\Delta V_{4\text{-}2}$). They were recorded in a 0.2 mM PBS (pH 7.5), before DNA hybridization and after the hybridization, denaturation and re-hybridization event. A high positive signal change of $\Delta V_{4\text{-}2}$~120 mV was registered after the DNA hybridization for sensor 4 immobilized with perfectly matched ssDNA, while practically no signal changes were observed for sensor 3 with fully-mismatched ssDNA. The positive signal shift in the ConCap mode corresponds to a more negative gate-surface charge, which can be attributed to additional negative charges of the hybridized dsDNA. The observed hybridization signals were 3-4 times higher than those previously reported in the study of a single capacitive SiO_2-gate EIS sensor without Au-NPs (24-33 mV) [PogIn07,PogAb07] and about 6 times higher than for a Si_3N_4-gate EIS structure (~14 mV) [SakMiy05].

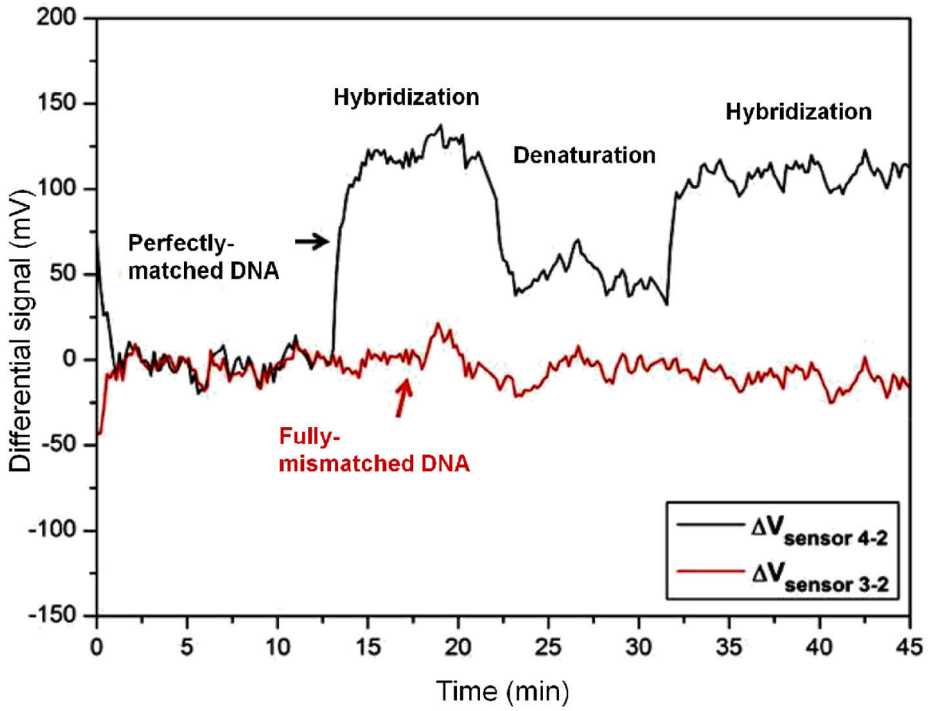

Fig. 6.8: Differential ConCap measurement of DNA hybridization and denaturation events with EISOI sensor array.

After DNA denaturation, the value of $\Delta V_{4\text{-}2}$ revealed a decrease of 90 mV that corresponds to a DNA-denaturation efficiency (β) of about 75%. As expected, no significant changes in the response signal were recorded after DNA denaturation for sensor 3 with immobilized fully-mismatched DNAs. After the second hybridization step, an increase of $\Delta V_{4\text{-}2}$ of about ~80 mV was recorded again. The recorded hybridization signals are replicable (about 120 mV after the first and 110 mV after the second hybridization procedure) showing that this has a good correlation with fluorescence-microscopy investigations in Ch. 6.2.

It is worth mentioning that the suggested method is only efficient and amenable for detection of the DNA-hybridization event for pretty short DNA fragments, L<50 base pairs. The hybridization efficiency for longer DNA sequences is reduced considerably together with the accuracy of signals detected. The preparation of DNA microarrays with short oligonucleotide (15-30-mer) is favorable because of a more precise detection of shorter nucleotide polymorphisms, which includes single nucleotide differences [Zou08]. Short oligonucleotides are used in diagnostic as well as for environmental microbial microarrays [Bod03, Zou08, LoSch05, SrDi04].

6.4 Sensor-potential changes upon DNA hybridization: Electrostatic model

FEDs are surface-charge measuring devices detecting the charge in a capacitive way. Since DNA molecules are polyanions with negative charges at their phosphate backbone, it can be expected that during the hybridization of ssDNA probe molecules with their complementary strands, the charge associated with the target molecule effectively changes the charge applied to the gate, resulting in a modulation of the flat-band voltage and capacitance of the EIS sensor. However, this scheme for electrostatic detection of charged macromolecules by their intrinsic molecular charge is only feasible if the sensor signal has not been interfered with any background interactions of the underlying gate surface such as ions in the solution (see Ch. 5). Moreover, the acid-base behavior and ion sensitivity of the gate surface, the surface-charge regulation effect, the density of the ssDNA layer, the length and orientation of DNA molecules, the length of linker molecules, the ionic strength (or screening length) of the solution as well as three-dimensional charge distribution in the intermolecular spaces in the immediate vicinity of the interface will play a critical role in transferring the hybridization-induced signal to the FED.

Modeling and simulation of DNA-FEDs are beneficial for a basic understanding of the DNA-hybridization detection mechanism as well as for technological predictions and optimization of these devices. Due to the high complexity of the DNA-FED system, theoretical models, which exactly describe the functioning taking into account all of the above mentioned interfering factors, do not exist so far. Therefore, recently several models describing the functioning of DNA-FEDs have been developed. For instance, an ion-concentration redistribution within the intermolecular spaces and alteration of the ion sensitivity of the gate surface upon DNA hybridization as possible mechanism for label-free detection of DNA has been discussed in [PogCh05]. To describe the sensitivity of field-effect transistors to DNA charge, the attached DNA layer has been modeled as an ion-permeable membrane with a neutral interior [LanAe05]. The relation between pH-, ion- and charge sensitivity of FEDs functionalized with charged biomolecules has been discussed in [Nef06]. More simplified models refer on the Grahame equation to calculate surface-potential changes due to the DNA hybridization by assuming that the whole charge associated with the target DNA is located at the gate-surface plane [InOf06, SakMiy05]. However, if the DNA molecules are tethered to the gate surface, the DNA charge is not confined directly to the interface, but it is distributed through some distance (dependent on the number of base pairs) away from the surface.

The electrostatic coupling between the DNA charge and gate surface as well as potential changes at the gate-electrolyte interface and the sensor signal induced upon the DNA hybridization will strongly drop with increasing the distance between the DNA molecules and the gate surface. Thus, in addition to the screening or Debye length (λ_D) the distance between the DNA charge and the sensor surface is one of the critical parameters that could strongly affect the expected sensor signal. In the following, a so-called "charge-plane" model for the simulation of gate-surface potential changes induced upon DNA hybridization is introduced. The model considers both the Debye length and middle distance of the DNA charge from the gate surface. A similar charge-plane model has been discussed to calculate surface-potential changes due to the binding of small peptides to a lipid monolayer [LuNi06].

The charge-plane model for the simulation of potential changes at the gate surface induced by the DNA hybridization or denaturation event and the schematic potential profile is illustrated in Figure 6.9.

The ssDNA and dsDNA molecules (with a density ρ_{DNA} and a length L) are assumed to be oriented normally to the sensor surface. Although the charges existing on each phosphate group in the DNA backbone are located at a different distance from the gate surface, the layer of charged ssDNA molecules is modeled as a plane (sheet) of uniformly distributed charges (with an effective charge density of σ_{ss}) located in the middle of the immobilized ssDNA layer at a distance of $x=L/2$ from the gate surface (the position of the gate surface is taken at $x=0$). This was done for the sake of simplicity in this study. The charges on both surfaces will create a diffuse layer in their vicinity. These diffuse layers will overlap for small distances between the gate surface and the charged plane.

In order to estimate the sensor signal that is induced upon the DNA-hybridization process, it was first approximated that the hybridization of the probe molecules with their complementary target molecules can be modeled by increasing the charge of the plane. Because the charge of the dsDNA (σ_{ds}) is nearly doubled, a new distribution of the electrostatic potential will be reached after hybridization.

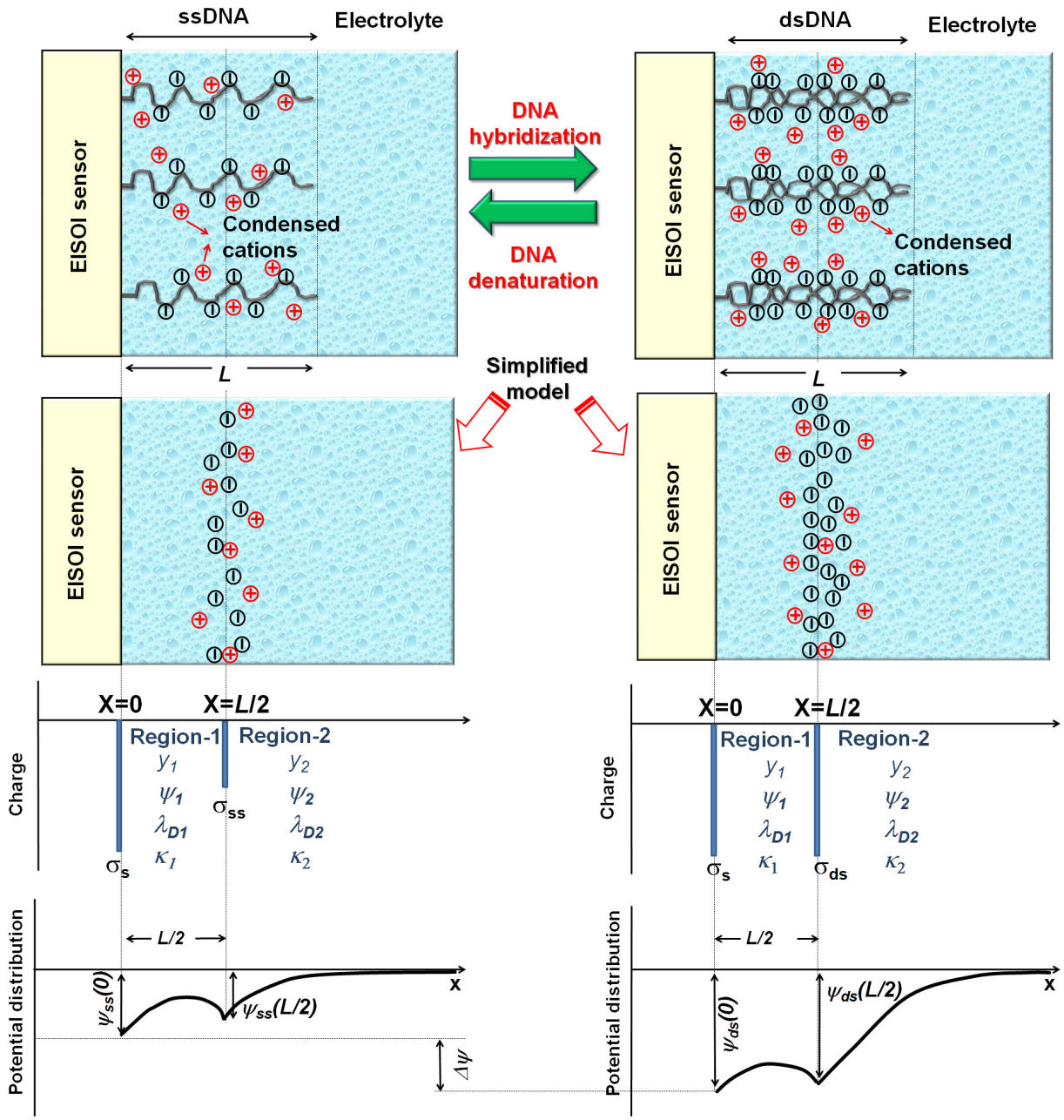

Fig. 6.9: The charge-plane model for the simulation of potential changes at the gate surface induced by DNA hybridization or denaturation event. The layer of charged ssDNA molecules is modeled as a plane (sheet) of uniformly distributed charges (with an effective charge density of σ_{ss}) located in the middle of the immobilized ssDNA layer at a distance of $x=L/2$ from the gate surface. The schematic potential profile between the negatively charged plane and the sensor surface after the DNA immobilization and hybridization is shown for a Debye length in electrolyte solution larger than the DNA length L.

Since the capacitive EISOI sensor operates in a constant-capacitance mode, the potential drop across the gate insulator is constant, so the changes in the flat-band voltage will be equal to the potential changes at the gate-electrolyte interface. Consequently, the response signal of the

EISOI sensor to intrinsic molecular charges (hybridization signal, $\Delta\psi$) can be calculated from the difference in the electrostatic potential at the gate surface after (ψ_{ds}) and before (ψ_{ss}) the DNA-hybridization process:

$$\Delta\psi = \psi_{ds}(x=0) - \psi_{ss}(x=0) \tag{6.2}$$

By assuming that the charge is uniform in the lateral direction, the one-dimensional Poisson-Boltzmann (PB) equation can be used to derive analytical expressions for the potential profile and changes in the gate-surface potential induced by the DNA hybridization or denaturation event. In the following, the potential distribution is calculated by assuming the linearized PB equation to be valid both in the space between the sensor surface and charged plane (region-1, $0 \le x \le L/2$) and in the outer electrolyte (region-2, $x \ge L/2$). The general solution of the linearized PB equation [Butt03, Isr92] is shown as:

$$\frac{d^2 y(x)}{dx^2} = \kappa^2 y(x) \tag{6.3}$$

For a dimensionless electrostatic potential $y = e_0\psi/(K_B T)$ in region-1 it can be described by two exponential functions [Che07a, Che08]:

$$y_1(x) = \alpha e^{\kappa_1 x} + \beta e^{-\kappa_1 x} \tag{6.4}$$

In region-2, where the potential has to decay to zero in the bulk electrolyte solution at large distances from the charged plane ($x \to \infty$), the general solution of the PB equation represents a single decaying exponential function:

$$y_2(x) = \gamma e^{-\kappa_2 (x - L/2)} \tag{6.5}$$

In Eq. 6.4 and Eq. 6.5, $\kappa_{1,2} = \lambda_{Dl,2}^{-1} = (2c_{1,2}e_0^{\,2}/\varepsilon K_B T)^{1/2}$, $c_{1,2}$, and ε are the reciprocal screening length, bulk electrolyte concentration and dielectric constant in region-1 and region-2, respectively. The integration constants α, β, γ are defined by the electrostatic boundary con-

ditions. These are given by the Gaussian law that relates to the derivative of the potential to the charge density on the sensor surface (σ_s) and the DNA sheet (σ). The third condition comes from the potential continuity across the charged plane. These boundary conditions are as follows:

$$\frac{d\psi_1}{dx} = -\frac{4\pi\sigma_s}{\varepsilon} > 0, \text{ at } x=0 \tag{6.6}$$

$$\frac{d\psi_2}{dx} = -\frac{4\pi\sigma/2}{\varepsilon} > 0, \text{ at } x=L/2 \tag{6.7}$$

$$\psi_1(L/2) = \psi_2(L/2) \tag{6.8}$$

From Eq. 6.4 - Eq. 6.8, the integration constants have been determined as:

$$\beta = \frac{4\pi l_B}{\kappa_2 e_0}.\frac{\frac{\sigma}{2}+\sigma_s\frac{\kappa_2}{\kappa_1}e^{\kappa_1 L/2}}{2\cosh[\kappa_1 L/2]}, \quad \alpha = \beta - \frac{4\pi l_B \sigma_s}{\kappa_1 e_0}, \text{ and } \quad \gamma = \frac{4\pi l_B \frac{\sigma}{2}}{\kappa_2 e_0}, \tag{6.9}$$

where $\sigma = \sigma_{ss}$ after ssDNA immobilization and $\sigma = \sigma_{ds}$ after DNA hybridization. It should be noted that in the linear PB approach, a doubling of the charge density of the DNA sheet in case of 100% hybridization efficiency will result in twice as high potentials on the charged plane after the hybridization, as compared to the ssDNA sheet.

For calculations of the change in the electrostatic potential ($\Delta\psi$) at the gate surface (at $x=0$) induced by the DNA-hybridization event and its comparison with the experimentally observed hybridization signal of the EISOI sensor, there is a need to define the effective charge density of immobilized ssDNA (σ_{ss}) and hybridized dsDNA (σ_{ds}). By assuming one negative charge on each phosphate group per base pair and considering the screening effect (fraction of DNA charge) by counter ions in the solution, the effective charge density of ssDNA and dsDNA can be calculated as follows:

$$\sigma_{ss} = e_0 n \rho_{DNA} (1-\delta) \tag{6.10}$$

$$\sigma_{ds} = \sigma_{ss} (1+\alpha) \tag{6.11}$$

where n is the number of base pairs (in this work, we use a thiol-modified, 20 base pair long ssDNA with L= 6.8 nm), $\rho_{DNA} = m.\rho_{Au-NP}$ is the density of the immobilized probe ssDNA molecules, m is the number of the immobilized ssDNA molecules per one Au-NP, ρ_{Au-NP} is the density of the deposited Au-NPs, α is the hybridization efficiency (by 100% hybridization, α=1 and $\sigma_{ds} = 2\sigma_{ss}$), and δ is the fraction of DNA charge screened or neutralized by cations. It should be noted, that according to Manning's counter-ion condensation theory (see e.g., [Mann78, Mann01]), monovalent cations could reduce the effective DNA charge by ~75% (i.e., δ~0.75), which will significantly reduce the expected hybridization signal.

Figure 6.10 shows different electrostatic potential profiles between the negatively charged plane and the sensor surface after the DNA immobilization and hybridization simulated by different Debye screening lengths in the region-1 of λ_{D1}=2, 5, and 21 nm (assuming different ion concentration in region-1) using Eq.6.4, E.q. 6.5 and Eq. 6.9- Eq. 6. 11. The simulation parameters are: ρ_{Au-NP} =1.2×10^{16} Au-NPs/m^2 (see Ch. 6.1), L/2=3.4 nm, n=20, m=1 (one immobilized ssDNA per Au-NP), ε=80 for both regions, $\alpha = 1$, $\delta = 0.75$, σ_{ss}= 6×10^{16} e_0 / m^2, σ_{ds}= 12×10^{16} e_0 / m^2, σ_s=2.4×10^{16} e_0 / m^2, and λ_2 =21 nm (this value of the Debye length in region-2 corresponds to an electrolyte concentration of 0.2 mM used in this work for the measurement of the DNA hybridization and denaturation signal).

The calculated potential changes at the gate surface (at x=0) induced by the DNA-hybridization event were $\Delta\psi$ =52, 116 and 143 mV for λ_{D1}=2, 5 and 21 nm, respectively. As expected, the lowering of the ionic strength (or increasing λ_{D1}) inside the DNA lattice (region-1) results in a higher hybridization signal. The calculated value of $\Delta\psi$ =116 mV for λ_{D1}=5 nm is close to the experimentally observed hybridization signal (~120 mV) of the EISOI sensor.

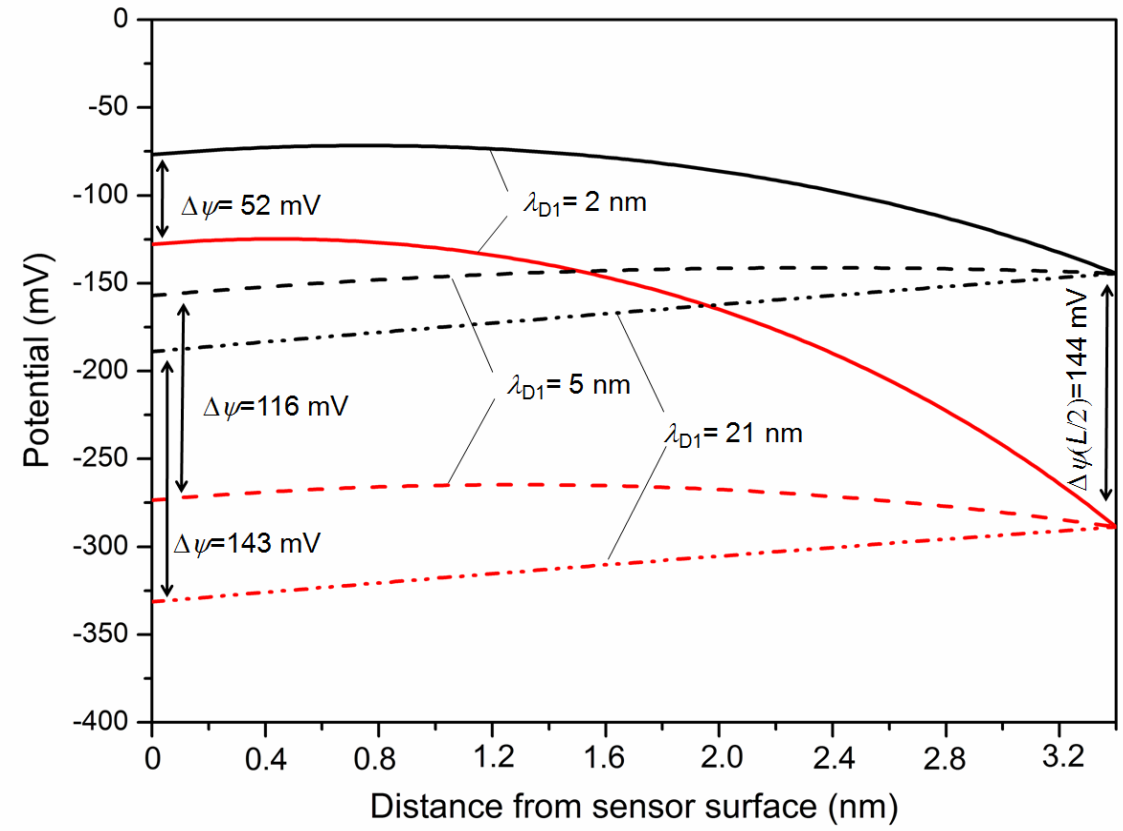

Fig. 6.10: Electrostatic potential profiles between the negatively charged plane and the sensor surface after the DNA immobilization and hybridization simulated by different Debye screening lengths in the region-1 of λ_{D1}=2, 5, and 21 nm. The screening length in region-2 was taken to be λ_{D2}=21 nm that corresponds to an electrolyte concentration of 0.2 mM used in this work for the measurement of the DNA hybridization and denaturation signal.

Nevertheless, there exist several unknown parameters as well as physical "complications" for a quantitative comparison of the potential changes predicted by the model when compared to the experimentally observed results:

- the unknown orientation of the DNA molecules to the sensor surface;
- the number of immobilized DNA molecules per Au-NP can be higher than m=1 as assumed in the model. Geometrically, the upper hemi-sphere of the Au-NP with an average size of 5-6 nm is potentially accessible for 3-4 dsDNA molecules with a diameter of 2 nm and a 4 nm separation between the DNA axis. According to recent experiments [PriTa10], short DNA fragments can be deposited at even higher densities on larger Au-NPs, with only ~3 nm distance between the neighboring DNA strands;

- the dielectric constant within the DNA lattice (region-1) can be significantly lower (e.g., ε=2-10 has been reported [Che07b] for a DNA interior) than inside the electrolyte solution in region-2 (ε~80);
- in the linear PB approach used in the presented model, it has been assumed that a doubling of the charge of the DNA sheet after hybridization will result in a twice as high potential on the charged plane. The linear PB equation is known to be valid for low potentials of ψ <25 mV [Isr92] (in most applications up to 50-80 mV [Butt03]). In a non-linear approach however, a much smaller surface potential of the charged sheet can be expected in comparison to the linear PB approach with the same surface-charge density [Isr92, Butt03]. Due to the non-linear dependence of the surface potential on the surface charge via the Grahame equation [Isr92, Butt03], doubling the charge of the DNA sheet upon DNA hybridization will result only in a moderate increase in the surface potential of the sheet. The expected potential change at the sensor surface and the hybridization signal could be, therefore, smaller than calculated (by the linearized PB equation).

In summary, a fabricated field-effect nanoplate EISOI sensor array was used for label-free electrical detection of DNA hybridization and denaturation. The ssDNA probe molecules were immobilized on the functionalized sensor surface by means of Au-NPs. To achieve high hybridization efficiency, the DNA hybridization was performed in a high ionic-strength solution. In order to reduce the screening of the DNA charge by counter ions in the electrolyte and to minimize the effect of disturbing factors, the signal changes induced by the hybridization and denaturation processes were read out in a low-ionic strength solution using a differential mode setup. In addition, the DNA immobilization, hybridization and denaturation were verified by fluorescence microscopy. For the simulation of the change of potential at the sensor surface induced by DNA hybridization, an electrostatic charge-plane model was developed taking into account both the Debye length and the distance of the DNA charge from the gate surface.

Chapter 7

7 Conclusions and outlook

In this thesis, field-effect-based capacitive EIS structures have been employed to detect the formation of “planar”- and “brush”-like molecular layers. Polyelectrolyte multilayers have been used as a model system to study the effects induced in capacitive EIS sensors via formation of a planar-like molecular layer [AbPog09, AbPog10, PogAb06, PogAb07, PogAb08, PogIn07, SchgAb09]. An electrostatic model based on the one-dimensional linear PB equation has been developed, which demonstrates the change of the EIS sensor’s surface charge upon the build-up of the PEM. In this model, the PEM interior is assumed as an electrically neutral environment with a very low ion concentration (~1 mM). Using this model, the change of the surface potential via the PEM formation in electrolytes with different ion concentrations has been simulated taking into account the Debye screening length inside the PEM. The simulations show that the change of the sensor-surface potential is a function of the distance between the charged layer and the sensor surface, charge density of the molecular layer, ionic strength in the PEM interior and in the bulk electrolyte. For experiments, the PEMs’ build-up on the sensor surface was achieved using the LbL technique, via consecutive adsorption of PAH and PSS. The formation of the PEM has been studied using physical characterization methods. After adsorption of each PE layer (increasing the layer number), a raise of the PEM thickness as well as surface roughness and hydrophilicity have been observed. Electrochemical monitoring of the PEM formation using an EIS sensor has been done by *C-V,* ConCap and IS measuring methods. The adsorption of each PE layer leads to an alternating shift of the sensor signal. Incidentally, the direction of this shift depends on the sign of the charge of the outermost (terminating) PE layer, resulting in a kind of “zigzag” curve of the signal changes as a function of the PEM number. The adsorption of PAH shifts the sensor sig-

nal towards the direction as for an additional positive charging of the SiO_2 surface that will increase the surface potential. Consequently, the direction of the potential changes after adsorption of negatively charged PSS corresponds to the case as if the SiO_2 surface would have been additionally negatively charged. This indicates that the molecular layer may also induce an interfacial potential change resulting in a change in the flat-band voltage of the EIS structure. Moreover, the potential shifts have the tendency to decrease with the increasing number of PE layers [AbPog09, AbPog10, PogAb06, PogAb07, PogAb08, PogIn07, SchgAb09]. The amplitude of the sensor signal is strongly dependent on the ion concentration of the applied electrolyte. All these observations are in good qualitative agreement with those predicted from the introduced model. Theoretically and experimentally, it is shown that the thickness of the PEM with maximum layer number and its charge can that be detected by FEDs is equal to the Debye length inside the PEM. In this way, the concentration in the PEM interior or dielectric constant of the PEM can be estimated.

The question arises, “Is the change of the sensor-surface potential (resulting in a shift of the sensor-output signal) caused by the intrinsic charge of the adsorbed or bounded macromolecules on the sensor surface, or is there other factors, which could affect the sensor signal, like the ion-concentration redistribution in the intermolecular spaces?”

To answer this question, the investigation of the PEM build-up using EIS sensors has been done in both buffered and unbuffered solutions with the same salt concentration. It has been observed that the potential shifts are much more smaller for the PEMs prepared in pH-buffer solution and decay much more rapidly with the number of adsorbed layers, as compared to PEMs formed in unbuffered solutions. It can be suggested that the local electric field emerged from the outermost PE layer redistributes protons (ions) in the PEMs, which in turn can change the local pH values on the SiO_2 surface and nearby the PAH layers. As the underlying SiO_2 gate-insulator surface is a pH-sensitive material, the redistribution of protons and alternating pH profiles inside the PEMs upon PAH/PSS adsorption can be detected with the underlying pH-sensitive field-effect transducer. Thus, larger signals were observed for EIS sensors with PE layers adsorbed from unbuffered solution. To prove the proton and ion permeability of the PEM, the pH- and sodium-ion sensitivity of EIS sensors covered with PEMs with a different layer number have been measured [SchgAb09]. The pH sensitivity of modified EIS sensors that is slightly dependent on the type of terminating PE layer as well as on the number of adsorbed layers is tested. This fact is a direct indication that the PEMs exhibit a high permeability for protons. Therefore, pH changes in the surrounding electrolyte will change the local pH within the PEM that will be directly detected by the underlying SiO_2 layer. The high

permeability of PEMs for protons as compared to other ions has been discussed in [Nef06] and explained by the Grotthuss-like mechanism of delocalized protons inside the PE films. In summary, it seems that both the intrinsic PE molecular charge and ion-concentration redistribution in PEMs contribute to the detected sensor signal. Probably for PE adsorption from unbuffered solutions, the sensor signal is largely induced by the redistribution of ions inside the PEM structure. For PE adsorption from buffered solution, on the other hand, the local pH changes in PEMs are suppressed and the signals detected are dominated by the direct electrostatic influence of the intrinsic charge of the adsorbed PE chains [SchgAb09].

The PE layers have been used in this work not only as a model system to study the planar-like formation of molecular layers but also for the preparation of EnFED-based biosensors with enhanced characteristics (using the permeability of the PE layer and pH-stimuli responsive behavior of the PAH) by functionalization of capacitive field-effect EIS structures with an LbL-assembled weak polyelectrolyte/penicillinase multilayer for penicillin sensing. The realized penicillinase/PAH-based biosensors respond to changes in both the local pH value near the gate surface and charges of the polyelectrolyte macromolecules induced via enzymatic reaction, resulting in a higher sensitivity. In addition, the embedment of enzymes in a multilayer prepared by LbL technique provides a larger amount of enzymes immobilized per sensor area, reduces the enzyme-leaching effect and thus, enhances the stability and life-time of the biosensor. Even after two months, the recorded sensor output-voltage directly correlates with the respective penicillin concentration with a low detection limit of about 20 µM. The realized penicillinase/PAH-based biosensor using LbL technique possesses a better biosensor characteristic than prepared penicillinase-based biosensors using the adsorptive method. The proposed novel strategy might be extended to further enzyme-based field-effect biosensors [AbPog10].

Furthermore, the realized field-effect nanoplate EISOI sensor array [AbMor11, AbIn09a, AbIn09b] modified with Au-NPs was successfully tested for a differential mode label-free electrical detection of DNA hybridization and denaturation events [AbPog11b, AbPog11a, AbPed10]. The differential setup provides a precise measurement by minimizing the disturbing factors (e.g., temperature, pH of ion concentration change, drift of the sensor) during measurements. The ssDNA probe molecules were immobilized on the surface of Au-NPs. The DNA hybridization was performed in a high-ionic strength solution. In contrast, to reduce the screening of the DNA charge by counter ions and to achieve a high sensitivity, the signal changes induced by hybridization and denaturation were read out in a low-ionic strength solution using a differential-mode setup. In addition, the fluorescence-microscopy method has

been applied to verify the DNA immobilization, hybridization and denaturation events. High differential signals of about 120 mV and 90 mV were registered after the DNA-hybridization and denaturation events, respectively. Moreover, an electrostatic charge-plane model for the simulation of potential changes at the gate surface induced by the DNA-hybridization event has been developed taking into account both the Debye length and the distance of the DNA charge from the gate surface. Potential profiles between the negatively charged DNA sheet as well as potential changes at the gate surface induced by the hybridization event has been simulated by different Debye screening lengths using the linearized PB equation [AbPog11b].

Outlook

Future work could be focused on:

a) the future miniaturization of capacitive EISOI sensors and increasing the number of sensors in the array, as well as the improvement of the sensors' geometry and design;

b) using single-stranded morpholinos instead of ssDNAs as recognition elements for the realization of DNA sensors. The morpholinos are not charged in the electrolyte and the hybridization of perfectly-matched morpholinos with probe DNAs can be also take place in low-concentrated salt solutions. This feature of morpholino-DNA hybridization condition will offer the direct on-line monitoring of the hybridization event;

c) the development of EISOI sensor arrays for the detection of single nucleotide polymorphisms, proteins, antibodies and other charged macromolecules;

d) using the EISOI sensor array for simultaneous multi-parameter (bio-)chemical sensing.

Literature

[Abd06] Abdelghani, A.; Cherif, K.; Jaffrezic-Renault, N.; Matejec, V., Impedance spectroscopy on xerogel layer for chemical sensing, Mat. Sci. Eng. C 26 (2006) 542-545.

[AbIn09a] Abouzar, M.H.; Ingebrandt, S.; Poghossian, A.; Zhang, Y.; Vu. X.T.; Moritz, W.; Schöning, M.J., Nanoplate field-effect capacitive (bio-)chemical sensor array based on SOI structure, Procedia Chemistry 1 (2009) 670-673.

[AbIn09b] Abouzar, M.H.; Ingebrandt, S.; Poghossian, A.; Zhang, Y.; Moritz, W.; Schöning, M.J., Field-effect nanoplate capacitive pH sensor based on SOI structure, Proc. of 7th Int. Conf. on Semiconductor Micro- and Nanoelectronics (2009) 53-56.

[AbMor11] Abouzar, M.H.; Moritz, W.; Schöning, M.J.; Poghossian, A., Capacitance-voltage and impedance-spectroscopy characteristics of nanoplate EISOI capacitors, Phys. Stat. Solidi A (2011) accepted.

[AbPed10] Abouzar, M.H.; Pedraza, A.M.; Schöning, M.J.; Poghossian, A., Label-free DNA hybridization and denaturation detection by means of field-effect nanoplate SOI capacitors functionalized with gold nanoparticles, Procedia Engineering 5 (2010) 918-921.

[AbPog08a] Abouzar, M.H.; Poghossian, A.; Christiaens, P.; Williams, O.A.; Haenen, K.; Wagner, P.; Schöning, M.J., Feldeffektsensor auf nanokristalliner Diamantbasis, VDI-Berichte 2011 (2008) 549-558.

[AbPog08b] Abouzar, M.H.; Poghossian, A.; Razavi, A.; Besmehn, A.; Bijnens, N.; Williams, O.A.; Haenen, K.; Wagner, P.; Schöning, M.J., Penicillin detection with nanocrystalline-diamond field-effect sensor, Phys. Stat. Solidi A 205 (2008) 2141-2145.

[AbPog09] Abouzar, M.H.; Poghossian, A.; Razavi, A.; Williams, O.A.; Bijnens, N.; Wagner, P.; Schöning, M.J., Characterisation of capacitive field-effect sensors with a nanocrystalline-diamond film as transducer material for multi-parameter sensing, Biosens. Bioelectron. 24 (2009) 1298-1304.

[AbPog10] Abouzar, M.H.; Poghossian, A.; Siqueira, Jr.J.R.; Oliveira, Jr.N.O.; Moritz, W.; Schöning, M.J., Capacitive electrolyte-insulator-semiconductor structures functionalised with a polyelectrolyte/enzyme multilayer: New strategy for enhanced field-effect biosensing, Phys. Stat. Solidi A 207 (2010) 884-890.

[AbPog11a] Abouzar, M.H.; Poghossian, A.; Pedraza, A.M.; Ingebrandt, S.; Moritz, W.; Schöning, M.J., (Bio-)chemical sensor array based on nanoplate SOI capacitors, Biosens. Bioelectron. 26 (2011) 3023-3028.

[AbPog11b] Abouzar, M.H.; Poghossian, A.; Pedraza, A.M.; Cherstvy, A.G.; Schöning, M.J., Label-free DNA hybridization and denaturation detection by means of field-effect nanoplate SOI capacitors functionalized with gold nanoparticles, Phys. Stat. Solidi A (2011) submitted.

[Bar05] Barhoumi, H.; Maaref, A.; Mlika, R.; Martelet, C.; Jaffrezic-Renault, N.; Ponsonnet, L., EIS field-effect structures functionalised by p-tertbutylcalix[6]arene, Mat. Sci. Eng. C 25 (2005) 61-66.

[BarJo96] Barrat, J.L.; Joanny, J.F., Theory of polyelectrolyte solutions, Adv. Chem. Phys. 94 (1996) 1-66.

[Ben06] Ben Ali, M.; Korpan, Y.; Gonchar, M.; El'skaya, A.; Maaref, M.A.; Jaffrezic-Renault, N.; Martelet, C, Formaldehyde assay by capacitance versus voltage and impedance measurements using bi-layer bio-recognition membrane, Biosens. Bioelectron. 22 (2006) 575-581.

[Berg91] Bergveld, P., A critical evaluation of direct electrical protein detection methods, Biosens. Bioelectron. 6 (1991) 55-72.

[Berg03] Bergveld, P., Thirty years of ISFETOLOGY: What happened in the past 30 years and what may happen in the next 30 years, Sens. Actuators B 88 (2003) 1-20.

[BergSib88] Bergveld P.; Sibbald, A., Analytical and Biomedical Applications of Ion-Selective Field-Effect Transistors, Elsevier, Amsterdam, 1988.

[Blac87] Blackburn, G.F., in "Biosensors: Fundamentals and Applications", Oxford University Press, Oxford, 1987.

[Bod03] Bodrossy, L.; Stralis-Pavese, N.; Murrell, J.C.; Radajewski, S.; Weilharter, A.; Sessitsch, A., Development and validation of a diagnostic microbial microarray for methanotrophs, Environ. Microbiol. 5 (2003) 566-582.

[Bos04] Bosio, V.; Dubreuil, F.; Bogdanovic, G.; Fery, A., Interactions between silica surfaces coated by polyelectrolyte multilayers in aqueous environment: Comparison between precursor and multilayer regime, Colloids Surf. A Physicochem. Eng. Asp. 243 (2004) 147-155.

[Bous83] Bousse, L.J.; de Rooij, N.F.; Bergveld, P., Operation of chemically sensitive field-effect sensors as a function of the insulator-electrolyte interface, IEEE Trans. Electron. Dev. ED-30 (1983) 1263-1270.

[BousB83] Bousse, L.; Bergveld, P., On the impedance of the silicon dioxide/electrolyte interface, J. Electroanal. Chem. 152 (1983) 25-39.

[Butt03] Butt, H.-J.; Graf, K.; Kappl, M., Physics and Chemistry of Interfaces, Wiley-VCH, Berlin, 2003.

[CarJan80] Caras, S.; Janata, J., Field effect transistor sensitive to penicillin, Anal. Chem. 52 (1980) 1935-1937.

[CarNi97] Caruso, F.; Niikura, K.; Furlong, D.N.; Okahata, Y., Ultrathin multilayer polyelectrolyte films on gold: Construction and thickness determination, Langmuir 13 (1997) 3422-3426.

[Carr04] Carrière, D.; Krastev, R.; Schönhoff, M., Oscillations in solvent fraction of polyelectrolyte multilayers driven by the charge of the terminating layer, Langmuir 20 (2004) 11465-11472.

[Che07a] Cherstvy, A.G., Electrostatic of DNA complexes with cationic lipids, J. Phys. Chem. B 111 (2007) 7914-7927.

[Che07b] Cherstvy, A.G., Effect of low-dielectric interior on DNA response to twisting and bending, J. Phys. Chem. B 111 (2007) 12933-12937.

[Che08] Cherstvy, A.G., DNA cholesteric phases: the role of DNA molecular chirality and DNA-DNA electrostatic interactions, J. Phys. Chem. B 112 (2008) 12585-12595.

[ChoSt99] Chodanowski, P.; Stoll, S., Monte Carlo simulations of hydrophobic polyelectrolytes: Evidence of complex configurational transitions, J. Chem. Phys. 111 (1999) 6069-6081.

[ClaLy62] Clark, L.C.; Lyons, C., Electrode system for continuous monitoring in cardiovascular surgery, Ann. N.Y. Acad. Sci. 148 (1962) 133-153.

[Cobb70] Cobbold, R.S.C., Theory and Applications of Field-Effect Transistors, Wiley, New York, 1970.

[Curr08] Curreli, M.; Zhang, R.; Ishikawa, F.; Chang, H.; Cote, R.; Zhou, C., Real-time label-free detection of biological entities using nanowire-based FETs, IEEE Trans. Nanotechnol. 7 (2008) 651-667.

[DaJen01] Dai, J.H.; Jensen, A.W.; Mohanty, D.K.; Erndt, J.; Bruening, M.L., Controlling the permeability of multilayered polyelectrolyte films through derivatization, cross-linking and hydrolysis, Langmuir 17 (2001) 931-937.

[Dech92] Decher, G.; Hong, J.D.; Schmitt, J., Build-up of ultrathin multilayer films by a self-assembly process. 3. Consecutively alternating adsorption of anionic and cationic polyelectrolytes on charged surfaces, Thin Sol. Films 210 (1992) 831-835.

[Dech97] Decher, G., Fuzzy nanoassemblies: Toward layered polymeric multicomposites, Science 277 (1997) 1232-1237.

[DechEc98] Decher, G.; Eckle, M.; Schmitt, J.; Struth, B., Layer-by-Iayer assembled multicomposite films, Curr. Opin. Colloid Interface Sci. 3 (1998) 32-39.

[DechSlf03] Decher, G.; Schlenoff, J., Multilayer Thin Films: Sequential Assembly of Nanocomposite Materials, Wiley-VCH, Weinheim, 2003.

[Diot85] Diot, L.; Joseph, J.; Martin, J.R.; Clechet, P., pH dependence of the Si/SiO_2 interface state density for EOS systems, J. Electroanal. Chem. 193 (1985) 75-88.

[Dem95] Demoz, A.; Verpoorte, E.M.J.; Harrison, D.J., An equivalent circuit model for ion-selective membrane/insulator/semiconductor interfaces used for chemical sensors, J. Electroanal. Chem. 389 (1995) 71-78.

[DemCa08] Demirel, G.; Çağlayan, M.O.; Garipcan, B.; Pişkin, E., A novel DNA biosensor based on ellipsometry, Surf. Sci. 602 (2008) 952-959.

[Dob96] Dobrynin, A.V.; Rubinstein, M.; Obukhov, S.P., Cascade of transitions of polyelectrolytes in poor solvents, Macromolecules 29 (1996) 2974-2979.

[Dong08] Lee, D.-Y.; Choi, W.-S.; Kafi, A.K.M.; Park, S.-H.; Kwon, Y.-S., Immobilization, hybridization and amperometric detection of DNA sensor using quartz crystal microbalance, J. Nanosci. Nanotechnol. 8 (2008) 4553-4556.

[DzySol06] Dzyadevych, S.V.; Soldatkin, A.P.; El'skaya, A.V.; Martelet, C.; Jaffrezic-Renault N., Enzyme biosensors based on ion-selective field-effect transistors, Anal. Chim. Acta 568 (2006) 248-258.

[Est96] Estrada del Cueto, M.; Altuzarra, A.C., On the analysis of C-V curves for high resistivity substrates, Solid-State Electron. 9 (1996) 1519-1521.

[EtPi04] Etienne, O.; Picart, C.; Taddei, C.; Haike, J.Y.; Dimarcq, L.; Schaaf, P.; Voegel, J.C.; Ogier, J.A.; Egles, C., Multilayer polyelectrolyte films functionalized by insertion of defensin: A new approach to protection of implants from bacterial colonization, Antimicrob. Agents Chemother. 10 (2004) 3662-3669.

[FaLa90] Fabry, P.; Laurent-Yvonnou, L., The C-V method for characterizing ISFET or EOS devices with ion-sensitive membranes, J. Electroanal. Chem. 286 (1990) 23-40.

[FrCo02] Fritz, J.; Cooper, E.B.; Gaudet, S.; Sorger, P.K.; Manalis S.R., Electronic detection of DNA by its intrinsic molecular charge, Proc. Natl. Acad. Sci. 99 (2002) 14142-14146.

[GaCha00] Gavalas, V.G.; Chaniotakis, N.A., Polyelectrolyte stabilized oxidase based biosensors: effect of diethylaminoethyl-dextran on the stabilization of glucose and lactate oxidases into porous conductive carbon, Anal. Chim. Acta 404 (2000) 67-73.

[Glin07] Glinel, K.; De´jugnat, C.; Prevot, M.; Schöler, B.; Schönhoff, M.; Klitzing, R.v., Responsive polyelectrolyte multilayers, Colloids Surf. A 303 (2007) 3-13.

[Grah47] Grahame, D.C., The electrical double layer and the theory of electrocapillarity, Chem. Rev. 41 (1947) 441-501.

[Grat98] Grattarola, M.; Massobrio, G., Bioelectronics Handbook: MOSFETs, Biosensors and Neurons, McGraw-Hill, New York, 1998.

[GuAb08] Gun, J.; Schöning, M.J.; Abouzar, M.H.; Poghossian, A.; Katz, E., Field-effect nanoparticle-based glucose sensor on a chip: amplification effect of coimmobilized redox species, Electroanal. 20 (2008) 1748-1753.

[GuRi09] Gun, J.; Rizkov, D.; Lev, O.; Abouzar, M.H.; Poghossian, A.; Schöning, M.J., Oxygen plasma-treated gold nanoparticle-based field-effect devices as transducer structures for bio-chemical sensing, Microchim. Acta 164 (2009) 395-404.

[HäFi07] Hänni-Ciunel, K.; Findenegg, G.H.; Klitzing, R.v., Water contact angle on polyelectrolyte-coated surfaces: Effects of film swelling and droplet evaporation, Soft Materials 5 (2007) 61-73.

[Hal95] van Hal, R.E.G.; Eijkel, J.C.T.; Bergveld, P., A novel description of ISFET sensitivity with the buffer capacity and double-layer capacitance as key parameters, Sens. Actuators B 24-25 (1995) 201-205.

[Hal96] van Hal, R.E.G.; Eijkel, J.C.T.; Bergveld, P., A general model to describe the electrostatic potential at electrolyte oxide interfaces, Adv. Colloid Interface Sci. 69 (1996) 31-62.

[HaLi04] Hahm, J.; Lieber, C.M., Direct ultrasensitivie electrical detection of DNA and DNA sequence variations using nanowire nanosensors, Nano Lett. 4 (2004) 51-54.

[Ham00] Hammond, P.T., Recent explorations in electrostatic multilayer thin film assembly, Curr. Opin. Colloid Interface Sci. 4 (2000) 430-442.

[Han06] Han, Y., Label-free detection of biomolecules by a field-effect transistor microarray biosensor with bio-functionalized gate surfaces, PhD thesis, RWTH Aachen University, 2006.

[Heiz07] Heitzinger, C.; Klimeck, G., Computational aspects of the three dimensional feature-scale simulation of silicon-nanowire field-effect sensor for DNA detection, J. Comput. Electron. 6 (2007) 387-390.

[HiaGaj01] Hianik, T.; Gajdos, V.; Krivanek, R.; Oretskaya, T.; Metelev, V.; Volkov, E.; Vadgama, P., Amperometric detection of DNA hybridization on a gold surface depends on the orientation of oligonucleotide chains, Bioelectrochem. 53 (2001) 199-204.

[Hill06] Hillberg, A.L.; Tabrizian, M., Biorecognition through layer-by-layer polyelectrolyte assembly: In-situ hybridization on living cells, Biomacromolecules 7 (2006) 2742-2750.

[Hou06] Hou, Y.; Helali, S.; Zhang, A.; Jaffrezic-Renault, N.; Martelet, C.; Minic, J., Immobilisation of rhodopsin on a self-assembled multilayer and its specific detection by electrochemical impedance spectroscopy, Biosens. Bioelectron. 21 (2006) 1393-1402.

[InHan07] Ingebrandt, S.; Han, Y.; Nakamura, F.; Poghossian, A.; Schöning, M.J.; Offenhäusser, A., Label-free detection of single nucleotide polymorphisms utilizing the differential transfer function of field-effect transistors, Biosens. Bioelectron. 22 (2007) 2834-2840.

[InOf06] Ingebrandt, S.; Offenhäusser, A., Label-free detection of DNA using field-effect transistors, Phys. Stat. Solidi A 203 (2006) 3399-3411.

[Isr92] Israelachvili, J., Intermolecular and Surface Forces, Academic Press, New York, 1992.

[Jana85] Janata, J.; Huber, R.J., Solid State Chemical Sensors, Academic Press, Orlando, 1985.

[KafPän08] Kafka, J.; Pänke, O.; Abendroth, B.; Lisdat, F., A label-free DNA sensor based on impedance spectroscopy, Electrochim. Acta 53 (2008) 7467-7474.

[KalCan10] Kalantari, R.; Cantor, R.; Chen, H.; Yu, G.; Janata, J.; Josowicz, M., Label-free voltammetric detection using individually addressable oligonucleotide microelectrode arrays, Anal. Chem. 82 (2010) 9028-9033.

[KhaSuk03] Kharlampieva, E.; Sukhishvili, S.A., Polyelectrolyte multilayers of weak polyacid and cationic copolymer: Competition of hydrogen-bonding and electrostatic interactions, Macromolecules 36 (2003) 9950-9956.

[Kli95] Klitzing, R.v.; Möhwald, H., Proton concentration profile in ultrathin polyelectrolyte films, Langmuir 11 (1995) 3554-3559.

[Kli06] Klitzing, R.v., Internal structure of polyelectrolyte multilayer assemblies, Phys. Chem. Chem. Phys. 8 (2006) 5012-5033.

[KraMor06] Krause, S.; Moritz, W.; Talabani, H.; Xu, M.; Sabot, A.; Ensell, G., Scanning Photo-induced Impedance Microscopy - Resolution studies and polymer characterization, Electrochim. Acta 51 (2006) 1423-1430.

[Kras00] Krasemann, L.; Tieke, B., Selective ion transport across self-assembled alternating multilayers of cationic and anionic polyelectrolytes, Langmuir 16 (2000) 287-290.

[LanAe05] Landheer, D.; Aers, G.; McKinnon, W.R.; Deen, M.J.; Ranuarez, J.C., Model for the field effect from layers of biological macromolecules on the gates of metal-oxide-semiconductor transistors, J. Appl. Phys. 98 (2005) 044701-044701-15.

[LiCh08] Liang, X.G.; Chou, S.Y., Nanogap detector inside nanofluidic channel for fast real-time label-free DNA analysis, Nano Lett. 8 (2008) 1472-1476.

[LoSch05] Loy, A.; Schulz, C.; Lucker, S.; Schopfer-Wendels, A.; Stoecker, K.; Baranyi, C.; Lehner, A.; Wagner, M., 16S rRNA gene-based oligonucleotide microarray for environmental monitoring of betaproteobacterial order " Rhodocyclales", Applied and Environ. Microbiol. 71 (2005) 1373-1386.

[Lun06] Luna-Lopez, J.A.; Aceves-Mijares, M.; Malik, O.; Glaenzer, R., Modelling the C-V characteristics of MOS capacitor on high resistivity silicon substrate for PIN photodetector applications, Revista Mexicana de Física 52 (2006) 45-47.

[Lund91] Lundström, I.; van den Berg, A.; van der Schoot, B.H.; van den Vlekkert, H.H.; Armgarth, M.; Nylander, C.I., Sensors: A Comprehensive Survey, Wiley, Weinheim, 1991.

[LuNi06] Lud, S.Q.; Nikolaides, M.G.; Haase, I.; Fischer, M.; Bausch, A.R., Field effect of screened charges: Electrical detection of peptides and proteins by a thin-film resistor, ChemPhysChem 7 (2006) 379-384.

[Mac87] Macdonald, J.R., Impedance spectroscopy, John Wiley & Sons, New York, 1987.

[Mado89] Madou, M.J.; Morrison, S.R., Chemical Sensing with Solid State Devices, Academic Press, San Diego, 1989.

[Mann01] Manning, G.S., Counterion condensation on a helical charge lattice, Macromolecules 34 (2001) 4650-4655.

[Mann78] Manning, G.S., The molecular theory of polyelectrolyte solution with applications to the properties of polynucleotides, Q. Rev. Biophys. II (1978) 179-246.

[MaWin09] Mansouri, S.; Winnik, F.M.; Tabrizian, M., Modulating the release kinetics through the control of the permeability of the LbL assembly: A review, Expert Opin. Drug Discovery 6 (2009) 585-597.

[MarTse09] Martnez, M.T.; Tseng, Y.-C.; Ormategui, N.; Loinaz, I.; Eritja, R.; Bokor, J., Label-free DNA biosensors based on functionalized carbon nanotube field effect transistors, Nano Lett. 9 (2009) 530-536.

[Maus04] Mauser, T.; De´jugnat, C.; Sukhorukov, G.B., Reversible pH-dependent properties of multilayer microcapsules made of weak polyelectrolytes, Macromol. Rapid Commun. 25 (2004) 1781-1785.

[Maxa77] Maxam, A.M.; Gilbert, W., A new method for sequencing DNA, Proc. Nat. Acad. Sci. 74 (1977) 560-564.

[MeJac03] Menchaca, J.L.; Jachimska, B.; Cuisinier, F.; Pérez, E., In situ surface structure study of polyelectrolyte multilayers by liquid-cell AFM, Colloids Surf. A 222 (2003) 185-194.

[Mic99] Micka, U.; Holm, C.; Kremer, K., Strongly charged, flexible polyelectrolytes in poor solvents: Molecular dynamics simulations, Langmuir 15 (1999) 4033-4044.

[MoMa03] Mourzina, Yu.; Mai, Th.; Poghossian, A.; Ermelenko, Yu.; Yoshinobu, T.; Vlasov, Yu.; Iwasaki, H.; Schöning, M.J., K^+-selective field-effect sensors as transducers for bioelectronic applications, Electrochim. Acta 48 (2003) 3333-3339.

[Nef06] Neff, P.A., Synthetic and biological polyelectrolytes: detection and characterisation by a silicon-on-insulator based thin film resistor, PhD thesis, Technical University Munich, 2006.

[NefNa06] Neff, P.A.; Naji, A.; Ecker, C.; Nickel, B.; Klitzing, R.v.; Bausch, A.R., Electrical detection of self-assembled polyelectrolyte multilayers by a thin film resistor, Macromolecules 39 (2006) 463-466.

[NefWu06] Neff, P.A.; Wunderlich, B.K.; Lud, S.Q.; Bausch, A.R., Silicon-on-insulator based thin film resistors for quantitative biosensing applications, Phys. Stat. Solidi (a) 14 (2006) 3417-3423.

[NefWu07a] Neff, P.; Serr, A.; Wunderlich, B.K.; Bausch, A.R., Label-free electrical determination of trypsin activity by a silicon-on-insulator based thin film resistor, ChemPhysChem. 8 (2007) 2133-2137.

[NefWu07b] Neff, P.A.; Wunderlich, B.K.; Klitzing, R.v.; Bausch, A.R., Formation and dielectric properties of polyelectrolyte multilayers studied by a silicon-on-insulator based thin film resistor, Langmuir 23 (2007) 4048-4052.

[Nico82] Nicollian, E.H.; Brews, J.R., MOS (Metal Oxide Semiconductor) Physics and Technology, Wiley, New York, 1982.

[PaLi07] Park, I.Y.; Li, Z.Y.; Li, X.M.; Pisano, A.P.; Williams R.S., Towards the silicon nanowire-based sensor for intracellular biochemical detection, Biosens. Bioelectron. 22 (2007) 2065-2070.

[Park03] Park, S.M.; Yoo, J.S., Electrochemical impedance spectroscopy for better electrochemical measurements, Anal. Chem. 75 (2003) 455A-461A.

[PaTi07] Patolsky, F.; Timko, B.P.; Zheng, G.F.; Lieber, C.M., Nanowirebased nanoelectronic devices in the life sciences, MRS Bull. 32 (2007) 142-149.

[Petr03] Petrov, A.I.; Antipov, A.A.; Sukhorukov, G.B., Base-acid equilibria in polyelectrolyte systems: From weak polvelectrolytes to interpolyelectrolyte complexes and multilayered polyelectrolyte shells, Macromolecules 36 (2003) 10079-10086.

[Pirr02] Pirrug, M.C., How to make a DNA chip, Angew. Chem. Int. Ed. 41 (2002) 1276-1289.

[PogAb06] Poghossian, A.; Abouzar, M.H.; Sakkari, M.; Kassab, T.; Han, Y.; Ingebrandt, S.; Offenhäusser, A.; Schöning, M.J., Field-effect sensors for monitoring the layer-by-layer adsorption of charged macromolecules, Sens. Actuators B 118 (2006) 163-170.

[PogAb07] Poghossian, A.; Abouzar, M.H.; Amberger, F.; Mayer, D.; Han, Y.; Ingebrandt, S.; Offenhäusser, A.; Schöning, M.J., Field-effect sensors with charged macromolecules: Characterisation by capacitance-voltage, constant-capacitance, impedance spectroscopy and atomic-force microscopy methods, Biosens. Bioelectron. 22 (2007) 2100-2107.

[PogAb08] Poghossian, A.; Abouzar, M.H.; Schöning, M.J., Capacitance-voltage and impedance characteristics of field-effect EIS sensors functionalised with polyelectrolyte multilayers, ITBM-RBM 29 (2008) 149-154.

[PogCh05] Poghossian, A.; Cherstvy, A.; Ingebrandt, S.; Offenhäusser, A.; Schöning, M.J., Possibilities and limitations of label-free detection of DNA hybridization with field-effect-based devices, Sens. Actuators B 111 (2005) 470-480.

[PogIn07] Poghossian, A.; Ingebrandt, S.; Abouzar M.H.; Schöning M.J., Label-free detection of charged macromolecules by using a field-effect-based sensor platform: Experiments and possible mechanisms of signal generation, Appl. Phys. A 87 (2007) 517-524.

[PogMa04] Poghossian, A.; Mai, D-T.; Mourzina, Yu.; Schöning, M.J., Impedance effect of an ion-sensitive membrane: characterisation of an EMIS sensor by impedance spectroscopy, capacitance-voltage and constant-capacitance method, Sens. Actuators B 103 (2004) 423-428.

[PogSchg06] Poghossian, A.; Schöning, M.J., Silicon-based chemical and biological field-effect sensors, in: Encyclopedia of Sensors, 9 (2006) 463-733.

[PogTh01] Poghossian, A.; Thust, M.; Schroth, P.; Steffen, A.; Lüth, H.; Schöning, M.J., Penicillin detection by means of silicon-based field-effect structures, Sensor Matr. 13 (2001) 207-223.

[PriTa10] Prigodich, A.; Lee, O.S.; Daniel, W.L.; Seferos, D.S.; Schatz, G.C.; Mirkin C.A., Tailoring DNA structure to increase target hybridization kinetics on surfaces, J. Am. Chem. Soc. 132 (2010) 10638-10641.

[Rade01] Radeva, T., Physical Chemistry of Polyelectrolytes, Marcel Dekker, New York, 2001.

[Rieg02] Riegler, H.; Essler, F., Polyelectrolytes. 2. Intrinsic or extrinsic charge compensation Quantitative charge analysis of PAH/PSS multilayers, Langmuir 18 (2002) 6694-6698.

[Ron03] Rong, B.; Nanaver L.K.; Burghartz, J.N.; Jansman, A.B.M.; Evans, A.G.R.; Rejaei, B.S., C-V characterization of MOS capacitors on high resistivity silicon substrate, Proc. ESSDERC (2003).

[RyRh89] Rychlik, W.; Rhoads, R.E., A computer-program for choosing optimal oligonucleotides for filter hybridization, sequencing and in-vitro amplification of DNA, Nucleic Acids Res. 17 (1989) 8543-8551.

[SakMiy05] Sakata, T.; Miyahara, Y., Detection of DNA recognition events using multi-well field effect devices, Biosens. Bioelectron. 21 (2005) 827-832.

[Sang77] Sanger, F.; Nicklen, S.; Coulson, A.R., DNA sequencing with chainterminating inhibitors, Proc. Nat. Acad. Sci. 74 (1977) 5463-5467.

[Schf03a] Schonhoff, M., Layered polyelectrolyte complexes: Physics of formation and molecular properties, J. Phys. Condens. Matter 15 (2003) R1781-R1808.

[Schf03b] Schonhoff, M., Self-assembled polyelectrolyte multilayers, Curr. Opin. Colloid Interface Sci. 8 (2003) 86-95.

[Schf07] Schonhoff, M.; Ball, V.; Bausch, A.R.; Dejugnat, C.; Delorme, N.; Glinel, K.; Klitzing, R.v.; Steitz, R., Hydration and internal properties of polyelectrolyte multilayers, Colloids Surf. A 303 (2007) 14-29.

[SchgAb07a] Schöning, M.J.; Abouzar, M.H.; Poghossian, A.; Han, Y.; Offenhäusser, A.; Ingebrandt, S., Markierungsfreie DNA-Detektion mit Silizium-Feldeffekt-Sensoren – Messeffekte oder Artefakte?, Technisches Messen 9 (2007) 466-474.

[SchgAb07b] Schöning, M.J.; Abouzar, M.H.; Wagner, T.; Näther, N.; Rolka, D.; Yoshinobu, T.; Kloock, J.P.; Turek, M.; Ingebrandt, S.; Poghossian, A., A semiconductor-based field-effect platform for (bio-)chemical and physical sensors: From capacitive EIS sensors and LAPS over ISFETs to nano-scale devices, Material Res. Soc. Sympos. Proc. 952 (2007) paper 0952-F08-02, 1-9.

[SchgAb09] Schöning, M.J.; Abouzar, M.H.; Poghossian, A., pH and ion sensitivity of a field-effect EIS (electrolyte-insulator-semiconductor) sensor covered with polyelectrolyte layers, J. Solid State Electrochem. 13 (2009) 115-122.

[SchgBr05] Schöning, M.J.; Brinkmann, D.; Rolka, D.; Demuth, C., CIP (cleaning-in-place) suitable “non-glass” pH sensor based on a Ta_2O_5-gate EIS structure, Sens. Actuators B 111 (2005) 423-429.

[SchgPog06] Schöning, M.J.; Poghossian, A., Bio FEDs (Field-Effect Devices): State-of-the-art and new directions, Electroanal. 18 (2006) 1893-1900.

[Schr07] Schollmeyer, H.; Guenoun, P.; Daillant, J.; Novikov, D., Ion Distribution in Polyelectrolyte Multilayers with Standing-Wave X-ray Fluorescence, J. Phys. Chem. B 16 (2007) 4036-4042.

[ScSchf02] Schwarz, B.; Schönhoff, M., Surface potential driven swelling of polyelectrolyte multilayers, Langmuir 18 (2002) 2964-2966.

[ShRu00] Shiratori, S.S.; Rubner, M.F., pH-dependent thickness behavior of sequentially adsorbed layers of weak polyelectrolytes, Macromolecules, 33 (2000) 4213-4219.

[Sibb86] Sibbald, A., Recent advances in field effect chemical microsensors, J. Mol. Electron. 2 (1986) 51-83.

[SilLe91] Silberzan, P.; Leger, L.; Ausserre, D.; Benattar, J.J., Silanation of silica surfaces. A new method of constructing pure or mixed monolayers, Langmuir 7 (1991) 1647-1651.

[SiqAb09a] Siqueira, Jr.J.R.; Abouzar, M.H.; Poghossian, A.; Zucolotto, V.; Oliveira Jr.O.N.; Schöning, M.J., Penicillin biosensor based on a capacitive field-effect structure functionalized with a dendrimer/carbon nanotube multilayer, Biosens. Bioelectron. 25 (2009) 497-501.

[SiqAb09b] Siqueira, Jr.J.R.; Abouzar, M.H.; Bäcker, M.; Zucolotto, V.; Poghossian, A.; Oliveira, Jr.O.N.; Schöning, M.J., Carbon nanotubes in nanostructured films: Potential application as amperometric and potentiometric field-effect (bio-)chemical sensors, Phys. Stat. Solidi a 206 (2009) 62-467.

[SmSan86] Smith, L.M.; Sanders, J.Z.; Kaiser, R.J.; Hughes, P.; Dodd, C.; Connell, C.R.; Heiner, C.;. Kent, S.B.H.; Hood, L.E., Fluorescence detection in automated DNA sequence analysis, Nature 321 (1986) 61-67.

[SnSi06] Snustad, D.P.; Simmons, M.J., Principles of Genetics, John Wiley, New York, 2006.

[Sout97] Souteyrand, E.; Cloarec, J.P.; Martin, J.R.; Wilson, C.; Lawrence, I.; Mikkelson, S.; Lawrence, M.F., Direct detection of the hybridization of synthetic homo-oligomer DNA sequences by field effect, J. Phys. Chem. B 101 (1997) 2980-2985.

[SrDi04] Sergeev, N.; Distler, M.; Courtney, S.; Al-Khaldi, S.F.; Volokhov, D.; Chizhikov, V.; Rasooly, A., Multipathogen oligonucleotide microarray for environmental and biodefense applications, Biosens. Bioelectron. 20 (2004) 684-698.

[SteiJa01] Steitz, R.; Jaeger, W.; Klitzing, R.v., Influence of charge density and ionic strength on the multilayer formation of strong polyelectrolytes, Langmuir 17 (2001) 4471-4474.

[Stern07] Stern, E.; Klemic, J.F.; Routenberg, D.A.; Wyrembak, P.N.; Turner-Evans, D.B.; Hamilton, A.D.; LaVan, D.A.; Fahmy, T.M.; Reed, M.A., Label-free immunodetection with CMOS-compatible semiconducting nanowires, Nature 445 (2007) 519-522.

[StrCa00] Strother, T.; Cai, W.; Zhao, X.S.; Hamers, R.J.; Smith, L.M., Synthesis and Characterization of DNA-Modified Silicon (111) Surfaces, J. Am. Chem. Soc.122 (2000) 1205-1209.

[StrHa00] Strother, T.; Hamers, R.J.; Smith, L.M., Covalent attachment of oligodeoxyribonucleotides to amine-modified Si (001) surfaces, Nucleic Acids Res. 28 (2000) 3535-3541.

[Sukh98] Sukhorukov, G.; Donath, E.; Lichtenfeld, H.; Knippel, E.; Knippel, M.; Budde, A.; Möhwald, H., Layer-by-layer self assembly of polyelectrolytes on colloidal particles, Colloids Surf. A 137 (1998) 253-266.

[Sze81] Sze, S.M., Physics of Semiconductor Devices, Wiley, New York, 1981.

[Taba92] Tabata, O.; Asahi, R.; Funabashi, H.; Shimaoka, K.; Sugiyama, S., Anisotropic etching of silicon in TMAH solutions, Sens. Actuators A 34 (1992) 51-57.

[TaGa06] Tansil, N.C.; Gao, Z.Q., Nanoparticles in biomolecular detection, Nano Today 1 (2006) 28-37.

[ThiFr97] Thiel, A.J.; Frutos, A.G.; Jordan, C.E.; Corn, R.M.; Smith, L.M., In situ surface plasmon resonance imaging detection of DNA hybridization to oligonucleotide arrays on gold surfaces, Anal. Chem. 69 (1997) 4948-4956.

[UsIn04] Uslu, F.; Ingebrandt, S.; Mayer, D.; Böcker-Meffert, S.; Odenthal, M.; Offenhäusser, A., Label-free fully electronic nucleic acid detection system based on a field-effect transistor device, Biosens. Bioelectron. 19 (2004) 1723-1731.

[Veer07] Veerabadran, N.G.; Goli, P.L.; Stewart-Clark, S.S.; Lvov, Y.M.; Mills, D.K., Nanoencapsulation of stem cells within polyelectrolyte multilayer shells, Macromol. Biosci. 7 (2007) 877-882.

[VuEsch09] Vu, X.T.; Eschermann, J.F.; Stockmann, R.; GhoshMoulick, R.; Offenhäusser, A.; Ingebrandt, S., Top-down processed silicon nanowire transistor arrays for biosensing, Phys. Stat. Solidi A 206 (2009) 426-434.

[VuGh10] Vu, X.T.; GhoshMoulick, R.; Eschermann, J.F.; Stockmann, R.; Offenhäusser, A.; Ingebrandt, S., Fabrication and application of silicon nanowire transistor arrays for biomolecular detection, Sens. Actuators B 144 (2010) 354-360.

[WaBe09] Becker, W.M.; Kleinsmith, L.J.; Hardin, J.;.Bertoni, G.P., The World of the Cell, Pearson/Benjamin Cummings, San Francisco, 2009.

[WalSh79] Wallace, R.B.; Shaffer, J.; Murphy, R.F.; Bonner, J.; Hirose, T.; Itakura, K., Hybridization of synthetic oligodeoxyribonucleotides to phi chi 174 DNA: The effect of single base pair mismatch, Nucleic Acids Res. 6 (1979) 3543-3558.

[WanKaw01] Wang, J.; Kawde, A.-N., Pencil-based renewable biosensor for label-free electrochemical detection of DNA hybridization, Anal. Chim. Acta 431 (2001) 219-224.

[Wat53] Watson, J.D.; Crick, F.H., Molecular structure of nucleic acids. A structure for deoxyribose nucleic, Nature 171 (1953) 737-738.

[Web1] http://engenheiromecanico.files.wordpress.com/2009/03/nanotube.jpg, 2010.

[Web2] http://www.hightech-edge.com/wp-content/uploads/silicon-nanowires.jpg, 2010.

[Web3] http://de.academic.ru/pictures/dewiki/109/myoglobin.png, 2010.

[Web4] http://www.gamry.com/App_Notes/EIS_Primer/Basics_Of_%20EIS.pdf, 2010.

[Web5] http://www.webelements.com, 2010.

[Web6] http://www.immuneweb.com/DNA_chip-1.pdf, 2010.

[Web7] http://www.sigmaaldrich.com/img/assets/17240/meltingtemp.pdf, 2010.

[WuGu02] Wu, Z.; Guan, L.; Shen, G.; Yu, R., Renewable urea sensor based on a self-assembled polyelectrolyte layer, Analyst 127 (2002) 391-395.

[Xie02] Xie, A.F.; Gramick, S., Local Electrostatics within a polyelectrolyte multilayer with embedded weak polyelectrolyte, Macromolecules 35 (2002) 1805-1813.

[Yate74] Yates, D.E.; Levine, S.; Healy, T.W., Site-binding model of the electrical double layer at the oxide/water interface, J. Chem. Soc. Faraday Trans. 70 (1974) 1807-1818.

[YoSh98] Yoo, D.; Shiratori, S.; Rubner. M., Controlling bilayer composition and surface wettability of sequentially adsorbed multilayers of weak polyelectrolytes, Macromolecules 31 (1998) 4309-4318.

[ZhCh08] Zhang, G.-J.; Chua, J.H.; Chee, R.-E.; Agarwal, A.; Wong, S.M.; Buddharaju, K.D.; Balasubramanian, N., Highly sensitive measurements of PNA-DNA hybridization using oxide-etched silicon nanowire, Biosens. Bioelectron. 23 (2008) 1701-1707.

[ZhLu10] Zhang, G.-J.; Luo, Z.H.; Huang, M.J.; Tay, G.K.; Lim, E.J., Morpholino-functionalized silicon nanowire biosensor for sequence-specific label-free detection of DNA, Biosens. Bioelectron. 25 (2010) 2447-2453.

[Zou08] Zourob, M.; Elwary, S.; Turner, A., Principles of Bacterial Detection: Biosensors, recognition receptors and microsystems, Springer, New York, 2008.

Appendix

A. Recipes and protocols

Cleaning:

For the wet cleaning and activation of sensor surface, the substrate has been dipped in a mixture of 5% Hellmanex and distilled water, followed by rinsing in water and drying with nitrogen.

Dry cleaning and activation of the sensor surface was achieved by treatment of the substrates in oxygen plasma for 45 seconds (0.7 bar, 100 W).

Silanization:

The surface of the sensors has been silanized by immersion of the freshly cleaned substrates in a mixture of 10% MPTES (3-mercaptopropyl trimethoxysilane) and toluol for 1 h followed by washing in toluol, acetonec, isopropanol and water, respectively.

Functionalization of silanized surface with Au-NPs:

For functionalization of the sensor surface with Au-nanoparticles, freshly silanized sensors have been immersed in Au-NP solution (tetraoctylammonium bromide (TOA) stabilized Au-nanoparticles in toluol) for overnight, followed by rinsing in toluol, acetone, isopropanol and ultrapure water, respectively.

Functionalization of the sensor surface with PEM:

Measurement solutions:

- Unbuffered solution: 0.1 M NaCl in distilled water; pH 5.4 (adjusted by NaOH and HCl)
- Buffered solution: 0.1 M NaCl in 1 mM phosphate buffer solution (0.14% monosodium phosphate, monohydrate: 0.001% disodium phosphate, heptahydrate)

- PSS solution: PSS (10 µM, 50 µM) in NaCl solution (1 mM, 10 mM and 100 mM), pH 5.4
- PAH solution: PAH (10 µM, 50 µM) in NaCl solution (1 mM, 10 mM and 100 mM), pH 5.4

The build-up of PEMs on the sensor surface has been achieved by consecutive adsorption of PAH and PSS (with molecular weight of Mw~ 70,000). Sensors were consecutively exposed to the respective PE solution for a time necessary for the adsorption of a single monolayer as well as for obtaining a stable sensor signal (usually 3-5 min), followed by rinsing with a solution of the same salt concentration and pH value as the respective PE solution or with ultrapure water, and exposing to next PE solution without any drying steps. These procedures were repeated until the desired number of layers was achieved. The pH value of all solutions used was adjusted to pH 5.4. As in solutions at pH 5.4 the surface of SiO_2 is negatively charged, we start the PEM formation with positively charged PAH.

DNA immobilization, hybridization and denaturation:

- Measurement solution: 0.2 mM phosphate buffer solution (0.001% monosodium phosphate monohydrate and 0.0034% disodium phosphate heptahydrate) in distilled water (pH 7.1).
- DNA immobilization: Immobilization of thiol-modified 20 base pair perfectly matched ssDNA (5'THI-ATGAACACTGCATGTAGTCA-3') and fully mismatched ssDNA (5'THI-TACTTGTGATGTACATCAGT-3') molecules to the target ssDNA on the surface of Au-NPs was done by pipetting of 40 µl immobilization solution (5 µM ssDNA, 0.1 M phosphate buffer solution (PBS), pH 8.5) onto the particular sensor surface, followed by incubating the sensors in humid conditions at 37 °C overnight. After immobilization, the sensor surface was washed in ultrapure water to remove not-attached ssDNA molecules and dried with nitrogen.
- DNA hybridization: For hybridization, a high ionic-strength solution (0.1 M PBS, 0.9 M NaCl, pH 7) containing 5 µM of target ssDNA (5'-TGACTACATGCAGTGTTCAT-3') was used. The hybridization solution was heated to ~70 °C, and then was pipetted onto the gate surface of the particular sensors. The sensors were left at room temperature for 15-30 min. After the incubation time, the sensor surface was washed (with distilled water for 1 min, 2 × SSC (sodium chloride-sodium citrate buffer) for 1 min, 1 ×

SSC for 1 min, rinsed again with distilled water) to remove the non-hybridized target DNA molecules and finally, dried with nitrogen.

- DNA denaturation: The denaturation process was done by applying a drop of 0.1 M NaOH to the sensor surfaces and leaving it for 1 min. It was followed by washing the sensors with the same protocol as for the hybridization procedure described above.

Penicillin biosensors:

- Polymix buffer solution: This multi-component buffer consists of 2.5 mM TRIS, 2.5 mM KH_2PO_4, 2.5 mM citric acid, 2.5 mM sodium tetraborate, 2.5 mM KCl. The pH of this polymix buffer was adjusted by titration either with NaOH or HCl. The polymix buffer has a constant buffer capacity over a wide pH range including the part from 5 to 9.
- Penicillin solutions: The penicillin solutions were prepared by dissolving penicillin G (benzyl penicillin, 1695 units/mg) in the working buffer. As working buffer, a 0.2 mM polymix multi-component buffer solution containing 100 mM KCl as an ionic strength adjuster was used. The pH of the polymix buffer was adjusted to pH 8 by titration with NaOH solution.
- Enzyme solution: The enzyme solution was prepared by dissolving the enzyme penicillinase (EC 3.5.2.6., Bacillus cereus, specific activity: 1650 units/mg protein) in a 200 mM TEA (trimethanolamine) buffer, pH 8.
- Penicillin biosensor preparation:
    - Adsorptively immobilization of penicillinase: For preparation of the p-Si/SiO_2/penicillinase structure with adsorptively immobilized penicillinase, 80 µl enzyme solution per sensor were pipetted onto the chip surface, incubated at room temperature for about 1 h and dried in N_2 atmosphere.
    - Immobilization of penicillinase using LbL method: For the preparation of the p-Si/SiO_2/$(PAH/penicillinase)_3$-PAH biosensor, the sensor chip was exposed to the PAH (50 µM PAH, 0.1 M NaCl, pH 6) solution for 5 min, followed by rinsing with ultrapure water and dried with N_2. Then, the enzyme penicillinase has been immobilized onto the modified sensor surface using the same immobilization protocol as for the p-Si/SiO_2/penicillinase sensor described above. These procedures were repeated until the desired number of PAH/penicillinase bilayers (in this study, three bilayers) were prepared.

Before their first use, the prepared penicillin biosensors were incubated in working buffer for at least 1 h to let the enzyme membrane equilibrate. When not in use, the sensors were stored in Titrisol buffer, pH 7, at 4 °C.

B. Photomask for sensor-array fabrication

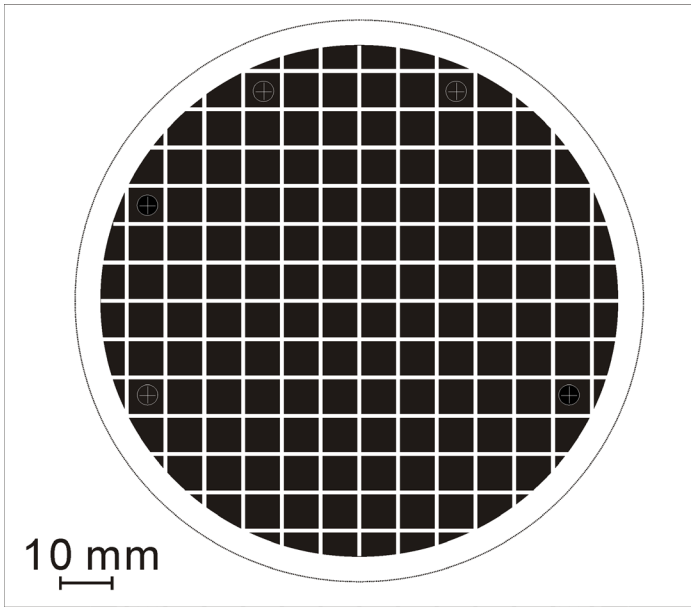

Photomask used for etching a trench in the top-Si layer.

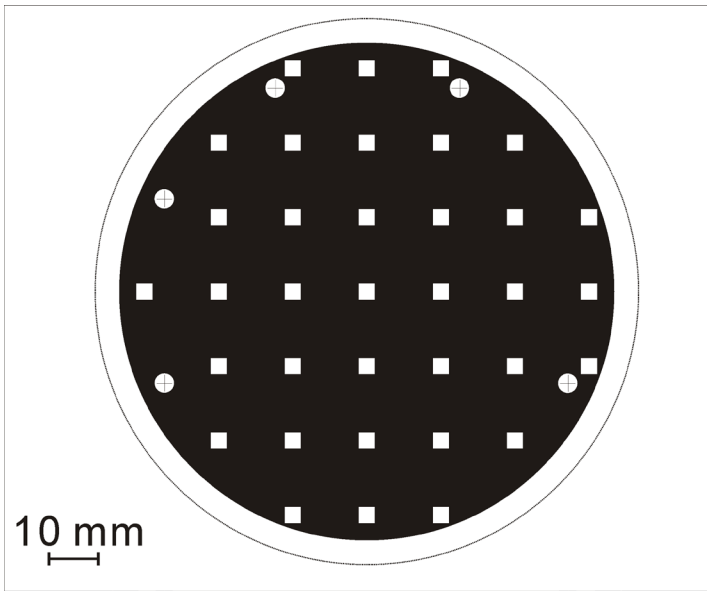

Photomask used for etching of the top-SiO_2 layer and deposition of the Al top contact.

C. Design of the EISOI measurement cell

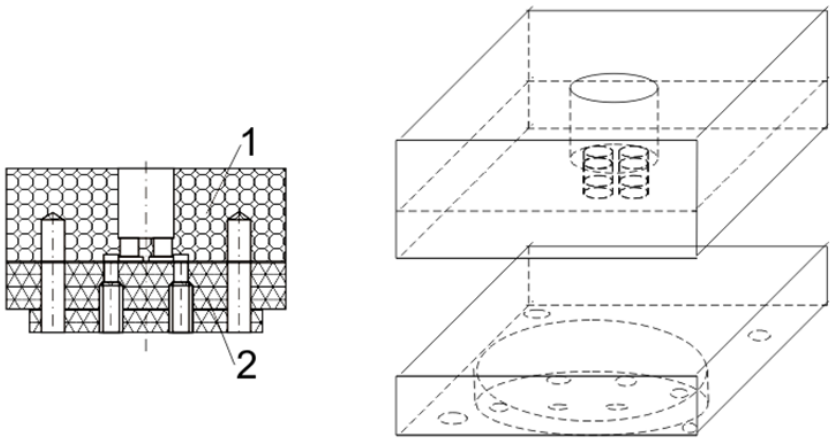

Technical cross-sectional sketch of the developed measurement cell for the EISOI sensor array.

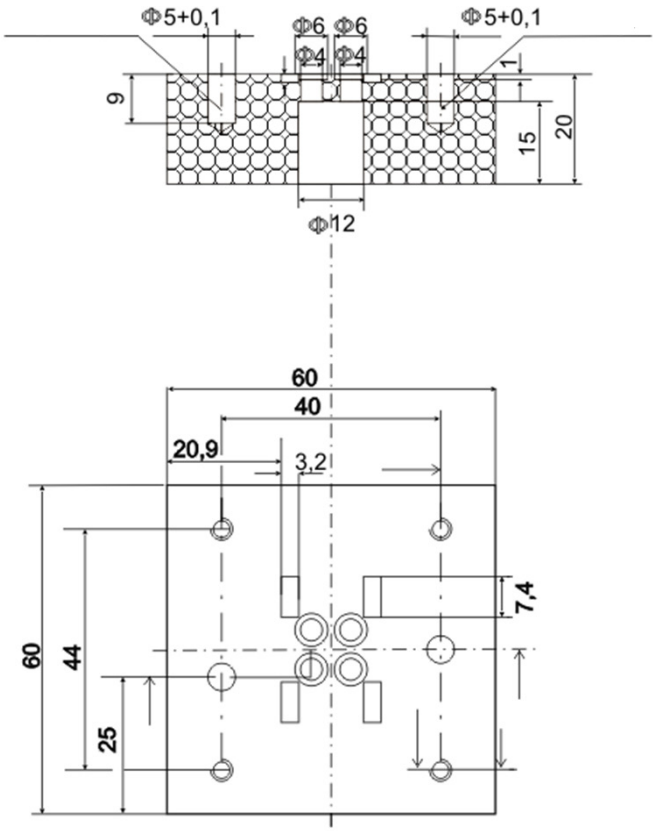

Top view sketch of upper part of the measuring cell.

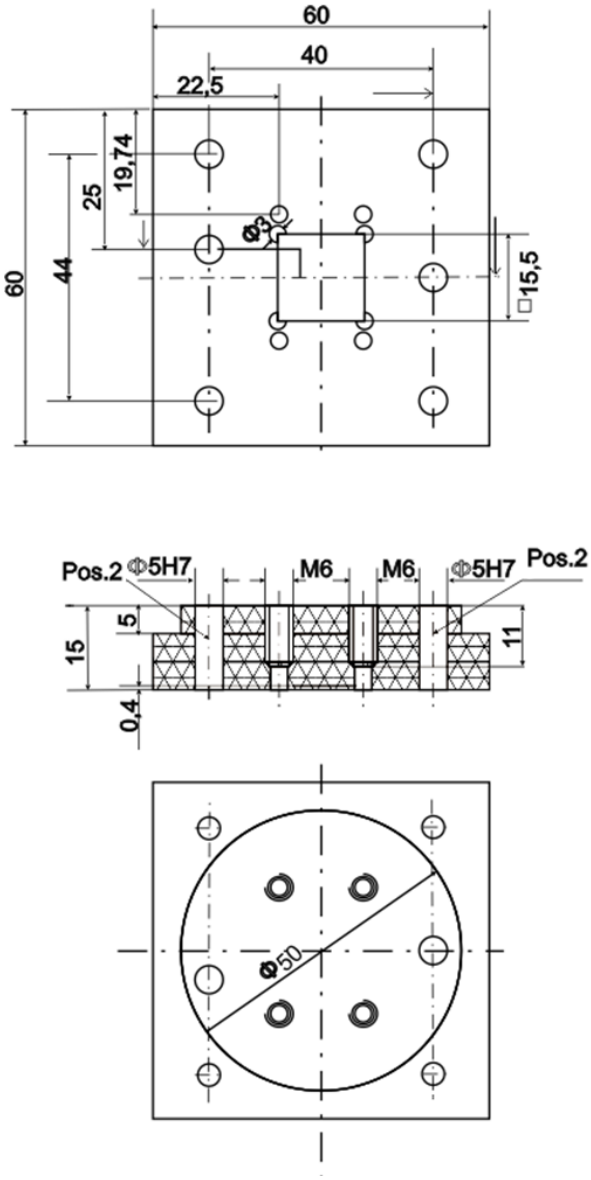

Top and bottom view of the lower part of the measuring cell.

Acknowledgements

I am grateful to numerous local and global “peers” who have contributed towards shaping this study. This is now a unique opportunity to acknowledge them, even though in a very small way.

First, I would like to express my appreciation to Prof. Dr. Michael J. Schöning for his advice during my Ph.D. work. I thank him for providing me with the opportunity to work with a talented team of researchers and attending in national and international conferences. His mentorship, in particular, has helped me overcome many technical and non-technical challenges, which I am grateful for.

I would like to express my deep gratitude to Prof. Dr. Arshak Poghossian who helped me during my research work courageously. His experience and guidance has greatly influenced the makeup of the research outcomes presented in this thesis. His broad vision and intellect has always been a source of inspiration for me. I would like to express my sincere thanks for generously sharing his time and knowledge.

My special thanks to Priv.-Doz. Dr. Werner Moritz for providing the opportunity to do this work in cooperation with his research group. I would like to thank him for his continuous interest, support, critical comments and suggestions during the period of my thesis work.

I am thankful to Prof. Dr. Erhard Kemnitz, Prof. Dr. Wolfgang Rettig, Prof. Dr. Ulrich Panne and Prof. Dr. Rainer Mahrwald for the attendance in examination committee.

I sincerely thank Prof. Dr. Sven Ingebrandt, Prof. Dr. Andreas Offenhäusser, Dr. Dirk Mayer as well as their research group at the Research Center Jülich GmbH, and specially Xu-Thang Vu for his advice and critical comments regarding to the fabrication of the nanoplate sensor array.

I am also grateful to Prof. Dr. Michael Keusgen from Philipps University of Marburg, Dr. Jenny Gun and Prof. Dr. Ovadia Lev from Hebrew University of Jerusalem (Israel), Prof. Dr. Patrick Wagner and Prof. Dr. Hans-Gerd Boyen from Hasselt University (Belgium), Prof. Dr. Vahe Buniatyan from State Engineering University of Armenia, Prof. Dr. Christiane Vaeßen and Prof. Dr. Thorsten Selmer from Aachen University of Applied Sciences for sharing their knowledge and experiences and great discussions. They have been always an exceptional source of support for me.

I would like to appreciate Dr. Andrey Cherstvy from Institute of Solid State Physic (IFF), in Research Center Jülich GmbH. It has been a pleasure to work with such an excellent physicist, and to learn from his vast knowledge of theoretical soft-matter and biophysics.

Special thanks are also due to Prof. Dr. Gereon Elbers and Prof. Dr. Günter Jeromin for giving me the opportunity to attend in their lectures in inorganic and organic chemistry. I am very thankful for their advices and sharing their knowledge.

I am thankful to members of IBN-PT and clean room stuff at Research Center Jülich GmbH, with whom I had the pleasure to work: Alfred Steffen, Jürgen Müller, Jana Mohr and Stephany Bunte.

Special thanks to Hans-Peter Bochem for SEM pictures, sharing his experiences about characterization of different structures and very useful discussions.

I had the pleasure to work together with seven master students, during my Ph.D. time. I would like to thank Shrutti Mankar, Yi Zhang, Dhruv Gandhi, Arash Razavi, Angela Pedraza, Kerstin Malzahn and Piyush Mehndiratta. Most of the results presented here would not have been possible without their engagement.

I am very grateful for all the support that I have received from the members of the Institute of Nano- and Biotechnologies as well as many others of my colleagues at Aachen University of Applied Sciences. Special thanks to Dr. Bernd Kraus, Dr. Monika Turek, Eylem Kurulgan-Demirchi, Dr. Taylan Demirchi, Matthias Bäcker, Christina Huck, Johannes Schiffels, David Rolka and Stefan Beging.

Thank you to Behnaz Golab, Maryam Lashkary, Sheida Mirfaizi and Saeed Arshadi for encouragement and moral support.

Of course, my greatest gratitude, affection and love belong to my family. I would like to thank my Mom, Dad and boyfriend for love, patience, and understanding. I dedicate this thesis to them.

Publikationen

[1] **Abouzar, M.H.**; Poghossian, A.; Pedraza, A.; Ingebrandt, S.; Moritz, W.; Schöning, M.J., (Bio-)chemical sensor array based on nanoplate SOI capacitors, Biosens. Bioelectron. 26 (2011) 3023-3028.

[2] **Abouzar, M.H.**; Moritz, W.; Schöning, M.J.; Poghossian, A., Capacitance-voltage and impedance-spectroscopy characteristics of nanoplate EISOI capacitors, Phys. Stat. Solidi A 208 (2011) 1327-1332.

[3] Poghossian, A.; Malzahn, K.; **Abouzar, M.H.**; Mehndiratta, P.; Katz, E.; Schöning, M.J., Integration of biomolecular logic gates with field-effect transducers, Electrochim. Acta, doi:10.1016/j.electacta.2011.01.102.

[4] Gun, J.; Gutkin, V.; Boyen, H.-G.; Saitner, M.; Wagner, P.; D'Olieslaeger, M.; **Abouzar, M.H.**; Poghossian, A.; Schöning, M.J., Tracing gold nanoparticle charge by electrolyte-insulator-semiconductor devices, J. Phys. Chem. C 115 (2011) 4439-4445.

[5] **Abouzar, M.H**.; Pedraza, A.M.; Schöning, M.J.; Poghossian, A., Label-free DNA hybridization and denaturation detection by means of field-effect nanoplate SOI capacitors functionalized with gold nanoparticles, Procedia Engineering 5 (2010) 918-921.

[6] **Abouzar, M.H.**; Poghossian, A.; Siqueira, Jr.J.R.; Oliveira, Jr.N.O.; Moritz, W.; Schöning, M.J., Capacitive electrolyte-insulator-semiconductor structures functionalized with a polyelectrolyte/enzyme multilayer: New strategy for enhanced field-effect biosensing, Phys. Stat. Solidi A 207(4) (2010) 884-890.

[7] Buniatyan, V.V.; **Abouzar, M.H.**; Matirosyan, N.W.; Schubert, J.; Gevorgian, S.; Schöning, M.J.; Poghossian, A., pH-sensitive properties of barium strontium titanate (BST) thin films prepared by pulsed laser deposition technique, Phys. Stat. Solidi A 207(4) (2010) 824-830.

[8] Bäcker, M.; Poghossian, A.; **Abouzar, M.H.**; Wenmackers, S.; Janssens, K.; Haenen, K.; Wagner, P.; Schöning, M.J., Capacitive field-effect (bio-)chemical sensors based on nanocrystalline diamond films, Mater. Res. Soc. Sympos. Proc., 1203 (2010) paper 1203-J17-31, 1-6.

[9] **Abouzar, M.H.**; Ingebrandt, S.; Poghossian, A.; Zhang, Y.; Vu. X.T.; Moritz, W.; Schöning, M.J., Nanoplate field-effect capacitive (bio-)chemical sensor array based on SOI structure, Procedia Chemistry 1 (2009) 670-673.

[10] **Abouzar, M.H.**; Ingebrandt, S.; Poghossian, A.; Zhang, Y.; Moritz, W.; Schöning, M.J., Field-effect nanoplate capacitive pH sensor based on SOI structure, Proc. of 7th Int. Conf. on Semiconductor Micro- and Nanoelectronics (2009) 53-56.

[11] Buniatyan, V.V.; Matirosyan, N.W.; **Abouzar, M.H.**; Schöning, M.J.; Poghossian, A.; Schubert, J.; Khachatryan, V.R.; Soukiassyan, G.R., (Ba,Sr)TiO_3 based electrolyte-insulator-semiconductor pH sensors: comparative study, Proc. of 7th Int. Conf. on Semiconductor Micro- and Nanoelectronics (2009) 57-60.

[12] Poghossian, A.; Krämer, M.; **Abouzar, M.H.**; Pita, M.; Katz, E.; Schöning, M.J., Interfacing of biocomputing systems with silicon chips: Enzyme logic gates based on field-effect devices, Procedia Chemistry 1 (2009) 682-685.

[13] Gun, J.; Rizkov, D.; Lev, O.; **Abouzar, M.H.**; Poghossian, A.; Schöning, M.J., Oxygen plasma-treated gold nanoparticle-based field-effect devices as transducer structures for bio-chemical sensing, Microchim. Acta 164 (2009) 395-404.

[14] Siqueira, Jr.J.R.; **Abouzar, M.H.**; Poghossian, A.; Zucolotto, V.; Oliveira Jr.O.N.; Schöning, M.J., Penicillin biosensor based on a capacitive field-effect structure functionalized with a dendrimer/carbon nanotube multilayer, Biosens. Bioelectron. 25 (2009) 497-501.

[15] Poghossian, A.; **Abouzar, M.H.**; Razavi, A.; Bäcker, M.; Bijnens, N.; Williams, O.A.; Haenen, K.; Moritz, W.; Wagner, P.; Schöning, M.J., Nanocrystalline-diamond thin films with high pH and penicillin sensitivity prepared on a capacitive Si-SiO_2 structure, Electrochim. Acta 54 (2009) 5981-5985.

[16] Siqueira, Jr.J.R.; **Abouzar, M.H.**; Bäcker, M.; Zucolotto, V.; Poghossian, A.; Oliveira, Jr.O.N.; Schöning, M.J., Carbon nanotubes in nanostructured films: Potential application as amperometric and potentiometric field-effect (bio-)chemical sensors, Phys. Stat. Solidi 206 (2009) 462-467.

[17] **Abouzar, M.H.**; Poghossian, A.; Razavi, A.; Williams, O.A.; Bijnens, N.; Wagner, P.; Schöning, M.J., Characterisation of capacitive field-effect sensors with a nanocrystalline-diamond film as transducer material for multi-parameter sensing, Biosens. Bioelectron. 24 (2009) 1298-1304.

[18] Schöning, M.J.; **Abouzar, M.H.**; Poghossian, A., pH and ion sensitivity of a field-effect EIS (electrolyte-insulator-semiconductor) sensor covered with polyelectrolyte layers, J. Solid State Electrochem. 13 (2009) 115-122.

[19] Poghossian, A.; **Abouzar, M.H.**; Christiaens, P.; Williams, O.A.; Haenen, K.; Wagner, P.; Schöning, M.J., Sensing charged macromolecules with nanocrystalline diamond-based field-effect capacitive sensors, Journal of Contemporary Physics 43(2) (2008) 77-81 (English) 120-127 (Russian).

[20] **Abouzar, M.H.**; Poghossian, A.; Christiaens, P.; Williams, O.A.; Haenen, K.; Wagner, P.; Schöning, M.J., Feldeffektsensor auf nanokristalliner Diamantbasis, VDI-Berichte 2011 (2008) 549-558.

[21] **Abouzar, M.H.**; Poghossian, A.; Razavi, A.; Besmehn, A.; Bijnens, N.; Williams, O.A.; Haenen, K.; Wagner, P.; Schöning, M.J., Penicillin detection with nanocrystalline-diamond field-effect sensor, Phys. Stat. Solidi A 205 (2008) 2141-2145.

[22] Poghossian, A.; **Abouzar, M.H.**; Schöning, M.J., Capacitance-voltage and impedance characteristics of field-effect EIS sensors functionalized with polyelectrolyte multilayers, ITBM-RBM 29 (2008) 149-154.

[23] Schöning, M.J.; **Abouzar, M.H.**; Poghossian, A.; Han, Y.; Offenhäusser, A.; Ingebrandt, S., Markierungsfreie DNA-Detektion mit Silizium-Feldeffekt-Sensoren – Messeffekte oder Artefakte?, Technisches Messen 9 (2007) 466-474.

[24] Christiaens, P.; **Abouzar, M.H.**; Poghossian, A.; Wagner, T.; Bijnens, N.; Williams, O.A.; Daenen, M.; Haenen, K.; Douheret, O.; D'Haen, J.; Mekhalif, Z.; Schöning, M.J.; Wagner, P., pH sensitivity of nanocrystalline diamond films, Phys. Stat. Solidi A 204 (2007) 2925-2930.

[25] Schöning, M.J.; **Abouzar, M.H.**; Wagner, T.; Näther, N.; Rolka, D.; Yoshinobu, T.; Kloock, J.P.; Turek, M.; Ingebrandt, S.; Poghossian, A., A semiconductor-based field-effect platform for (bio-)chemical and physical sensors: From capacitive EIS sensors and LAPS over ISFETs to nano-scale devices, Material Res. Soc. Sympos. Proc. 952 (2007) paper 0952-F08-02, 1-9.

[26] Poghossian, A.; Ingebrandt, S.; **Abouzar, M.H.**; Schöning, M.J., Label-free detection of charged macromolecules by using a field-effect-based sensor platform: Experiments and possible mechanisms of signal generation, App. Phys. A 87 (2007) 517-524.

[27] Poghossian, A.; **Abouzar, M.H.**; Amberger, F.; Mayer, D.; Han, Y.; Ingebrandt, S.; Offenhäusser A.; Schöning, M.J., Field-effect sensors with charged macromolecules: Characterisation by capacitance-voltage, constant-capacitance, impedance spectroscopy and atomic-force microscopy methods, Biosens. Bioelectron. 22 (2007) 2100-2107.

[28] Poghossian, A.; **Abouzar, M.H.**; Sakkari, M.; Kassab, T.; Han, Y.; Ingebrandt, S.; Offenhäusser, S.; Schöning, M.J., Field-effect sensors for monitoring the layer-by-layer adsorption of charged macromolecules, Sens. Actuators B 118 (2006) 163-170.

[29] Schöning, M.J.; **Abouzar, M.H.**; Ingebrandt, S.; Platen, J.; Offenhäusser, A.; Poghossian, A., Towards label-free detection of charged macromolecules using field-effect-based structures: Scaling down from capacitive EIS sensor over ISFET to nanoscale devices, Material Res. Soc. Sympos. Proc. 915 (2006) paper 0915-R05-04, 1-6.

Eidesstattliche Erklärung

Hiermit versichere ich, dass ich die Dissertation selbstständig verfasst und keine anderen als die angegebenen Quellen und Hilfsmittel benutzt habe.

Maryam Hadji Abouzar

Linnich den 31.03.2011